

Phonon-phonon interactions in highly anharmonic systems

Thesis by
Vladimir Vladimirovich Ladygin

In Partial Fulfillment of the Requirements for the
Degree of
Doctor of Philosophy

The logo for the California Institute of Technology (Caltech), featuring the word "Caltech" in a bold, orange, sans-serif font.

CALIFORNIA INSTITUTE OF TECHNOLOGY
Pasadena, California

2025
Defended May 19, 2025

© 2025

Vladimir Vladimirovich Ladygin
ORCID: 0000-0002-5697-6956

All rights reserved

To my father.

ACKNOWLEDGEMENTS

I started Ph.D. during the pandemic, but it did not stop me from meeting wonderful people inside and outside Caltech. Here, I want to express my gratitude to all of you.

This work would not have been possible without my advisor, Brent Fultz. I thank him for inviting the simulation person to the group and showing the experimental side of phonon physics by introducing me to neutron scattering experiments. I appreciate his patience with my computational enthusiasm, and his guidance and support for my study. He also helped me arrange my arrival to Caltech during the COVID-19 pandemic. I am grateful to my thesis committee members: Joseph Falson, Keith Schwab, William Goddard, and Marco Bernardi.

I would like to acknowledge my colleagues from outside Caltech: Florian Knoop, Samuel Poncé, Maya Greenberg, Omer Yaffe, and Olle Hellman. Special thanks go to Camille Bernal-Choban and Claire Saunders for their contribution to the work, Anne Lin for the supportive office environment, and Elena Priesen Reis for her words of care. I also thank the current and past members of the group for conversations about life and science, including Pedro Gusman, Ziyi Wang, Stefan Lohaus, Ethan Klein, Kyle Hunady, and Ihab Elmasri.

I wish to acknowledge the staff of ORNL, especially Garrett Granroth, who helped me run experiments and data postprocessing and always answered questions throughout my Ph.D. I also thank Mike Manley for thoughtful discussions and helpful career advice. I also thank my mentors back in Russia, Alexey Yanilkin and Alexander Shapeev, who introduced me to the field of computational materials science and scientific software design.

I'm grateful to my friends and colleagues from the Moscow Institute of Science and Technology for visiting me, some of them from far away during my time here, especially Adel, Alina, and Sonia. I also thank my university and school friends, Ilya Beniya and Maxim Mihailov.

Finally, I wish to acknowledge the members of my family who took care of me on this path. Nothing would have been possible without my wife, who joined me on this journey to a new country and in life. My mom was always there for me, engaged in endless science and life phone calls. I want to thank my father separately, who believed in me at every point of my life.

Funding for the work was provided by the Department of Energy (DOE) Office of Energy Science program Basic Energy Sciences (BES) under Contract DE-FG02-03ER46055. The National Energy Scientific Computing Center (NERSC) provided the computing resources for the studies. The neutron scattering data was collected at Spallation Neutron Source (SNS), a DOE facility operated by Oak Ridge National Laboratory (ORNL).

ABSTRACT

The phonon, a quantum of atomic vibrations, is a core ingredient in the description of materials' behavior at both high and low temperatures. A harmonic theory of lattice dynamics treats phonons as independent, noninteracting normal modes with long lifetimes. The proper description of phenomena in solids requires the phonons to interact depending on temperature, or in other words, to act anharmonically. The phonon interaction in highly anharmonic crystals can result in intermodulation and an additional coherent scattering intensity at frequencies of the sums and differences of classical normal modes. At low temperatures, anharmonic interaction is triggered by nuclear quantum effects of zero-point motion, which can be observed as intermodulation and negative thermal expansion (NTE). In the thesis, I expand the general understanding of intermodulation phenomena using computational and experimental methods by adding missing parts expected in the theoretical intermodulation picture, such as phonon second harmonic generation and nuclear quantum intermodulation.

The latent heat, L , is central to melting, but its atomic origin remains elusive. It is proportional to the entropy of fusion, $\Delta S_{\text{fus}} = L/T_m$ (T_m is the melting temperature), which depends on changes of atom configurations, atom vibrations, and thermal electron excitations. Here, I use machine-learned molecular dynamics to complement experimental results in the aim of separating ΔS_{fus} into these components for Ge, Si, Bi, Sn, Pb, and Li. When the vibrational entropy of melting, ΔS_{vib} is zero, $\Delta S_{\text{fus}} \simeq 1.2 k_B$ per atom. This result provides a baseline for ΔS_{config} and nearly coincides with ‘‘Richard’s Rule’’ of melting. The ΔS_{fus} deviates from this value for most elements, however, we show that this deviation originates with extra ΔS_{vib} and extra ΔS_{config} . These two components are correlated for positive and negative deviations from Richard’s rule — the extra ΔS_{config} is consistently $\sim 80\%$ of ΔS_{vib} .

The phenomenon of second harmonic generation (SHG) was found for phonons in anharmonic NaBr by inelastic neutron scattering. The temperature dependence of this phonon SHG was measured from 300 K to 650 K. At 300 K the second harmonic (SH) is seen as a high-energy branch around 33 meV, nearly independent of \vec{Q} . The temperature effective potential (TDEP) method and classical molecular dynamics (MD) simulation with machine learning interatomic potential were able to reproduce the SH, and showed that SHG occurs with the flat transverse optical (TO) phonon branch. A classical model of a nonlinear medium explains the intensity

and lifetime of the SH, compared to those of the TO modes. Also successful was a quantum model based on the Heisenberg-Langevin equation for interacting phonons coupled to a thermal bath, which also predicts a spectral distribution of the SH. The measured temperature dependence of the intensity of the second harmonic showed that it follows the Planck distribution of a one-phonon quasiparticle, and not two TO phonons.

The anharmonic behavior of phonons and thermal expansion of hexagonal zinc were studied from 15 to 690 K by inelastic neutron scattering (INS) and ab initio simulations. Phonon spectra were measured for Q -points over the full Brillouin zone, giving the phonon density of states (DOS), and dispersions along high-symmetry directions. The dispersions were crisp at 15 K, but diffuse intensity was observed at energies above them. The dispersions broadened with temperature, T , and the diffuse intensity grew relatively stronger. This diffuse intensity appeared in all INS measurements and simulations, except for classical molecular dynamics at 15 K. The TDEP method was used to calculate the free energy and thermal expansion with the nuclear quantum effect from zero-point vibrational dynamics. For $T < 100$ K the nuclear quantum effect was essential for obtaining the negative thermal expansion, and path integral molecular dynamics (PIMD) was particularly effective for obtaining the negative thermal expansion in the basal plane. A Heisenberg-Langevin model for interacting phonons coupled to a thermal bath was able to reproduce the shape and intensity of the diffuse spectral features.

Atomic vibrational dynamics in cuprite, Cu_2O , was studied by inelastic neutron scattering and molecular dynamics (MD) simulations from 10 K to 900 K. At 300 K, a diffuse inelastic intensity (DII) appeared in the phonon dispersions, and dominated the spectral intensity at higher temperatures. Classical MD simulations with a machine learning interatomic potential reproduced general features of the DII. Better agreement with experiment was obtained with the addition of a stiffer potential at close approaches of the Cu and O-atoms. The DII originates from random phase shifts of vibrating O-atoms that have brief (~ 10 fs) anharmonic interactions with neighboring Cu-atoms. The spectrum of DII gives information about the interaction time of anharmonic interactions between atoms, and its intensity gives a strength of coupling between vibrating atoms and a thermal bath.

PUBLISHED CONTENT AND CONTRIBUTIONS

- [1] V. V. Ladygin, F. Knoop, C. M. Bernal-Choban, C. Saunders, G. Granroth, and B. Fultz. Anharmonic phonons and nuclear quantum effects in Zn. *Manuscript submitted for publication*, 2025.
V.V.L. participated in the experiment, analyzed the experimental data, performed simulations and theory derivations, and wrote the manuscript.
- [2] C. N. Saunders, V. V. Ladygin, D. Kim, C. M. Bernal-Choban, S. Lohaus, G. Granroth, D. L. Abernathy, and B. Fultz. Diffuse intensity from phonon noise in inelastic neutron scattering. *Phys. Rev. Mater.*, 9:024602, Feb 2025. doi: 10.1103/PhysRevMaterials.9.024602. URL <https://link.aps.org/doi/10.1103/PhysRevMaterials.9.024602>.
V.V.L. as a coauthor performed simulations, and participated in writing the manuscript.
- [3] V. V. Ladygin, C. N. Saunders, C. M. Bernal-Choban, D. L. Abernathy, M. E. Manley, and B. Fultz. Phonon second harmonic generation in nabr studied by inelastic neutron scattering and computer simulation. *Phys. Rev. Mat.*, 9: 015002, Jan 2025. doi: 10.1103/PhysRevMaterials.9.015002. URL <https://link.aps.org/doi/10.1103/PhysRevMaterials.9.015002>.
V.V.L. participated in the experiment data collection, analyzed the experimental data, performed simulations and theory derivations, and wrote the manuscript.
- [4] C. M. Bernal-Choban, V. V. Ladygin, Garrett Granroth, C. N. Saunders, S. Lohaus, D. L. Abernathy, and B. Fultz. Atomistic origin of the entropy of melting from inelastic neutron scattering and machine learned molecular dynamics. *Comm. Mat.*, 2024. doi: <https://doi.org/10.1038/s43246-024-00695-x>. URL <https://www.nature.com/articles/s43246-024-00695-x>.
V.V.L. as a coauthor performed simulations, and participated in writing the manuscript.
- [5] V. V. Ladygin, I. Beniya, E. Makarov, and A. Shapeev. Bayesian learning of thermodynamic integration and numerical convergence for accurate phase diagrams. *Phys. Rev. B*, 104(10):104102, 2021. doi: <https://doi.org/10.1103/PhysRevB.104.104102>.
V.V.L. performed simulations, methodology design, software design, model fitting, and wrote the manuscript.
- [6] V. V. Ladygin, Y. Korotaev, A. Yanilkin, and A. Shapeev. Lattice dynamics simulation using machine learning interatomic potentials. *Comput. Mater. Sci.*, 172:109333, 2020. doi: <https://doi.org/10.1016/j.commatsci.2019.109333>.
V.V.L. performed simulations, methodology design, model fitting, and wrote the manuscript.

TABLE OF CONTENTS

Acknowledgements	iv
Abstract	vi
Published Content and Contributions	viii
Table of Contents	viii
List of Illustrations	xi
List of Tables	xviii
Nomenclature	xix
Chapter I: Introduction	1
Chapter II: Background	4
2.1 Introduction	4
2.2 Neutron Scattering	4
2.3 Vibrations in solid	7
2.4 Moment Tensor Potential (MTP)	11
Bibliography	14
Chapter III: Bayesian learning of thermodynamic integration applied to atom- istic origin of the entropy of melting	17
3.1 Thermodynamic Integration with MTP	18
3.2 Inelastic Neutron Scattering	28
3.3 Results and Discussion	30
3.4 Conclusion	33
3.5 Supplemental Materials	34
Bibliography	39
Chapter IV: Diffuse Intensity from Phonon Noise in Inelastic Neutron Scat- tering in cuprite	45
4.1 Introduction	45
4.2 Experimental Measurements and Ab Initio Simulation	47
4.3 Results and Discussion	50
4.4 Theory	51
4.5 Summary and Conclusion	60
4.6 Supplemental Materials	61
Bibliography	69
Chapter V: Phonon second harmonic generation in Sodium Bromide	74
5.1 Introduction	74
5.2 Experiment	75
5.3 Computation	75
5.4 Theory	79
5.5 Discussion	85
5.6 Conclusion	85
5.7 Supplemental Material	86

Bibliography	93
Chapter VI: Anharmonic phonons and nuclear quantum effects in Zinc	96
6.1 Introduction	96
6.2 Experimental Details	97
6.3 Ab Initio Simulations	98
6.4 Heisenberg-Langevin Equation	104
6.5 Thermal Expansion	106
6.6 Conclusion	109
6.7 Supplemental Material	109
Bibliography	120
Chapter VII: Final Remarks and Future Directions	125
7.1 New Methods Development	125
7.2 Sidebands and Nonlinear Optics	126
7.3 Diffuse Inelastic Intensity	129
Bibliography	131

LIST OF ILLUSTRATIONS

<i>Number</i>	<i>Page</i>
2.1 Illustration of the neutron scattering event. On the left, the incident neutron with momentum \vec{k}_i and energy \vec{E}_i scatters off the sample changing momentum to \vec{k}_f and energy \vec{E}_f . This results in the formation of the phonon with energy ΔE and momentum \vec{Q} . On the right, the triangular diagram of the momentum conservation law.	5
2.2 Scheme of the ARCS instrument with labeled components.	6
3.1 Entropies of fusion, ΔS_{fus} , and their number distribution. (a) Entropies of fusion for elements up to uranium, plotted versus atomic number. The elements chosen for this study are indicated by a vertical line and are annotated with the value of their entropy of fusion. Circles (crosses) designate experimentally (computationally) studied elements. (b) Distribution of ΔS_{fus} for the first 92 elements. The dashed lines in (a) and (b) show Richard's rule of $1.1 k_{\text{B}}$ per atom.	19
3.2 Illustration of integration via the trapezoidal quadrature rule (red) and Gaussian process (blue) on noisy data. The left graph shows how the function $f(x) = \sin(x)$ is reconstructed and the right one shows how the derivative is reconstructed. The Gaussian process has the same accuracy, but produces a smooth result and also yields uncertainties of prediction within which the exact solution (purple) falls.	26
3.3 General scheme of the Bayesian framework for calculating free energy as a function of volume and temperature.	27
3.4 Thermodynamic data for free energy integration from Molecular Dynamics simulation of Li, Pb, Si, and Ge in the crystalline solid (gray triangles), liquid (black circles), and melting point (grey diamonds).	28
3.5 Vibrational DOS curves from velocity autocorrelations of Li, Pb, Si, and Ge in the crystalline solid (gray triangles) and liquid (black circles) from computations. Note the large softening in liquid Ge and the small stiffening in Li and Pb. All DOSs are normalized to one.	29

- 3.6 Inelastic neutron scattering spectra for solid and liquid Ge and Pb. Total $S(Q, \varepsilon)$ in the crystalline solid (top left) and liquid (bottom left) phases after background subtraction, with selected $S(Q_n, \varepsilon)$ (right) normalized to $S(Q)$ for (a) Ge and (b) Pb near their respective melting temperatures. The $S(Q, \varepsilon)$ intensity bars for the solid and liquid phases of each element are the same and are on a log scale. The dashed lines under the constant Q cuts are quasielastic fits to the data that include a convolution with the Q and ε -dependent instrument resolution function. Standard errors (grey bars) are generally smaller than the symbol size. 31
- 3.7 Experimental DOS curves. Each DOS curve is from Q -cuts of Pb, Sn, Bi, and Ge in the crystalline solid (gray triangles) and liquid (black circles) phases. Note the large softening in liquid Ge and the small stiffening in Pb. All DOSs are normalized to one. 31
- 3.8 Atomistic components of the entropy of fusion from inelastic neutron scattering and molecular dynamics. (a) Vibrational (light gray), and extra (dark gray) contributions to the entropies of fusion in Ge, Bi, Sn, and Pb determined from Q -weighted densities of states. Error bars were estimated from the two scalings of the neutron-weighted density of states (see details in Methods: Density of States Analysis). (b) Vibrational (light gray), configurational (dark gray), and electronic (black) contributions to the entropies of fusion in Ge, Si, Pb, and Li from computations. The horizontal dashed line is the total entropy of fusion, $\Delta S_{\text{fus}} = 1.1 k_B$ per atom, according to Richard's rule. . . . 32
- 3.9 Vibrational entropies across the melt versus the total entropy of fusion. Circles (crosses) are from experimental (computational) results. The intercept at $\Delta S_{\text{fus,vib}} = 0$ occurs at $\Delta S_{\text{fus}} \approx 1.2 k_B$ per atom, near the value of Richard's rule. 34
- 4.1 Examples of nonlinearities in phase space of an oscillator. (a) Trajectory in p - q (momentum-position) phase space of harmonic oscillator and hard-wall oscillator (rectangle with instant reversal at walls). Both have the same velocity at $q = 0$ and have the same period. (b) Example of phase space for an oscillation with a potential that is harmonic at small q but with moveable hard walls at larger q 46

4.2	Experimental and computational vibrational spectra projected onto high-symmetry directions. Columns from left to right: INS data, MD MLIP with Cu-O bound splined to ZBL potential at low separations; and MD MLIP without ZBL potential. Rows from top to bottom: 900 K, 700 K, 300 K, 10 K. Each panel is normalized with respect to its total inelastic intensity (data are on log scale at right).	49
4.3	Atom arrangement and phonon density of states in cuprite. (a) Tetrahedral arrangement of Cu-atoms about O-atom in cuprite. (b) Phonon partial DOS from sTDEP calculations using second-order terms at 300 K. Solid curves are Cu-atoms, dashed are O-atoms.	54
4.4	Characteristic timescale of DII in cuprite from Fourier transform of vibrational spectra. (a) Average inelastic intensity from left column of Fig. 2, and (b) its Fourier transform. (c) Fourier transform from 0 to 100 fs. ($F[I(\omega)] \equiv P(t)$) Temperatures from top to bottom are 900 K, 700 K, 300 K, and 10 K.	54
4.5	Illustration of semi-periodic model application to cuprite. (a) Time-time correlation function of Eq. (4.22) for $\gamma = \tau/3$. (b) Intensity $I(\omega)$ of Eq. 4.26 from Fourier transform of panel a, for different ratios of γ/τ (c) Comparison of predicted spectral weight from Cu-atoms with the experimental data from cuprite at 700 K.	59
4.6	Illustration of subtraction of multiphonon correction of cuprite at 900 K. (a) $S_{exp}(Q , E)$, reduced data after background subtraction and rebinning into $ \vec{Q} $. (b) calculated multiphonon correction $S_{MP}(Q , E)$ for $2 \leq n \leq 8$. (c) data of panel a after subtraction of multiphonon scattering. to the total scattering function $S_{exp}(Q , E)$	63
4.7	Comparison between vibrational spectra computed with sTDEP and autocorrelation function analyses. (left column) Calculated sTDEP phonon dispersions along high-symmetry directions. (right column) MD simulations with noise from Langevin thermostat. Temperatures from top to bottom: 900 K, 700 K, 300 K, and 10 K.	64
4.8	Average phonon density of states from Fig. 1 in the main text (left) and its Fourier transform (right). (a), (b), (c) for experimental data, and (d), (e), (f) for molecular dynamics simulations with a MTP-ZBL potential. Temperatures from top to bottom are: 900 K, 700 K, 300 K, and 10 K.	66

4.9	Anharmonicity quantification in cuprite. Left panel: anharmonicity measure for temperatures in Figure 2 of the main text. The blue color corresponds to Molecular Dynamics simulations with MTP describing interatomic interaction; results with MTP potential splined to ZBL are red; the anharmonicity measure after including third-order forceconstant contribution is shown with dashed lines. Right panel: potential energy along Cu-O bond for MTP (blue) and MTP-ZBL (red) potentials.	68
5.1	Inelastic neutron scattering data from NaBr single crystal. Each panel is normalized with respect to its total inelastic intensity (data are on a linear scale).	76
5.2	Illustration on band elimination technique. (a) sTDEP phonon dispersions along high-symmetry directions at 300 K. (b) phonon line-shapes at 300 K where contributions from three-phonon processes associated with transverse optical mode are set to zero. (c) harmonic modes that give the maximum contribution to the second harmonic spectral lineshape through three-phonon processes.	77
5.3	Vibrational spectra of NaBr obtained with autocorrelation function analyses. (left column) Phonon dispersions along high-symmetry directions calculated by projected velocity-velocity autocorrelation function method. (right column) Temperature dependence of vibrational spectrum at particular q -cuts. Temperatures from top to bottom: 650 K, 550 K, 425 K, and 300 K.	78
5.4	Predictions of the classical model of a nonlinear medium (solid red line) for experimental spectra (open circles) at 300 K for (a) $\vec{Q} = [0.6 \ 0 \ 0.6]$, (b) $[0.6 \ 0 \ 0]$, (c) $[0.75 \ 0 \ 0.75]$, (d) $[1 \ 0 \ 0]$	80
5.5	Results from the Heisenberg–Langevin model for SHG at 300 K in the medium-strong coupling regime. (left) Spectral function from Heisenberg–Langevin applied to two coupled TO phonons. (right) Intensity distribution between TO, IPS and SHG.	82

5.6	Temperature dependence of averaged vibrational spectra: left and center columns - vibrational spectra at 300 K, 425 K, 550 K, 650 K with fitted peaks. Spectra are normalized to 1. (bottom left) temperature dependence of the phonon breadth, and (bottom right) phonon energy shift, with respect to 300 K data for transverse optical (TO) mode and second harmonic generation (SHG). Slopes of the bottom plots are presented in the text.	83
5.7	Calculated sTDEP phonon dispersions along high-symmetry directions for temperatures from top to bottom: 650 K, 550 K, 425 K, and 300 K.	88
5.8	Temperature dependence of averaged vibrational spectra at high symmetry points of NaBr Brillouin zone: a)-f) - [0.4 0 0]; g)-l) - [0.6 0 0]; m)-r) - [0.6 0 0.6]; m)-r) - [0.2 0 0.2]. The panels e), f), k), l), q), r), w), x) correspond to the temperature dependence of the phonon lifetime and energy shift with respect to 300 K data for transverse optical mode (TO) and second harmonic generation (SHG) (slope of the data temperature dependence is given in the caption). Other panels show vibrational spectra at 300 K, 425 K, 550 K, 650 K with fitted peaks.	91
5.9	Temperature dependence of thermal occupation of (left) TO mode, and (right) SHG. Red solid line is a fit to the model function representing the sum of occupancy factors related to one and two phonon processes as fit with Eq. 5.26 for the TO mode at left and Eq. 5.20 for SHG at right.	92
6.1	Inelastic neutron scattering data from Zn single crystal (a)-(d) with phonon DOS (e)-(h). Each panel is normalized with respect to its total inelastic intensity (data are on a log scale).	99
6.2	Inelastic neutron scattering data from Zn single crystal at 15 K with fine spectral features (data are on a log scale).	100

6.3	Band elimination analyses of Zn vibrational spectra. (a) sTDEP phonon dispersions along high-symmetry directions at 15 K. (b) Phonon lineshapes at 15 K where contributions from three-phonon processes associated with the optical modes in the range of 22 to 24 meV are set to zero. (c) Harmonic modes that give the maximum contribution to the second harmonic spectral lineshape through three-phonon processes at 40 meV, and (e) 35 meV. Coupling at K high symmetry point over the Brillouin zone of hexagonal crystal projected on the q_x, q_y plane at 40 meV (d) and 35 meV (f).	101
6.4	Phonon dispersions along high-symmetry directions calculated with classical MD and projected velocity-velocity autocorrelation function method. Temperatures from top to bottom: 15 K, 300 K, 500 K, 690 K.	104
6.5	Results from the Heisenberg–Langevin model for high energy diffuse intensity formation at 15 K in the medium-strong coupling regime. . .	105
6.6	Mode Grüneisen parameters for dispersions, shaded to match their corresponding dispersions at (a-b) 15 K and (d-e) 300 K. Phonon dispersions from sTDEP calculations at (c) 15 K and (f) 300 K colored to correspond with their matching mode Grüneisen parameters. . . .	106
6.7	Computational lattice constants (left and center) and volume (right) as a function of temperature of hexagonal Zn. Path Integral MD and sTDEP calculations are shown with red and blue dots, respectively. Classical MD simulation and static relaxation calculation at zero temperature are shown with dashed black line and black dot. (Inset) Calculations at temperatures with NTE.	107
6.8	Calculated and experimental coefficients of linear thermal expansion of a-axis (left) and c-axis (right) of hexagonal Zn. Calculations are shown with circles (PIMD with MTP, red; PIMD with RANN, cyan; QH calculation, orange). Experimental data from Channing and Weintraub and McCannon are presented with diamond and triangle markers. Crosses are from present X-ray diffraction measurements of zinc powder.	108
6.9	Intensity cut at K high symmetry point at $E = 15$ meV as a function of temperature.	110
6.10	Zn single-crystal with vanadium sample holder.	110
6.11	Zinc X-ray diffraction patterns measured from 30 to 100 K. Peaks are indexed. Positions of diffractions are shown with blue markers. . . .	112

6.12	Temperature dependence of the lattice parameters of Zinc extracted from X-ray diffraction data. Confidence intervals are shown with errorbars.	113
6.13	Calculated sTDEP phonon dispersions along high-symmetry directions for temperatures from top to bottom: 15 K, 300 K, 500 K, and 690 K.	116
6.14	Phonon dispersions along high-symmetry directions calculated by projected velocity-velocity autocorrelation function method at 15 K using BCMD.	117
6.15	Convergence of lattice parameters in the PIMD simulation at 10 K. (a),(b) show limits as the number of beads approach infinity: black dots - NPT simulation results of lattice parameters; solid curve - linear fit of the function $f(1/n_{bead})$; red dot - limit of lattice parameter at number of beads equal approaching infinity. (c),(d) error in lattice parameter estimation with respect to a number of beads (a^* , c^* denote the limit with number of beads approaching infinity).	118
6.16	Instrument parameters for GSAS-II Rietveld refinement.	119
6.17	Results of Rietveld refinement.	119
7.1	Magnetization comparison between DFT data (orange) and collinear spin MLIP (blue) for Fe ₆₈ Pd ₃₂ in the pressure interval from -10 to 40 GPa.	127
7.2	Phonon density of states between DFT data (orange) and collinear spin MLIP (blue) for Fe ₆₈ Pd ₃₂ using a 32-atom supercell in the pressure interval from -10 to 40 GPa (top to bottom).	127
7.3	Phonon density of states using collinear spin MLIP (blue) for Fe ₆₈ Pd ₃₂ with 864 atom supercell in the pressure interval from -10 to 40 GPa (top to bottom).	128
7.4	Schematic of the 2D-TTR experiment, pulse sequence, and time definitions. The polarization of each pulse is indicated in the circles.	128
7.5	Vibrational spectra of ZnS along high symmetry directions (left) and density of states (right) at 300 K computed with TDEP method.	129
7.6	Vibrational spectra from autocorrelation function analyses of cuprite at 700 K. Simulations are performed using MLIP with Cu-O bound splined to ZBL potential at low separations. Dispersions are seen at energies below 100 meV. The right panel is phonon DOS.	130

LIST OF TABLES

<i>Number</i>	<i>Page</i>
3.1 Ranges of parameters used in the active learning process, including temperatures, $T(\text{K})$ and increment, and cubic cell lattice constants, $a(\text{\AA})$ and increment used for each material.	25
3.2 Thermodynamic contributions to the entropy of fusion from experimental computational methods.	33
5.1 Slopes of peaks shift and width temperature dependence in Fig. 5. Slopes are given in $\text{meV}/\text{K}\cdot 10^3$	89
5.2 Fitting parameters for peaks in Fig. 2 of main text. μ and γ are given in meV	90

NOMENCLATURE

- AH.** Anharmonic.
- ARCS.** Wide-Angular Range Chopper Spectrometer.
- BES.** Basic Energy Sciences.
- BZ.** Brillouin zone.
- DFT.** Density Function Theory.
- DII.** Diffuse Inelastic Intensity.
- DOE.** Department of Energy.
- ILM.** Intrinsic Localized Mode.
- INS.** Inelastic Neutron Scattering.
- IPS.** Intermodulation Phonon Sideband.
- LAMMPS.** Large-scale Atomic/Molecular Massively Parallel Simulator.
- MD.** Molecular Dynamics.
- MLIP.** Machine Learning Interatomic Potential.
- MTP.** Moment Tensor Potential.
- NERSC.** National Energy Research Scientific Computing Center.
- NQE.** Nuclear quantum effect.
- NTE.** Negative thermal expansion.
- ORNL.** Oak Ridge National Laboratory.
- QHA.** Qasiharmonic.
- SH.** Second Harmonics.
- SHG.** Second Harmonics Generation.
- SNS.** Spallation Neutron Source.
- VASP.** Vienna Ab initio Simulation Package.

Chapter 1

INTRODUCTION

Life is motion. This general phrase has more to tell us than you think. Not only do we have to constantly move physically as living beings, but the microscopic building blocks of matter themselves are also constantly involved in never-ending motion. When people ask me, "What are you studying?" to shorten years of practice and a pile of books, I describe my research subject in a line that always includes the word for one kind of motion called "vibration."

The things we use in everyday life are built from materials. The choice of material for a particular application is driven by its properties, such as the ability to transfer electric current, heat, or mechanical properties. The characteristics of the materials result from the motion of individual atoms constructing material unseen by the human eye. The increase in temperature enriches this motion, changing material behavior. This thesis focuses on new phenomena in microscopic collective motion inside materials at low and high temperatures.

Imagine tapping a tuning fork and hearing a pure, clear note. Now, tap two forks at once, and you might notice new, unexpected tones emerging from the interaction of sounds. The effect can also be seen in the water waves interfering on the lake's surface or two prism experiments with laser light. These illustrations refer to wave blending phenomena called intermodulation. The atomic vibrations are treated as waves propagating in the solid. Applying analogy to material science, a similar phenomenon is called phonon intermodulation — the interaction of atomic motion waves to create new vibrational patterns, altering how materials behave.

Atomic vibrations can be probed with neutrons. Neutron techniques rely on the neutron changing its momentum and energy in a scattering event. The collected data give insight into the structure and atomic motion of materials. The experimental data presented in the thesis is collected at inelastic neutron scattering experiments, giving the basis for the theoretical discussions on new phenomena in solid-state physics.

Modern computational methods provide a direct comparison to the experiment data. This simulation relies on the material's description from the first principles, where configuration consisting of atoms and surrounding electrons are translated

into potential energy surface. The energy surface is key in determining macroscopic solid properties like stability. Machine learning techniques transfer the accuracy of first principle methods to classical simulations of atomic motion. In the classical limit, the time dependence of atomic positions is obtained using Newton's law. The realistic comparison is achieved with many atoms and requires high-performance computers (HPC) computations.

In Chapter 2 of the thesis, I present background information on techniques used in the study. These include inelastic neutron scattering as the major experimental technique. For the computational techniques, I focus on computations based on Density Functional Theory as the first principle model, Many-Body theory for anharmonic phonons, and Molecular Dynamics (MD) for accurate macroscopic anharmonicity treatment.

Chapter 3 discusses the contributions to the entropy of melting. The computations provides data for elements that can not be accessed experimentally. In the chapter I discuss Bayesian learning of thermodynamic integration technique, that allows accurate estimation of the entropy difference upon melting of elements through large scale Molecular Dynamics (MD) simulation. Combining theory and experiment we found out that excess entropy of fusion (compared to richargs rule) is proportional to vibrational contribution. Additionally, excess configurational part shows proportionality with respect to vibrational part of the entropy.

Chapter 4 presents study of diffuse inelastic intensity (DII) in cuprite. DII is a new concept in the field of neutron scattering. DII arises from random phase shifts of atomic vibrations in strongly anharmonic solids. In the vibrational spectra of cuprite measured by inelastic neutron scattering, it appears at high temperatures as a featureless background that overwhelms phonon dispersions. I show how the DII can be reproduced in classical molecular dynamics simulations with machine learning interatomic potential modified to account for hard wall collisions at low atomic separations.

Chapter 5 addresses the second harmonic generation from anharmonic phonons in sodium bromide. I observed a new feature in the inelastic neutron scattering experiment. Using computations, I identified the origin of the new feature. Nonlinear optics was applied to the phonon intermodulation theory to describe the intensity distribution between modes and estimate characteristic anharmonic coupling strength. The temperature dependence of the second harmonics showed that intermodulation results in the formation of coherent excitation of vibrations generated through the coupling of modes of the same frequency in the thermodynamic equilibrium.

Chapter 6 focuses on intermodulation phenomena in hexagonal Zinc single crystals at low temperatures. I show that anharmonic coupling of zero point oscillations is responsible for the formation of diffuse intensity at high energies in inelastic neutron scattering spectra. Additionally, I explore how anharmonic effects at low temperatures result in negative thermal expansion in zinc, an effect of material decreasing in volume upon heating.

Chapter 7 discusses future directions. This includes computational perspectives on the interaction of dipole, spin, and lattice degrees of freedom, new possibilities for intermodulation studies for optical materials, and possible experiments for future more detailed exploration of the DII.

Chapter 2

BACKGROUND

2.1 Introduction

The phonon, a quasiparticle of atom vibrations, is a fundamental concept in solid-state physics. It describes the collective motion of atoms in the material, where individual atoms experience mostly local interactions. In the first approximation, these vibrational dynamics are presented in terms of the normal modes of the crystal lattice. In this formulation, the vibrations can be quantized. The elementary quanta of the excitation is called phonon.

In the thesis, I use experimental, computational, and theoretical methods to study anharmonic phonon behavior in solids. The experiment provides the basis for the phenomenon's existence. The computations complement experiments by providing a ready-to-use toolbox of existing theory. If the same result can be obtained in simulation, what is left is to design a theory that interprets the observations. These are the steps I tried to follow at work.

2.2 Neutron Scattering

Experimentally, one of the most informative ways to study phonon behavior is inelastic neutron scattering (INS). The source of observation in the scattering experiment lies in the deviation of neutron motion interacting with the crystal lattice. The motion of the neutron is characterized by energy E and momentum \vec{k} . In the scattering event, the neutron changes its energy $\Delta E = E_i - E_f$, and momentum $\vec{Q} = \vec{k}_i - \vec{k}_f$ through interaction with the crystal nucleus. If the change in energy equals 0, the scattering is called elastic. For inelastic scattering, the initial energy of the neutron, E_i , before hitting the target is different from the energy E_f after the interaction. The momentum transfer \vec{Q} is related to the neutron propagation wavevector. The amplitude of the wavevector is associated with the energy transfer by Planck's constant \hbar . I present a schematic diagram of the scattering event in Fig. 2.1

Let us introduce the notion of neutron cross section σ_s . Mathematically, the scattering cross section is the number of neutrons scattered Φ_s related to the total flux of neutrons coming from the source Φ_0 . For neutron scattering, the more critical

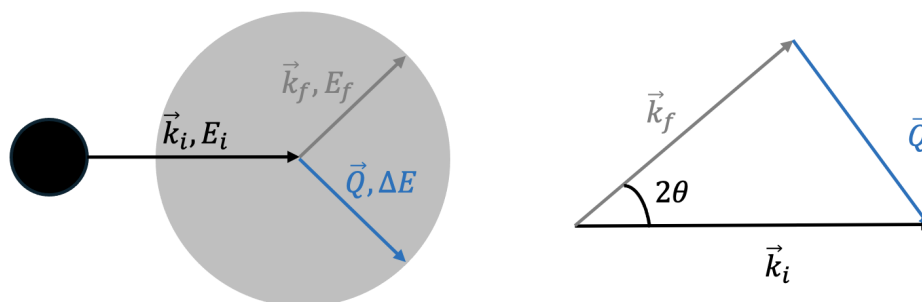


Figure 2.1: Illustration of the neutron scattering event. On the left, the incident neutron with momentum \vec{k}_i and energy E_i scatters off the sample changing momentum to \vec{k}_f and energy E_f . This results in the formation of the phonon with energy ΔE and momentum \vec{Q} . On the right, the triangular diagram of the momentum conservation law.

role is played by its differential analog. In this case, we are looking for the number of neutrons scattered at a particular solid angle $d\Omega$, having a final energy in the interval $\{E_f, E_f + dE_f\}$. The resulting cross section is called partial differential cross section (PDCS):

$$\sigma_s = \frac{\Phi_s}{\Phi_0}, \quad PCDT = \frac{d^2\sigma}{d\Omega dE_f}. \quad (2.1)$$

The PDCS obtained in the neutron experiment gives information about lattice dynamics of the material. It can be directly related to the quanta of lattice vibration operators \hat{A}, \hat{A}^\dagger . To be more accurate, the observable quantity is the autocorrelation function of these operators $\langle \hat{A}^\dagger(t_0)\hat{A}(t_1) \rangle$. The autocorrelation function shows the correlation of atomic motion in material separated by time evolution between t_0 and t_1 . Since it depends only on differences in time, in the matter of notation, t_0 is taken as 0, and t_1 is denoted as t . Since the possible scattering events are restricted by phonon excited in the particular material, scattering can be directly related to the phonon autocorrelation function

$$\frac{d^2\sigma}{d\Omega dE_f} = \frac{|\vec{k}_f|}{|\vec{k}_i|} \frac{\sigma}{4\pi\hbar} \int_{-\infty}^{\infty} \langle \hat{A}^\dagger \hat{A}(t) \rangle \exp(-i\omega t) dt. \quad (2.2)$$

I changed the notation here, replacing energy transfer ΔE with the corresponding frequency of excited phonon ω .

Thus, measuring the partial differential cross section along with momentum and energy transfer gives information about the vibrational properties of the material.

If I omit the terms in the Eq. 2.2 that correspond to particular experimental setup ($|\vec{k}_f|, |\vec{k}_i|, \sigma$), I am left with

$$S(\vec{Q}, \omega) = \frac{1}{2\pi\hbar} \int_{-\infty}^{\infty} \langle \hat{A}^\dagger \hat{A}(t) \rangle \exp(-i\omega t). \quad (2.3)$$

S is called the dynamical structure factor and is only material dependent.

Precise measurement of PDCS as a function of momentum and energy transfer can be done with a highly focused neutron beam. Hence, all the experiments shown in this thesis are performed on a Wide-Angular-Range Chopper Spectrometer (ARCS) [1] at the Spallation Neutron Source (SNS) [2] at Oak Ridge National Laboratory (ORNL). Fig. 2.2 shows details of ARCS instruments with individual components labeled.

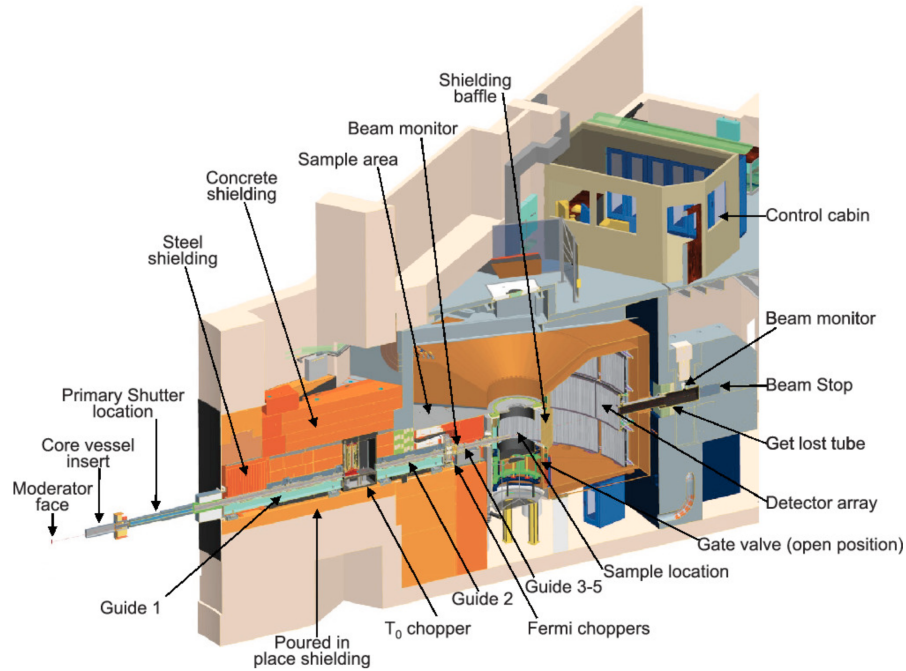


Figure 2.2: Scheme of the ARCS instrument with labeled components.

ARCS is a time-of-flight instrument. In the measurements, the neutrons are collected in the event mode. Each neutron coming to the detector is characterized by the arrival time and position on a two-dimensional detector bank. The third spatial dimension is given by the distance between the sample and the detector and by the relation between the neutron energy and the wavevector.

Three types of solid materials samples are used in INS experiments: single-crystal, polycrystalline, and powders. In the thesis, I focus on single-crystal experiments.

The main feature of the single crystal is its ideal periodic lattice arrangement. It can be considered a toy model to study the properties of the materials in the absence of defects and distortions. Since the single-crystal is perfectly periodic, I can get information about high symmetry points of particular lattices from the INS dataset. The information on the material behavior at high symmetry points allows one to perform analyses of material properties without exploring the entire Brillouin Zone (BZ).

2.3 Vibrations in solid

The solids are modeled as a periodic system of nuclei with point mass. The nucleus lives in the potential energy surface formed by light electrons. In the Born-Oppenheimer approximation, the motion of electrons and displacement of nuclei live on different time scales [3].

The Hamiltonian of the lattice motion has the form

$$H = \sum_I \frac{p_I^2}{2M_I} + \Phi, \quad (2.4)$$

where M_I is the nuclear mass and Φ is the potential energy term.

Assuming that the nucleus vibrates around the equilibrium position, we expand the Φ with respect to displacement.

$$\Phi = U_0 + \sum_{i\alpha} \Phi'_{i\alpha} u_i^\alpha + \frac{1}{2!} \sum_{ij\alpha\beta} \Phi''_{ij} u_i^\alpha u_j^\beta + \frac{1}{3!} \sum_{ijk\alpha\beta\gamma} \Phi'''_{ijk} u_i^\alpha u_j^\beta u_k^\gamma + \dots, \quad (2.5)$$

where Φ' , Φ'' , and Φ''' are coefficients of the expansion. In equilibrium Φ' cancels out. The harmonic limit treats order three coefficients Φ''' and higher to be zero.

In the harmonic approximation, atomic displacement can be decomposed in a sum of crystal normal modes

$$\vec{u}_i = \frac{1}{\sqrt{m_i}} \sum_{\vec{q}} A_{\vec{q}} \vec{\epsilon}_{\vec{q}}^i e^{i(\vec{q} \cdot \vec{R} - \omega_{\vec{q}} t)}. \quad (2.6)$$

The \vec{q} is the wave vector, $A_{\vec{q}}$, $\epsilon_{\vec{q}}^i$, and $\omega_{\vec{q}}$ are the wavevector, the amplitude, polarization and the frequency of the normal mode, respectively.

The frequency and the polarization vector are found by solving eigenvalue problem of dynamical matrix $\Phi(\vec{q})$:

$$\omega_{\vec{q}}^2 \epsilon_{\vec{q}} = \Phi''(\vec{q}) \epsilon_{\vec{q}}, \quad \Phi''_{ij}(\vec{q}) = \sum_{\vec{R}} \frac{\Phi''_{ij}(\vec{R})}{\sqrt{m_i m_j}} e^{i\vec{q} \cdot \vec{R}}. \quad (2.7)$$

The Eq. 2.5 in the limit of small displacements strongly connects to perturbation theory applied to crystal potential [4].

$$H = H_0 + \lambda H_3 + \lambda^2 H_4 + \dots, \quad (2.8)$$

where H_0 denote harmonic Hamiltonian, H_3 , H_4 arise from high order phonon-phonon interaction.

In the thesis, I look at the phenomena coming from the H_3 term of the expansion. This term translates into an interaction involving three phonons. Since phonons obey Bose-Einstein statistics, the third order part of the Hamiltonian in Eq. 2.5 $\frac{1}{3!} \sum_{ijk\alpha\beta\gamma} \Phi_{ijk}^{\alpha\beta\gamma} u_i^\alpha u_j^\beta u_k^\gamma$ can be directly related to a three phonon process by replacing u_i^α in terms of phonon creation and annihilation operators, $\hat{x}_{\vec{q}i} = \hat{a}_{-\vec{q}i}^\dagger + \hat{a}_{\vec{q}i}$, where \mathbf{q} is the phonon momentum in the reciprocal space of the crystal lattice. The resulting Hamiltonian has a form

$$H_3 = \frac{1}{3!} \sum_{\mathbf{q}\mathbf{q}'\mathbf{q}''} \sum_{ijk} \frac{\hbar^{3/2}}{2^{3/2} N^{1/2}} \frac{\Phi(\vec{q}i, \vec{q}'j, \vec{q}''k)}{\sqrt{\omega_{\vec{q}i} \omega_{\vec{q}'j} \omega_{\vec{q}''k}}} \delta_{\vec{q}+\vec{q}'+\vec{q}'', \vec{G}} \\ \times (\hat{a}_{-\vec{q}i}^\dagger + \hat{a}_{\vec{q}i}) (\hat{a}_{-\vec{q}'j}^\dagger + \hat{a}_{\vec{q}'j}) (\hat{a}_{-\vec{q}''k}^\dagger + \hat{a}_{\vec{q}''k}), \quad (2.9)$$

where $\omega_{\vec{q}i}$, $\omega_{\vec{q}'j}$, and $\omega_{\vec{q}''k}$, are frequencies of the harmonic oscillator; $\Phi(\vec{q}i, \vec{q}'j, \vec{q}''k)$ is the three phonon scattering intensity, and \vec{G} is the reciprocal lattice vector. The operator part in the Eq. 2.9 represents some of the following three phonon processes: absorption of the phonon with the formation of two phonons, absorption of two phonons with the formation of the phonon, and spontaneous formation and absorption of three phonons (the last two processes violate the energy conservation law and are usually omitted in practice). The $\Phi(\vec{q}i, \vec{q}'j, \vec{q}''k)$, later denoted as $\Phi_{ss's''}^{\vec{q}\vec{q}'\vec{q}''}$ for notation purposes, is directly related to the third-order force constants from Eq. 2.5

$$\Phi_{ss's''}^{\vec{q}\vec{q}'\vec{q}''} = \sum_{ijk} \sum_{\alpha\beta\gamma} \frac{\epsilon_s^{i\alpha} \epsilon_{s'}^{j\beta} \epsilon_{s''}^{k\gamma}}{\sqrt{m_i m_j m_k} \sqrt{\omega_{\vec{q},s} \omega_{\vec{q}',s'} \omega_{\vec{q}'',s''}}} \Phi_{ijk}^{\alpha\beta\gamma} \exp [i (\vec{q} \cdot \vec{r}_i + \vec{q}' \cdot \vec{r}_j + \vec{q}'' \cdot \vec{r}_k)], \quad (2.10)$$

where m_i, m_j, m_k are atomic masses for third order matrix element, and $\epsilon_s^{i\alpha}$, $\epsilon_{s'}^{j\beta}$, and $\epsilon_{s''}^{k\gamma}$ are the corresponding normal mode eigenvectors.

The many-body theory relates the result in Eq. 2.9 to the real (Δ) and imaginary ($i\Gamma$) parts of the self-energy of the phonon. The imaginary part is [5–7]

$$\begin{aligned} \Gamma_s^{\vec{q}}(V, T) = & \frac{\hbar\pi}{16} \sum_{\vec{q}'\vec{q}''} \sum_{s',s''} \left| \Phi_{s's''}^{\vec{q}'\vec{q}''} \right|^2 (n_{\vec{q}',s'} + n_{\vec{q}'',s''} + 1) \times \delta(\Omega - \omega_{\vec{q}',s'} - \omega_{\vec{q}'',s''}) \\ & + (n_{\vec{q}',s'} - n_{\vec{q}'',s''}) \left[\delta(\Omega - \omega_{\vec{q}',s'} + \omega_{\vec{q}'',s''}) - \delta(\Omega + \omega_{\vec{q}',s'} - \omega_{\vec{q}'',s''}) \right], \end{aligned} \quad (2.11)$$

where $\hbar\Omega$ is the probing energy from the neutron, $\omega_{\vec{q},s}^2$ are the eigenvalues of the dynamical matrix, and n are the Planck occupancy factors (where $n(\hbar\omega, T)$).

The real part can be found through the Kramers-Kronig transformation of the complex function [5–7]

$$\Delta_{\vec{q},s}(\Omega_{\vec{q},s}) = \frac{1}{\pi} \int \frac{\Gamma(\omega_{\vec{q},s})}{\omega_{\vec{q},s} - \Omega} d\omega_{\vec{q},s}. \quad (2.12)$$

Large deviations of $\Delta_{\vec{q},s}(\Omega_{\vec{q},s})$ from a Lorentzian lineshape are consequences of a high degree of anharmonicity.

Another important classification can be made on the basis of Eq. 2.5. The quasiharmonic (QH) approximation assumes that terms beyond Φ'' are zero but allow terms to depend on volume $\Phi'' = \Phi''(V)$. In the anharmonic (AH) expansion, all terms Φ'' and Φ''' are treated as functions of volume V and temperature T .

The vibrational part of the Helmholtz free energy is

$$F_{\text{vib}} = \sum_{\vec{q},\nu} \left[\frac{1}{2} \hbar\omega_{\vec{q},\nu} + k_B T \ln(1 - e^{-\beta\hbar\omega_{\vec{q},\nu}}) \right]. \quad (2.13)$$

In the AH approximation $F_{\text{vib}} = F(T, V)$ through renormalization of frequencies $\omega_{\vec{q},\nu}(T, V)$, while in QH approximation F_{vib} depends explicitly on volume, and implicitly on temperature as $V(T)$.

Phonon intermodulation phenomena

A harmonic theory of lattice dynamics treats phonons as independent, noninteracting normal modes with long lifetimes. The Born – von Kármán model of a periodic crystal predicts up to $3R$ branches for a crystal with R number of atoms in its unit cell. Approaches based on many-body perturbation theory for anharmonic interactions [5, 7, 8] account for thermal shifts and finite lifetime of these $3R$ branches through three- and four-phonon scattering, and the numbers and degeneracies of these phonon branches have been consistent with most measurements by inelastic

neutron scattering (INS) on single crystals. Modern techniques for INS on single crystals have enabled the observation of new phonon branches in addition to the $3R$ expected for a harmonic crystal [9–13]. Experimental investigations of NaI ionic crystal revealed a low-energy “intrinsic localized mode” (ILM) [9, 10], which can alter thermal transport properties [11, 12]. In NaBr, this ILM was found to be a lower sideband from intermodulations of TA and TO modes and their upper sideband was found [13]. These findings of intermodulation phonon sidebands (IPS) were supported by a quantum Langevin model for intensity redistribution and independent calculations with many-body perturbation theory.

For a classical picture, assume the initial phonon wavefunction ψ_{in} is a superposition of two waves with frequencies ω_a and ω_b

$$\psi_{in} = \psi_{in}^a + \psi_{in}^b, \quad (2.14)$$

$$\begin{aligned} \psi_{in} &= A(e^{i\omega_a t} + e^{-i\omega_a t}) \\ &+ B(e^{i\omega_b t} + e^{-i\omega_b t}). \end{aligned} \quad (2.15)$$

. With a quadratic nonlinearity, the response of the medium, ψ_{out} , is

$$\psi_{out} = \eta\psi_{in} + \epsilon\psi_{in}^2 + \dots \quad (2.16)$$

Substituting ψ_{in} from Eq. 2.15 into $\epsilon\psi_{in}^2$ of Eq. 2.16 generates a pair of cross terms with frequencies $\omega_a + \omega_b$ and $\omega_a - \omega_b$, the “intermodulation phonon sidebands” [13], and “second harmonics” with frequencies $2\omega_a$ and $2\omega_b$. The cross terms have been observed at modest temperatures by INS measurements on NaBr [13].

Temperature Dependent Effective Potential

One way to estimate terms in Eq. 2.5 is by minimizing the difference between forces predicted by model Hamiltonian $F_{TDEP}^{i\alpha} = \sum_{j\beta} \Phi_{ij}''^{\alpha\beta} u_j^\beta + \frac{1}{2} \sum_{jk\beta\gamma} \Phi_{ijk}'''^{\alpha\beta\gamma} u_j^\beta u_k^\gamma$ and a reference model $F_{ref}^{i\alpha}$. The usual choice for the reference model is density functional theory. The coefficients $\Phi_{ij}''^{\alpha\beta}$, and $\Phi_{ijk}'''^{\alpha\beta\gamma}$ are parameterized with symmetrically irreducible set Θ , which is found in the optimization problem

$$\min_{\Theta} ||F_{TDEP}(\Theta) - F_{DFT}||^2. \quad (2.17)$$

The stochastic temperature-dependent effective potential (sTDEP) [14–17] was used throughout the work. In short, the method obtains coefficients for a model Hamiltonian using an ensemble average of the Hellman-Feynman forces in an *ab initio*

simulation of supercells with thermally displaced atoms. The model potential explicitly includes cubic anharmonicity by obtaining third-order order force constants at finite temperatures. These third-order force constants are used to calculate real and imaginary parts of the phonon self-energy, following the many-body perturbation theory [5, 18] as in Eq. 2.11 and Eq. 2.12.¹

2.4 Moment Tensor Potential (MTP)

In the thesis, lattice dynamics simulations were performed with the moment tensor potential (MTP). In this model, the total interaction energy of the structure is presented as the sum of the atomic contributions $V(\mathbf{r}_i)$. Here, \mathbf{r}_i is the atomic neighborhood encoded in the set of vectors connecting atom i with the neighboring atoms j , $\mathbf{r}_i = \{r_{ij}\}$. Each contribution $V(\mathbf{r}_i)$ is expanded as a linear combination of basis functions $B_k(\mathbf{r}_i)$. Thus, the total energy of a configuration x could be written as

$$E(x) := \sum_{i=1}^N \sum_k \theta_k B_k(\mathbf{r}_i), \quad (2.18)$$

where N is the number of atoms in the configuration x , θ are the adjustable parameters to be found by minimizing the difference between $E(x)$ and the DFT energy, together with forces and virial stresses of the training set of configurations x . The basis functions are constructed as different contractions of moment tensor descriptors of atomic environments

$$M_{\mu,\nu}(u) := \sum_{i=1}^n |u_i|^{2\mu} u_i^{\otimes \nu}(u), \quad (2.19)$$

where integers $\mu, \nu \geq 0$ index different descriptors, and $u^{\otimes \nu}$ is the Kronecker product of ν copies of the vector u . This functional form respects all the physical symmetries. The details can be found in [19, 20].

There are two methodologies for assembling a training set. The first one is passive learning; the potential is trained using the whole dataset of structures processed by the reference model. This approach requires a large dataset of reference model (DFT, in our case) calculations to cover the system's phase space. Learning on-the-fly or active learning (AL) methodology enables a potential to be trained automatically only on configurations where significant extrapolation is detected. In this case, only a few configurations required for the phase space of the system description

¹The quartic in the potential energy expansion has the same inversion symmetry as the quadratic, so it is not practical to fit a quartic term independently. Nevertheless, the effects of the quartic term are accounted for, approximately, by the static offset and the quadratic term.

are processed by the reference model. This approach significantly decreases the number of DFT calculations required for potential training. The technique is one of the advantages of using MTP, which makes it highly efficient for on-the-fly learning [21, 22].

The main advantage of MTP potential for material science calculations is its flexible form. This allows training the potential by minor tuning of the basis set during the MD run. Another advantage is learning on the fly, significantly reducing the number of reference model calculations.

Velocity-velocity correlation functions

Correlation functions provide statistical relationships between random variables. The correlation $C(x, t)$ of the random variable $A(x)$, a function of space, and $B(t)$, a random function of time is

$$C(x, t) = \langle A(x)B(t) \rangle , \quad (2.20)$$

where the brackets represent the expectation value of the variables. For correlations of random independent variables of vector functions, Eq. 2.20 is modified for vector components

$$C_{ij}(x, t) = \langle A_i(x)B_j(t) \rangle . \quad (2.21)$$

Here $C_{ij}(x, t)$ is the ij^{th} component of the correlation matrix, written as

$$C(x, t) = \sum_i \sum_j \langle A_i(x)B_j(t) \rangle . \quad (2.22)$$

Studies of lattice dynamics require time and space relationships. Autocorrelation functions give correlations of the same quantity at two distinct points. For random variables $A(x)$ and $B(t)$

$$C_{AA}(x_1, x_2) = \langle A(x_1)A(x_2) \rangle \quad (2.23)$$

and

$$C_{BB}(t_1, t_2) = \langle B(t_1)B(t_2) \rangle , \quad (2.24)$$

for the spatial autocorrelation of A , C_{AA} , and the temporal autocorrelation of B , C_{BB} .

For phonon dispersions, we want the autocorrelation of the position of an atom at two different times. This is equivalent to knowing the vibrational response of materials

and corresponds to the construction of the Van Hove function [5] we evaluated the correlation with the mode-projected velocity, a form of current density

$$\vec{j}(\vec{q}, t) = \sum_i^N \vec{v}_i(t) \exp[i\vec{q} \cdot \vec{r}_i(t)]. \quad (2.25)$$

Here \vec{q} , $\vec{r}_i(t)$, and $\vec{v}_i(t)$ are the respective wavevector, position, and mass-weighted velocity of atom i at time t . The Fourier transforms of the current autocorrelation function $\langle \vec{j}(t, \vec{q}) \vec{j}(0, -\vec{q}) \rangle$ give a vibrational density of states at a particular point of the Brillouin zone,

$$g(\omega, \vec{q}) = \int_0^\infty \langle \vec{j}(t, \vec{q}) \vec{j}(0, -\vec{q}) \rangle \exp(-i\omega t) dt. \quad (2.26)$$

Unlike perturbation theory methods, autocorrelation methods contain all orders of anharmonicity. However, autocorrelation functions require substantially larger time and length scales to reach convergence than methods based on perturbation theory.

Thermodynamic properties such as vibrational entropy and free energy play a significant role in determining system stability at finite temperatures. These qualities can be calculated directly from the vibrational density of states. The velocity autocorrelation function (VACF) method is used as in Eq. 2.26 to reproduce the vibrational density of states with anharmonic effects. VACF $\langle v(t)|v(0) \rangle$ can be calculated explicitly from molecular dynamics simulation. The Fourier transform of the VACF obtains the vibrational density of states [23].

$$g(\nu) = \int_0^\infty \cos 2\pi\nu t \frac{\langle \overline{v(0)v(t)} \rangle}{\langle \overline{v(0)^2} \rangle} dt, \quad (2.27)$$

where ν is the vibrational frequency, and the average $\langle \overline{\bullet} \rangle$ is taken over all atoms. The advantage of such a method is its high accuracy in the vibrational density of states description. On the other hand, calculation for large system should be performed to achieve this accuracy, so one can use *ab initio* molecular dynamics only for very approximate calculations [24].

References

- [1] D. L. Abernathy, M. B. Stone, M. J. Loguillo, M. S. Lucas, O. Delaire, X. Tang, J. Y. Y. Lin, and B. Fultz. Design and operation of the wide angular-range chopper spectrometer ARCS at the Spallation Neutron Source. *Rev. Sci. Instrum.*, 83(1):015114, 2012. doi: 10.1063/1.3680104. URL <https://doi.org/10.1063/1.3680104>.
- [2] T.E. Mason, D. Abernathy, I. Anderson, J. Ankner, T. Egami, G. Ehlers, A. Ekkebus, G. Granroth, M. Hagen, K. Herwig, J. Hodges, C. Hoffmann, C. Horak, L. Horton, F. Klose, J. Larese, A. Mesecar, D. Myles, J. Neufeind, M. Ohl, C. Tulk, X-L. Wang, and J. Zhao. The Spallation Neutron Source in Oak Ridge: A powerful tool for materials research. *Physica B Condens. Matter*, 385-386:955–960, 2006. ISSN 0921-4526. doi: 10.1016/j.physb.2006.05.281. URL <https://www.sciencedirect.com/science/article/pii/S092145260601177X>.
- [3] M. Born. Born-Oppenheimer approximation. *Ann. Phys.*, 84:457–484, 1927.
- [4] P. Aynajian. *Electron-phonon interaction in conventional and unconventional superconductors*. Springer Science & Business Media, 2011.
- [5] A. A. Maradudin and A. E. Fein. Scattering of neutrons by an anharmonic crystal. *Phys. Rev.*, 128:2589–2608, 1962. doi: 10.1103/PhysRev.128.2589. URL <https://link.aps.org/doi/10.1103/PhysRev.128.2589>.
- [6] R. A. Cowley. Anharmonic crystals. *Rep. Progr. Phys.*, 31(1):123, jan 1968. doi: 10.1088/0034-4885/31/1/303. URL <https://dx.doi.org/10.1088/0034-4885/31/1/303>.
- [7] D. C. Wallace and H. Callen. Thermodynamics of crystals. *Am. J. Phys.*, 40(11):1718–1719, 1972.
- [8] G. Grimvall. *Thermophysical properties of materials*. Elsevier, 1999.
- [9] M. E. Manley, A. J. Sievers, J. W. Lynn, S. A. Kiselev, N. I. Agladze, Y. Chen, A. Llobet, and A. Alatas. Intrinsic localized modes observed in the high-temperature vibrational spectrum of NaI. *Phys. Rev. B*, 79(13):134304, 2009.
- [10] M. E. Manley, D. L. Abernathy, N. I. Agladze, and A. J. Sievers. Symmetry-breaking dynamical pattern and localization observed in the equilibrium vibrational spectrum of nai. *Sci. Rep.*, 1(1):4, 2011.
- [11] M. E. Manley, J. W. Lynn, D. L. Abernathy, E. D. Specht, O. Delaire, A. R. Bishop, R. Sahul, and J. D. Budai. Phonon localization drives polar nanoregions in a relaxor ferroelectric. *Nat. Commun.*, 5(1):3683, 2014.

- [12] M. E. Manley, O. Hellman, N. Shulumba, A. F. May, P. J. Stonaha, J. W. Lynn, V. O. Garlea, A. Alatas, R. P. Hermann, J. D. Budai, et al. Intrinsic anharmonic localization in thermoelectric pbse. *Nat. Commun.*, 10(1):1928, 2019.
- [13] Y. Shen, C. N. Saunders, C. M. Bernal, D. L. Abernathy, T. J. Williams, M. E. Manley, and B. Fultz. Prediction and observation of intermodulation sidebands from anharmonic phonons in NaBr. *Phys. Rev. B*, 103(13):134302, 2021.
- [14] O. Hellman, I. A. Abrikosov, and S. I. Simak. Lattice dynamics of anharmonic solids from first principles. *Phys. Rev. B*, 84:180301, 2011. doi: 10.1103/PhysRevB.84.180301. URL <https://link.aps.org/doi/10.1103/PhysRevB.84.180301>.
- [15] O. Hellman, P. Steneteg, I. A. Abrikosov, and S. I. Simak. Temperature dependent effective potential method for accurate free energy calculations of solids. *Phys. Rev. B*, 87:104111, Mar 2013. doi: 10.1103/PhysRevB.87.104111. URL <https://link.aps.org/doi/10.1103/PhysRevB.87.104111>.
- [16] O. Hellman and I. Abrikosov. Temperature-dependent effective third-order interatomic force constants from first principles. *Phys. Rev. B*, 88:144301, Oct 2013. doi: 10.1103/PhysRevB.88.144301. URL <https://link.aps.org/doi/10.1103/PhysRevB.88.144301>.
- [17] D. S. Kim, Olle Hellman, J. Herriman, H. L. Smith, Jiao Y. Y. Lin, N. Shulumba, J. L. Niedziela, C. W. Li, D. L. Abernathy, and B. Fultz. Nuclear quantum effect with pure anharmonicity and the anomalous thermal expansion of silicon. *Proc. Natl. Acad. Sci. USA*, 115(9):1992–1997, 2018. ISSN 0027-8424. doi: 10.1073/pnas.1707745115. URL <https://www.pnas.org/content/115/9/1992>.
- [18] D. C. Wallace. *Thermodynamics of Crystals*. J. Wiley, New York, 1998.
- [19] A. V. Shapeev. Moment tensor potentials: A class of systematically improvable interatomic potentials. *Multiscale Model. Simul.*, 14(3):1153–1173, 2016. doi: 10.1137/15M1054183. URL <https://doi.org/10.1137/15M1054183>.
- [20] K. Gubaev, E. V. Podryabinkin, G. L. W. Hart, and A. V. Shapeev. Accelerating high-throughput searches for new alloys with active learning of interatomic potentials. *Comp. Mat. Sc.*, 156:148–156, January 2019. ISSN 0927-0256. doi: 10.1016/j.commatsci.2018.09.031. URL <http://www.sciencedirect.com/science/article/pii/S0927025618306372>.
- [21] E. Podryabinkin and A. Shapeev. Active learning of linearly parametrized interatomic potentials. *Comput. Mat. Sci.*, 140:171–180, 2017.
- [22] I. S. Novikov, K. Gubaev, E. V. Podryabinkin, and A. V. Shapeev. The MLIP package: moment tensor potentials with MPI and active learning. *Mach. Learn.: Sci. Technol.*, 2(2):025002, 2020. doi: 10.1088/2632-2153/abc9fe.

- [23] J. Dickey and A. Paskin. Computer simulation of the lattice dynamics of solids. *Phys. Rev.*, 188(3):1407, 1969.
- [24] D. V. Minakov, P. R. Levashov, and V. B. Fokin. Vibrational spectrum and entropy in simulation of melting. *Comp. Mat. Sci.*, 127:42–47, 2017.

Chapter 3

BAYESIAN LEARNING OF THERMODYNAMIC
INTEGRATION APPLIED TO ATOMISTIC ORIGIN OF THE
ENTROPY OF MELTING

Bayesian learning thermodynamic integration formulation is taken from "Bayesian learning of thermodynamic integration and numerical convergence for accurate phase diagrams" [1] For the entropy of melting of elements, I refer to "Atomistic origin of the entropy of melting from inelastic neutron scattering and machine learned molecular dynamics" [2].

Melting is the iconic first-order phase transition where a material changes from a solid to a liquid at the melting temperature, T_m . In equilibrium, this occurs when the Gibbs free energy,

$$G = U - TS + PV, \quad (3.1)$$

of the solid equals that of the liquid. The energy absorbed at T_m , the latent heat, is defined as $L = T_m \Delta S_{\text{fus}}$, where ΔS_{fus} is the entropy of fusion. The definition of L corresponds to the condition $\Delta G = G_l - G_s = 0$, and ΔS_{fus} results from the inequality of $\partial G / \partial T$ for the solid and liquid at T_m .

Estimating T_m is central to many investigations [3–6]. A well-known predictor is the Lindemann criterion, which states that melting occurs when the square root of the mean-squared atom displacement reaches approximately 10% of the interatomic distance [7]. While it has had some success, its conceptual basis includes only the solid phase. An effort to include the thermodynamics of the liquid in this criterion led to mixed results [8]. More recently, advances in computational methods [9, 10] have allowed for increasingly accurate melting temperature predictions for various materials [11–13].

Despite the improvements in predicting melting temperatures, work remains to codify the thermodynamics of melting. To date, a common “rule” for the entropy of fusion is the empirical Richard’s rule, which states $\Delta S_{\text{fus}} \approx 1.1 k_{\text{B}}$ per atom for monatomic systems [14]. Elements with much larger entropies of fusion are considered to melt anomalously (see Fig. 3.1) [15]. Some efforts to explain these anomalies consider a separation of the entropy of fusion into components from changes in atomic vibrations, configurations, and electronic excitations [16–18]

$$\Delta S_{\text{fus}} = \Delta S_{\text{fus,vib}} + \Delta S_{\text{fus,config}} + \Delta S_{\text{fus,el}}. \quad (3.2)$$

Experimentally quantifying these atomic components of the entropy of fusion is a challenge. However, methods that measure the dynamic response function, such as neutron or x-ray scattering, show promise for identifying and analyzing vibrational motion in liquids [19–22]. For solids, using vibrational spectra for assessing the vibrational entropy is well established for scattering techniques [23–25]. Extending these analyses to the liquid state is difficult owing to the quasielastic scattering from diffusion, which widens the intense elastic peak to cover the vibrational spectra at low energies. In fact, most neutron studies on liquid dynamics focus on diffusion.

Here, advances in experimental and computational methods were used to quantify the thermodynamic contributions to the entropy of fusion in pure elements. Simulations used molecular dynamics with machine-learning interatomic potentials for Ge, Si, Pb, and Li. The computations complement time-of-flight (TOF) inelastic neutron scattering (INS) experiments on Ge, Bi, Sn, and Pb to obtain the vibrational entropy across the melt. To our knowledge, this is the first experimental quantification of the vibrational contribution to melting. Vibrational entropy accounts for most, but not all, of the anomalous deviation from Richard’s rule.

3.1 Thermodynamic Integration with MTP

To reproduce dynamics across the melting transition, machine-learned moment tensor potentials (MTP) [26] for Ge, Si, Pb, and Li were trained on DFT data following [27]. For each element, the MTP potentials were actively trained on the fly by running MD simulations for a grid of volumes and temperatures near melting conditions. The interatomic potentials from this procedure were used to calculate the total change in entropy between the solid and liquid phases of each element with Bayesian learning thermodynamic integration. The vibrational entropy contribution of each phase was calculated from the vibrational density of states (PDOS) obtained from velocity autocorrelation function analyses [28]. The quasielastic peak was

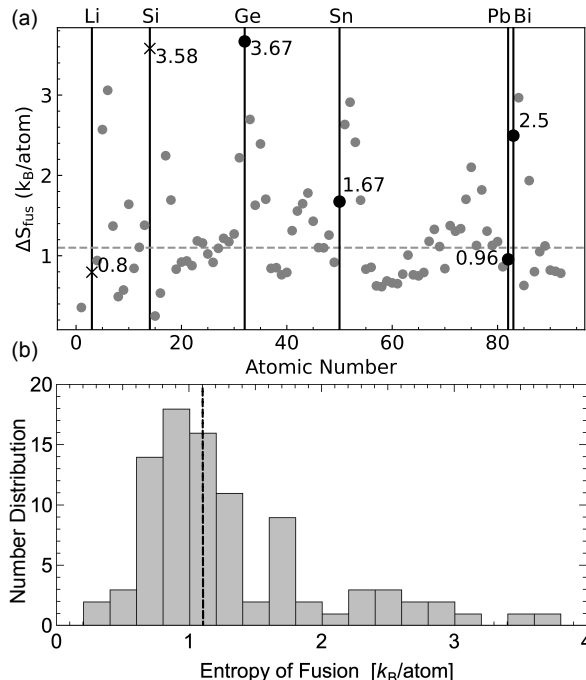


Figure 3.1: Entropies of fusion, ΔS_{fus} , and their number distribution. (a) Entropies of fusion for elements up to uranium, plotted versus atomic number. The elements chosen for this study are indicated by a vertical line and are annotated with the value of their entropy of fusion. Circles (crosses) designate experimentally (computationally) studied elements. (b) Distribution of ΔS_{fus} for the first 92 elements. The dashed lines in (a) and (b) show Richard’s rule of $1.1 k_B$ per atom.

subtracted from the total PDOS for the liquid phase. Additional details on MLIP construction and computational data analyses are given below.

Theory of Bayesian learning thermodynamic integration

In the current section, we will obtain the relations between free energy derivatives and statistical averages as will be used by Gaussian processes. In what follows, we distinguish the extensive and intensive quantities in the notation: the former will have a hat accent: \hat{E} , \hat{V} . The corresponding intensive, per-atom quantities are $E = \hat{E}/N$, $V = \hat{V}/N$, where N will denote the number of atoms.

Free energy

Let \mathbf{x} be a configuration with N atoms enclosed in a volume \hat{V} (we will interchangeably use \hat{V} for the actual region in space and its measure) with periodic boundary conditions. Let $\hat{E}(\mathbf{x})$ be the potential energy of the interatomic interaction. We assume that the units for the temperature T are the same as for the energy \hat{E} ; in other

words, our Boltzmann constant is $k_B = 1$.

We define the free energy by

$$-T \log \int_{\hat{V}^N} \exp(-\hat{E}(\mathbf{x})/T) d\mathbf{x} = \hat{F}_{ref} - T\hat{S}, \quad (3.3)$$

where \hat{F}_{ref} will be explicitly assigned later (differently for each phase), and we will call \hat{S} the entropy. We will rely on comparing the absolute free energies of different phases (as opposed to the free energy difference between phases); therefore, it is important to choose \hat{F}_{ref} and \hat{S} consistently across phases.

For solid we choose

$$F_{ref}^{(s)} := E_0 + T \left(-\log(NV) + 1 - \frac{3}{2} \log(2\pi T) \right), \quad (3.4)$$

where $E_0 = E_0(V)$ is the potential energy at zero temperature for the given volume. Here and in what follows the superscript (s) denotes the solid phase. Choosing $F_{ref}^{(s)}$ in the form (3.4) is motivated by the fact that in this case the entropy admits a simple low-temperature expansion

$$S^{(s)} = -\frac{1}{2N} \log \det \hat{H} - \log(V) + O(T), \quad (3.5)$$

where \hat{H} is the Hessian of the energy \hat{E} at the equilibrium configuration \mathbf{x}_0 . For the derivation of (3.4) and (3.5), refer to Supplemental Material. A well-defined zero-temperature limit of $S^{(s)}$ such as (3.5) is important for reconstructing the free energy with a Gaussian process, as molecular dynamics can generate the data on derivatives of S and thus allow, without (3.5), one to reconstruct $S^{(s)} = S^{(s)}(T, V)$ only up to an additive constant.

Indeed, an NVT-thermostatted molecular dynamics produces the averages of the form

$$\langle f \rangle := \frac{\int_{\hat{V}^N} f(\mathbf{x}) \exp(-\hat{E}(\mathbf{x})/T) d\mathbf{x}}{\int_{\hat{V}^N} \exp(-\hat{E}(\mathbf{x})/T) d\mathbf{x}}.$$

One can then find that

$$\frac{\partial S^{(s)}}{\partial T} = T^{-2} \langle E - E_0 \rangle - \frac{3}{2} T^{-1}, \quad \text{and} \quad (3.6)$$

$$\frac{\partial S^{(s)}}{\partial V} = T^{-1} \langle P - P_0 \rangle, \quad (3.7)$$

where $P_0 := -\frac{\partial E_0}{\partial V}$ is the pressure at zero temperature. Here, and in what follows by P we denote the virial part of the pressure. The virial pressure is, in fact, easier

to compute from molecular dynamics. The derivation of (3.6) and (3.7) is given in Supplemental.

Also, we consider the liquid and gas phases. A single free energy curve can describe these phases because they are indistinguishable at temperatures above the critical one. Hence, we will denote the corresponding phase by superscript (f) and refer to it as the fluid phase. For the fluid, we simply choose ideal gas as a reference,

$$F_{ref}^{(f)} := -T \log(NV), \quad (3.8)$$

so that

$$\lim_{T \rightarrow \infty} S^{(f)} = \lim_{V \rightarrow \infty} S^{(f)} = 0. \quad (3.9)$$

This equality is a consequence of our definition of free energy in (3.3). In the limit of $T \rightarrow \infty$, the exponent in the integral is approaching one. Hence, the integral itself is equal to NV . In the same manner, when $V \rightarrow \infty$, the interaction between particles is negligible ($\hat{E}(\mathbf{x}) \rightarrow 0$) and the integral also approaches NV .

The derivatives of $S^{(f)}$ are thus

$$\frac{\partial S^{(f)}}{\partial V} = T^{-1} \langle P \rangle, \quad \text{and} \quad (3.10)$$

$$\frac{\partial S^{(f)}}{\partial T} = T^{-2} \langle E \rangle. \quad (3.11)$$

The derivation of (3.10) and (3.11) is very similar to the corresponding formulas for the solid, hence we omit such a derivation.

The harmonic (3.4) and ideal gas (3.8) limits are not always applicable—for instance, there are systems with solid phases being dynamically unstable at low temperature. For such systems, the limit (3.4) is irrelevant. In such cases, we determine the additive constant of the free energy through fitting to the melting (or, more generally, coexistence) point of a phase. We find melting point at pressure P by solving the system of equations

$$\left\{ \begin{array}{l} \frac{\partial S^{(f)}}{\partial V^{(f)}} = \frac{P}{T} + \frac{1}{T} \frac{\partial F_{ref}^{(f)}}{\partial V^{(f)}} \\ \frac{\partial S^{(s)}}{\partial V^{(s)}} = \frac{P}{T} + \frac{1}{T} \frac{\partial F_{ref}^{(s)}}{\partial V^{(s)}} \\ S^{(f)} - S^{(s)} = \frac{F_{ref}^{(f)} - F_{ref}^{(s)}}{T} + \frac{P(V^{(f)} - V^{(s)})}{T}, \end{array} \right. \quad (3.12)$$

with respect to the temperature T and specific volumes of solid and fluid, $V^{(f)}$ and $V^{(s)}$.

Gaussian process regression

The derivatives of the entropy from an NVT molecular dynamics (MD) cannot be obtained without some noise arising from averaging over a finite trajectory. Due to randomness in the initial state or in the thermostat, such a trajectory is random. Thus, the free energy that we reconstruct from the MD data is also random, but hopefully, it has a narrow distribution around the true free energy. The effect of a thermostat—let us consider a Langevin thermostat, for instance—consists of making a large number of small perturbations to the trajectory [29]. Thanks to the central limit theorem, it is hence reasonable to assume that averages over such a trajectory are distributed according to the Gaussian distribution. This assumption brings us to the Gaussian process framework.

In the Gaussian process framework, we assume that the data, and the reconstructed free energy, are distributed according to a multivariate Gaussian distribution. We assume zero mean—any prior information about a nonzero mean is already accounted for in F^{ref} . Further, we assume that the values of the free energy at different points (V_1, T_1) and (V_2, T_2) are correlated with covariance $\text{Cov}(S(V_1, T_1), S(V_2, T_2)) = k((V_1, T_1), (V_2, T_2))$. Such a distribution of functions $S(V, T)$ is called the *Gaussian process* (GP) and k is called *the kernel*. A simple example of the kernel is

$$k((V_1, T_1), (V_1, T_1)) \sim \exp\left(-\frac{(T_1 - T_2)^2}{2\theta_T^2}\right) \exp\left(-\frac{(V_1 - V_2)^2}{2\theta_V^2}\right). \quad (3.13)$$

A property of Gaussian processes that will be very helpful in our application is that any linear functional of the Gaussian process is also Gaussian-distributed. For example, the derivative with respect to volume (as, e.g., in (3.10)) at (V_1, T_1) is correlated with $S(V_2, T_2)$ as given by the following formula:

$$\text{Cov}\left(\frac{\partial S}{\partial V_1}(V_1, T_1), S(V_2, T_2)\right) = \frac{\partial}{\partial V_1} k((V_1, T_1), (V_2, T_2)).$$

This allows us to make predictions based on data. In the most general case, each data point is a linear functional X on S , for example $\langle S|X_1 \rangle = S(V, T)$, $\langle S|X_2 \rangle = \frac{\partial}{\partial V} S(V, T)$, etc. The data are usually given with noise, hence the input data to our Gaussian process are of the form $(X_1, Y_1, \Delta Y_1)$, $(X_2, Y_2, \Delta Y_2)$, \dots , which means that

$\langle S|X_i \rangle$ is measured (e.g., from molecular dynamics) as $Y_i \pm \Delta Y_i$, or to be precise, $\langle S|X_i \rangle$ is distributed according to the normal distribution, \mathcal{N}

$$\langle S|X_i \rangle \sim \mathcal{N}(Y_i, (\Delta Y_i)^2).$$

We denote $\text{Cov}(\langle S|X_1 \rangle, \langle S|X_2 \rangle) = k(X_1, X_2)$ extending the definition for the kernel. We assume that the uncertainties ΔY_i are all statistically independent from each other.

Suppose we want to make a prediction of $Y_* = \langle S|X_* \rangle$; for simplicity one can think of $Y_* = F(V_*, T_*)$. The Gaussian process framework is a particular case of the Bayesian framework in which the prediction problem is formulated as the following question: what is the most likely value of Y_* given data X_i, Y_i , and ΔY_i . To that end we form a joint distribution

$$\begin{bmatrix} \mathbf{Y} \\ Y_* \end{bmatrix} \sim \mathcal{N}\left(\begin{pmatrix} \mathbf{0} \\ 0 \end{pmatrix}, \begin{pmatrix} K(\mathbf{X}, \mathbf{X}) + \text{diag}(\Delta \mathbf{Y}) & K(\mathbf{X}, X_*) \\ K(X_*, \mathbf{X}) & K(X_*, X_*) \end{pmatrix}\right),$$

where \mathbf{X} , \mathbf{Y} , and $\Delta \mathbf{Y}^1$ are the vectors composed of X_i, Y_i , and ΔY_i , which makes $K(\mathbf{X}, \mathbf{X})$ a matrix composed of $k(X_i, X_j)$. From this, we find that Y_* is normally-distributed with mean

$$\bar{Y}_* = K(X_*, \mathbf{X})[K(\mathbf{X}, \mathbf{X}) + \text{diag}(\Delta \mathbf{Y})]^{-1} \mathbf{Y},$$

and variance

$$\text{Var}(Y_*) = K(X_*, X_*) - K(X_*, \mathbf{X})[K(\mathbf{X}, \mathbf{X}) + \text{diag}(\Delta \mathbf{Y})]^{-1} K(\mathbf{X}, X_*). \quad (3.14)$$

The variance of a nonlinear functional $\mathcal{F}(S)$, which is needed to predict the uncertainty of determining the melting point (3.12), is derived in Supplemental in the limit of a large amount of data (in which can we can linearize $\mathcal{F}(S)$ around the mean prediction \bar{S}).

For a given application, one needs to find the right values of hyperparameters $\boldsymbol{\theta} = (\theta_T, \theta_V)$ in (3.13). This is done by maximizing the so-called marginal likelihood $p(\mathbf{Y}|\mathbf{X}, \boldsymbol{\theta})$ which is proportional to the probability that the underlying data is distributed according to the hyperparameters $\boldsymbol{\theta}$. The marginal likelihood is calculated according to the formula

$$\begin{aligned} \log p(\mathbf{Y}|\mathbf{X}, \boldsymbol{\theta}) &= -\frac{1}{2} \mathbf{Y}^T [K(\mathbf{X}, \mathbf{X}) + \text{diag}(\Delta \mathbf{Y})]^{-1} \mathbf{Y} \\ &\quad - \frac{1}{2} \log |K(\mathbf{X}, \mathbf{X}) + \text{diag}(\Delta \mathbf{Y})| - \frac{n}{2} \log(2\pi), \end{aligned} \quad (3.15)$$

¹ $\text{diag}(\Delta \mathbf{Y})$ is an operation of transforming vector to diagonal matrix.

where $|K|$ denotes the determinant of the matrix K and n is the dimension of the model (number of input points).

The Bayesian variance expressed in equations (3.14) and (3.25) does not directly depend on \mathbf{Y} . This allows us to define the quantity

$$\mathcal{H}(Q, X^*) = -\log \frac{\mathbb{V}(Q|\mathbf{X} \cup X^*)}{\mathbb{V}(Q|\mathbf{X})}, \quad (3.16)$$

which expresses an expected improvement of the variance of Q after adding a new point X^* to the dataset \mathbf{X} . We will call (3.16) the information function. By maximizing \mathcal{H} with respect to X^* , we find the point that is best in reducing the variance of the quantity Q . This gives rise to our active sampling algorithm, whose essence is to simply greedily add points with maximum information to the training set, one by one. For simplicity, when deciding which new point to add to the training set, we assume that we would add data with zero variance.

Moment Tensor Potential training

Large-scale molecular dynamics (MD) simulations were performed with the use of Moment Tensor Potentials (MTPs) [30, 31] as implemented in the MLIP software package [27]. A total of four MTPs were fit to quantum mechanical data.

Moment tensor potentials for each element were trained to reproduce both the solid and liquid phases and their lattice dynamics near and across the melt. Training for each followed the procedure described in [27] for calculating the melting point. In the pretraining stage, a level-16 MTP with a cutoff radius of 5 Å and a mindist parameter of 1.4 Å was trained with 20 configurations sampled from *ab initio* molecular dynamics. Next, on-the-fly training was performed using classical molecular dynamics for the solid and liquid phases near the melting point. The temperature and lattice constant grids for the active selection runs for each material are shown in Table 3.1. Configurations selected from this training were processed with low-fidelity DFT to reduce computational cost². The final training set, generated from a subset of these configurations, was run with high-accuracy DFT calculations using VASP [32–34]. Another round of active learning was also performed in this step.

A summary of the fitting procedure parameters is shown in Table 3.1, where N_{conf} is the number of configurations in the training set and ΔE is the mean potential energy difference per atom between the MTP and the *ab initio* model. F_{rel} and S_{rel} are the

²Term "low-fidelity" refers to one k-point DFT calculation. This reduces selection cost by a two orders of magnitudes compare to high accuracy kpoint grid.

Table 3.1: Ranges of parameters used in the active learning process, including temperatures, T (K) and increment, and cubic cell lattice constants, a (Å) and increment used for each material.

Element	phase	T (K); ΔT (K)	a (Å); Δa (Å)
Li	solid	300-450; 50	3.42-3.68; 0.04
Li	liquid	500-650; 50	3.42-3.68; 0.04
Pb	solid	300-700; 100	5.000-5.225; 0.025
Pb	liquid	600-1000; 100	5.000-5.225; 0.025
Ge	solid	700-1100; 100	5.60-5.93; 0.03
Ge	liquid	900-1300; 100	5.60-5.93; 0.03
Si	solid	1200-1500; 100	5.40-5.60; 0.05
Si	liquid	1700-2000; 100	5.40-5.60; 0.05

relative energy and stress difference per atom and are computed using

$$A_{\text{rel}} = \sqrt{\frac{\langle (\Delta A - \overline{\Delta A})^2 \rangle}{\langle (A_{\text{MTP}} - \overline{A_{\text{MTP}}})^2 \rangle}}, \quad (3.17)$$

where ΔA is the difference in force or stress between the *ab initio* model and the moment tensor potential, and $\overline{\Delta A}$ is its mean value.

Thermodynamic Integration using Bayesian learning

Illustrative example: performing integration with a Gaussian process

Before applying Gaussian processes to reconstruct the free energy function from its derivatives, let us consider an illustrative problem of simply reconstructing $f(x) = \sin(x)$ on the interval $[0, \pi]$ from its value $f(x) = 0$ and nine noisy values of $f'(x)$. To that end, we take nine evenly spaced points, $x_1 = 0$, $x_2 = \pi/8$, \dots , $x_9 = \pi$ and consider $y_i = f'(x_i) + \mathcal{N}(0, \sigma^2)$ (i.e., added to $f'(x_i)$ some normally distributed noise) with variance $\sigma = 0.1$. The added noise simulates the statistical noise always present in averages taken over finite MD trajectories.

The results of the comparison are shown in Figure 3.2. To mimic thermodynamic integration, the state-of-the-art method used for calculating the free energy, we use the second-order trapezoidal quadrature rule, shown with red in the figure. The “integration” with the Gaussian process was done as outlined in Section 3.1. We see that the accuracy of the two methods is comparable, but the Gaussian process yields smoother results and also gives an accurate confidence interval.

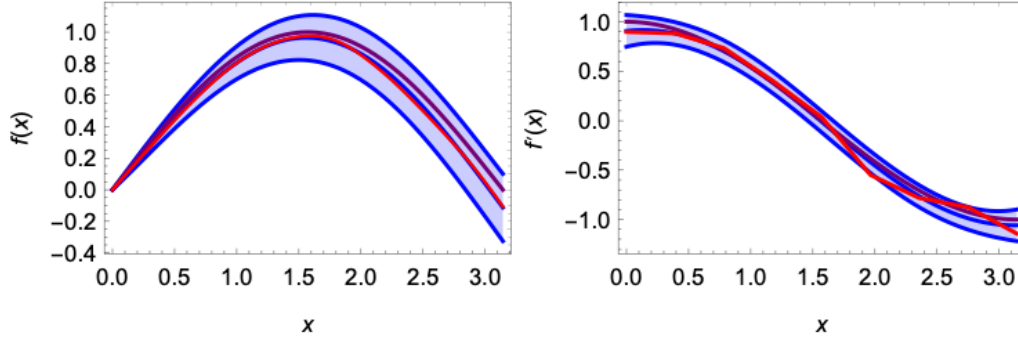


Figure 3.2: Illustration of integration via the trapezoidal quadrature rule (red) and Gaussian process (blue) on noisy data. The left graph shows how the function $f(x) = \sin(x)$ is reconstructed and the right one shows how the derivative is reconstructed. The Gaussian process has the same accuracy, but produces a smooth result and also yields uncertainties of prediction within which the exact solution (purple) falls.

Dataset generation

Thermodynamic data were generated from molecular dynamics calculations using LAMMPS [35] with Moment Tensor Potentials (see section above for how to generate these). Simulations of 4800 ps were run on a grid of volumes and temperatures near the melting point for each element in its solid and liquid phase. The average of the pressure and potential energy of each grid point was taken over 480 values (one value per 10 ps of the calculation) to ensure the statistical independence of the samples. Each simulation was performed with a randomly chosen number of atoms to include information about the finite size dependence of the computed thermodynamic data. The melting point for each element was predicted from a coexistence calculation following the procedure in [36] for uncertainty estimation. The confidence interval for the computational values of the melting point presented in the main text is less than 2 K for all elements.

A Bayesian learning Thermodynamic Integration workflow (Fig. 3.3) was constructed using the thermodynamic data from MD on a temperature-pressure grid (Fig. 3.4). Data generated from this step were fed into a Gaussian Process regression with a physically informed kernel function. The kernel for the solid phases dynamically stable (subscript ss) at low temperatures is chosen as

$$k_{\text{Li}}^{\text{ss}}(x_1, x_2) \sim \exp\left(-\frac{(T_1 - T_2)^2}{2\theta_T^2}\right) \exp\left(-\frac{(\rho_1 - \rho_2)^2}{2\theta_\rho^2}\right) \exp\left(-\left(\frac{1}{N_1} - \frac{1}{N_2}\right)^2 \frac{\theta_N^2}{2}\right).$$

For liquid (subscript liq) and solid phases dynamically unstable at low temperatures (subscript uc) we do not have reference at zero temperature. In order to account

for divergence of entropy at this limit we modify temperature part of the kernel by adding the $\frac{1}{T}$ term:

$$k_{\text{Li}}^{\text{su,liq}}(x_1, x_2) \sim \left(\frac{\theta_T^2}{T_1 T_2} + \exp\left(-\frac{(T_1 - T_2)^2}{2\theta_T'^2}\right) \right) \exp\left(-\frac{(\rho_1 - \rho_2)^2}{2\theta_\rho^2}\right) \exp\left(-\left(\frac{1}{N_1} - \frac{1}{N_2}\right)^2 \frac{\theta_N^2}{2}\right).$$

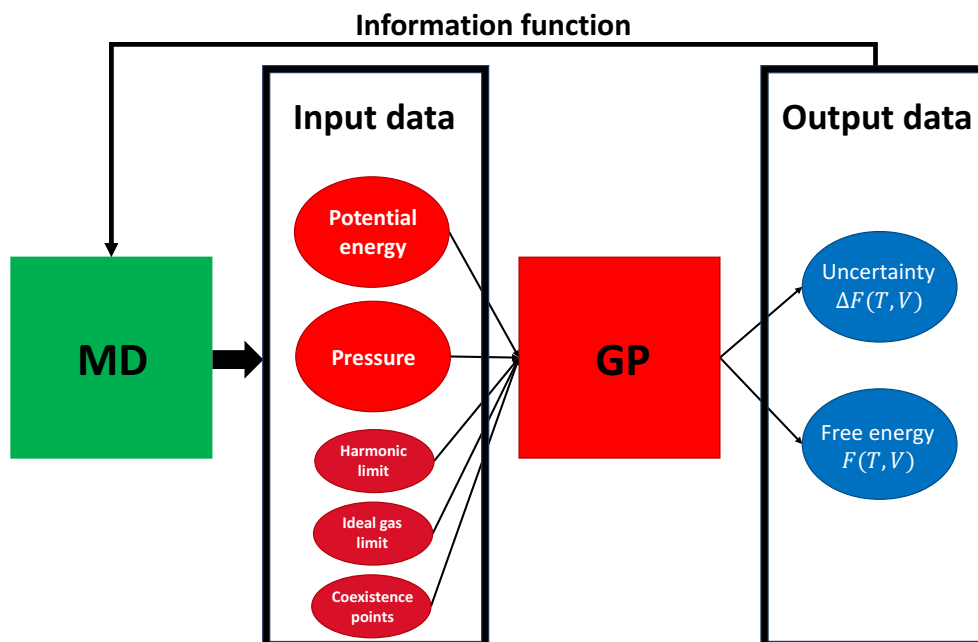


Figure 3.3: General scheme of the Bayesian framework for calculating free energy as a function of volume and temperature.

This process provided a flexible, nonparametric, analytical, functional form, which allowed a reconstruction of the free energy and its derivatives with an estimation of the confidence interval. The resulting statistical error of the computed entropy differences was less than 0.1 %.

Autocorrelation function analyses

The Moment Tensor Potentials obtained with the procedure described in the previous section were used to perform large-scale molecular dynamics simulations with the LAMMPS code [35]. The supercell size was $20 \times 20 \times 20$ of the conventional unit cell of the corresponding solid phase. The calculations were performed in two subsequent steps. In the first step, the system was equilibrated near melting. For the solid phase, this corresponded to a molecular dynamics run at zero pressure at the

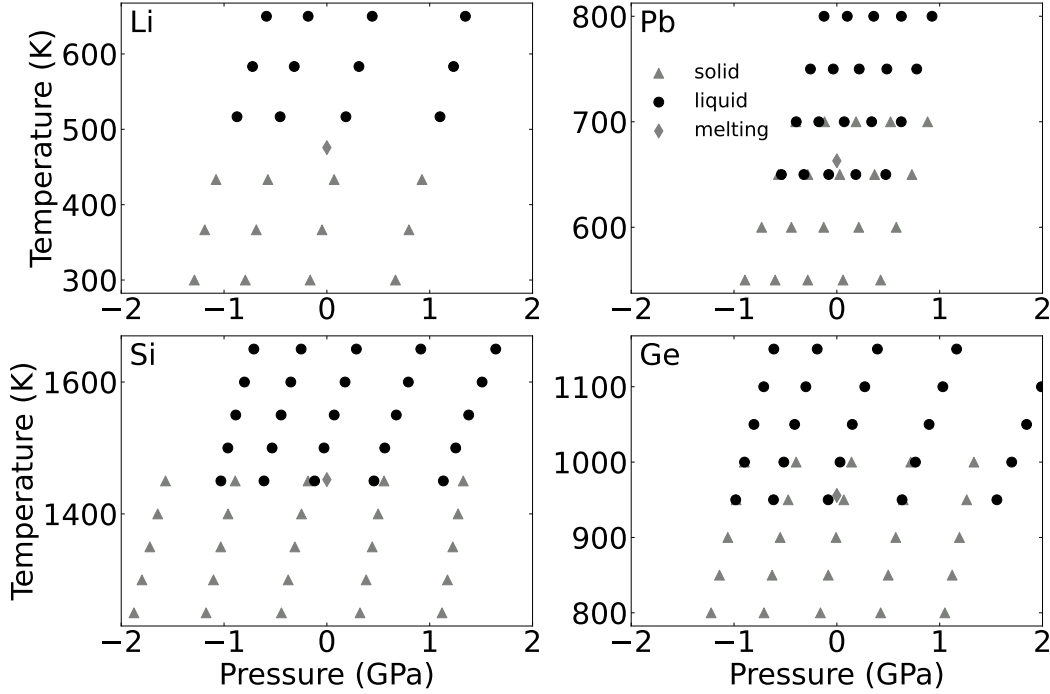


Figure 3.4: Thermodynamic data for free energy integration from Molecular Dynamics simulation of Li, Pb, Si, and Ge in the crystalline solid (gray triangles), liquid (black circles), and melting point (grey diamonds).

melting temperature for 40 ps. The procedure for liquids included an additional pre-equilibrium melting stage in which the system was kept at a high temperature (four times the melting temperature) for 40 ps. In the second step, the equilibrated phases were run in the microcanonical (NVE) ensemble for 10 ps. The autocorrelation function was then computed using outputs from this step.

The Fourier transform of the autocorrelation function was used to obtain the anharmonic vibrational density of states. For the liquid phase, the contributions from diffusive processes were removed by subtracting a Lorentzian fit from the density of states. The computational densities of states for different elements are shown in Fig. 3.5. Finally, the vibrational contribution to the entropy was calculated from both phases using Eqn. 3.18.

$$S_{\text{vib}} = 3k_B \int g(\varepsilon) [(n(\varepsilon) + 1) \ln(n(\varepsilon) + 1) - n(\varepsilon) \ln(n(\varepsilon))] d\varepsilon. \quad (3.18)$$

3.2 Inelastic Neutron Scattering

Inelastic neutron scattering experiments were performed on high-purity polycrystalline granules of Ge (99.999%), Bi (99.997%), Sn (99.99%), and Pb (99.99%)

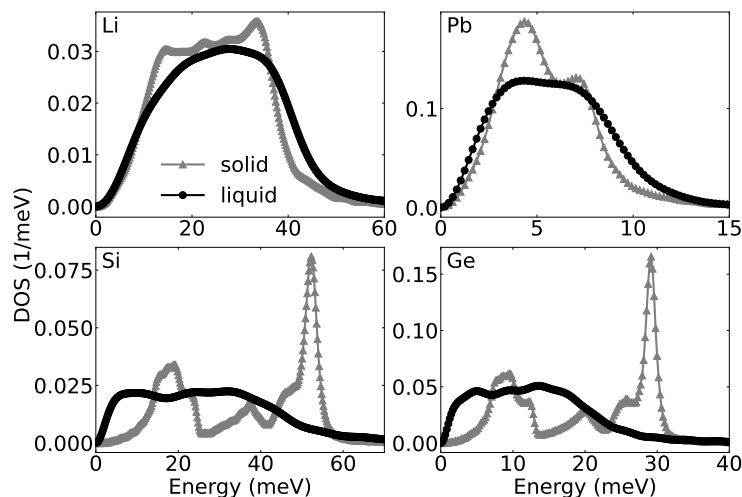


Figure 3.5: Vibrational DOS curves from velocity autocorrelations of Li, Pb, Si, and Ge in the crystalline solid (gray triangles) and liquid (black circles) from computations. Note the large softening in liquid Ge and the small stiffening in Li and Pb. All DOSs are normalized to one.

encapsulated in vacuum-sealed quartz tubes. The high-temperature furnace MICAS was used to heat the samples to approximately 200 K above their melting temperatures, allowing data collection in the solid and liquid phases [37]. Spectra from empty ampules in a vanadium sachet were also collected for background subtraction at the temperatures of interest for background subtraction.

All measurements were taken on the time-of-flight direct geometry wide-angular range chopper spectrometer (ARCS) at the Spallation Neutron Source (SNS) at Oak Ridge National Laboratory [38]. Single phonon scattering and vibrational densities of states (DOS) for the crystalline solids were obtained using the Mantid and multiphonon packages, and multiple scattering corrections were calculated with MCViNE [39–41].

Liquid Spectra Analyses

Accessing a sufficient range of momentum transfer, Q , to capture the structure and dynamics in liquids using time-of-flight (TOF) neutron scattering presents a challenge due to the balance between energy resolution and the kinematic energy cutoff in reciprocal space. An incident energy of 50 meV provided sufficient energy resolution (approximately 2 meV at the elastic peak) and allowed Q -cuts from 0.5–8 \AA^{-1} . An advantage of the TOF method is that it allows simultaneous data acquisition with high statistical quality over a wide range of Q , and the selection of Q for analysis can be done post-measurement.

After subtracting the signal from the empty sample holder, the scattering intensities were separated into diffusive and vibrational components. These intensities were symmetrized using the condition of detailed balance and normalized to the total intensity of the static structure factor, $S(Q)$ yielding $S(Q_n, \varepsilon)/S(Q)$, where Q_n is a selected value of Q and ε is the energy. The quasielastic peak for each Q_n was then fit to the well-established incoherent response function,

$$S(Q, \varepsilon) = \frac{A}{\pi} \frac{\hbar\Gamma(Q)}{\varepsilon^2 + (\hbar\Gamma(Q))^2} * R(Q, \varepsilon), \quad (3.19)$$

where A is a scaling factor, Γ is the peak width, and $*R(Q, \varepsilon)$ denotes a convolution with the resolution function. Within the hydrodynamic regime (where $Q < Q_0/2$ and Q_0 is the location of the first peak in $S(Q)$ [42]), these fits agree with previously reported self-diffusion coefficients, D , from the relationship $\Gamma = DQ^2$ [43–46].

Each fit was then subtracted from the observed intensity to remove effects from diffusion (diffusive processes do not describe atomic vibrations [47], and, as discussed later, diffusion does not contribute substantially to the latent heat).

To analyze the range of Q -cuts with distinct vibrational dynamics, a $S(Q_n, \varepsilon)$ specific density of states (DOS) algorithm was developed. DOS curves from individual Q_n for the liquid were summed and normalized to obtain a total vibrational density of states, $g(\varepsilon)$. This workflow was repeated on the solid for the same Q_n .

3.3 Results and Discussion

Vibrational Densities of States

The left columns of Figure 3.6 (a), (b) show background-corrected inelastic neutron scattering spectra for polycrystalline and liquid Ge and Pb near their melting temperatures, $T_{m,Ge} = 1211$ K and $T_{m,Pb} = 601$ K. Intensities for each element are on the same scale so a direct comparison of features between the solid and liquid phases is possible. Selected constant- Q slices for liquid Ge and Pb are shown in the right column of Fig 3.6 (a), (b). Gray error bars show the excellent statistical quality of the data — the error bars are often smaller than the marker size. Dashed lines illustrate the resolution-convoluted quasielastic fits of Eqn. 3.19. Each matches well the expected Lorentzian shape and intensities [44, 48–50].

In agreement with previous studies [51–53], Fig. 3.6 shows non-diffusive contributions to the scattering intensities. Similar intensities are also found for Bi and Sn. After corrections to remove intensities from quasielastic, multiple scattering (MS), and multiphonon (MP) scattering, the vibrational spectra remain. These are used to

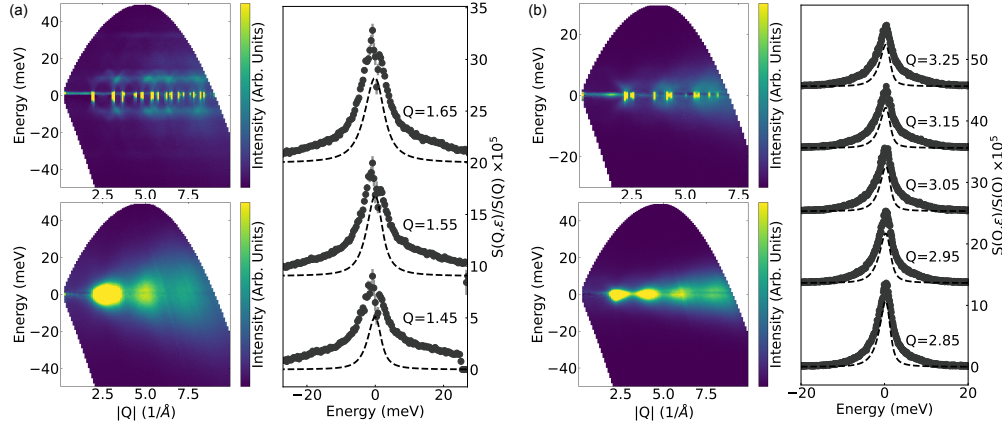


Figure 3.6: Inelastic neutron scattering spectra for solid and liquid Ge and Pb. Total $S(Q, \varepsilon)$ in the crystalline solid (top left) and liquid (bottom left) phases after background subtraction, with selected $S(Q_n, \varepsilon)$ (right) normalized to $S(Q)$ for (a) Ge and (b) Pb near their respective melting temperatures. The $S(Q, \varepsilon)$ intensity bars for the solid and liquid phases of each element are the same and are on a log scale. The dashed lines under the constant Q cuts are quasielastic fits to the data that include a convolution with the Q and ε -dependent instrument resolution function. Standard errors (grey bars) are generally smaller than the symbol size.

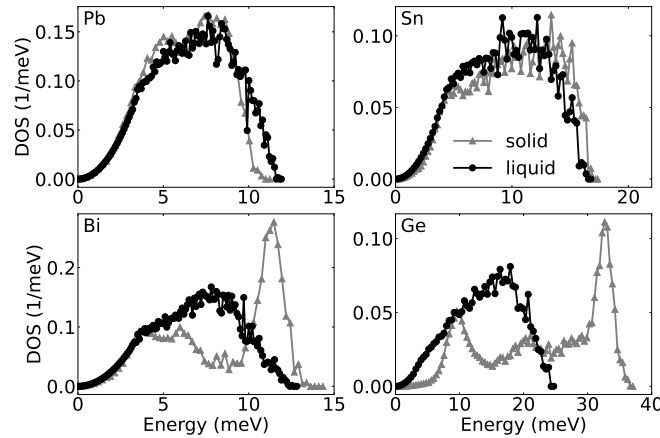


Figure 3.7: Experimental DOS curves. Each DOS curve is from Q -cuts of Pb, Sn, Bi, and Ge in the crystalline solid (gray triangles) and liquid (black circles) phases. Note the large softening in liquid Ge and the small stiffening in Pb. All DOSs are normalized to one.

obtain the Q -weighted densities of states (DOSs) in Fig. 3.7 for Pb, Sn, Bi, and Ge. Crystalline solid DOSs obtained from the same Q values are plotted for comparison.

The upper vibrational modes in liquid Pb extend to energies higher than those of solid Pb, showing a stiffening from approximately 10 to 12 meV. This is unexpected since most materials exhibit the opposite behavior with increasing temperature. Results

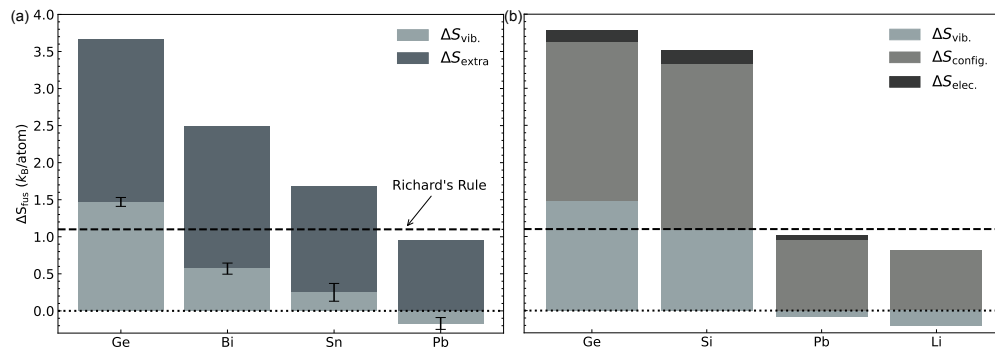


Figure 3.8: Atomistic components of the entropy of fusion from inelastic neutron scattering and molecular dynamics. (a) Vibrational (light gray), and extra (dark gray) contributions to the entropies of fusion in Ge, Bi, Sn, and Pb determined from Q -weighted densities of states. Error bars were estimated from the two scalings of the neutron-weighted density of states (see details in Methods: Density of States Analysis). (b) Vibrational (light gray), configurational (dark gray), and electronic (black) contributions to the entropies of fusion in Ge, Si, Pb, and Li from computations. The horizontal dashed line is the total entropy of fusion, $\Delta S_{\text{fus}} = 1.1 k_B$ per atom, according to Richard's rule.

for Sn are more typical, showing a small softening of the vibrational spectrum upon melting. Nevertheless, the average energies of both solid and liquid DOS curves for Pb and Sn are similar. The elements Bi and Ge, which show large deviations from Richard's rule, exhibit significant differences between their vibrational DOSs for crystalline and liquid phases. The highest vibrational peak in Bi softens from 11.4 to 8 meV. Ge shows an even greater decrease in energy between its solid and liquid states (32.8 to 17.2 meV). Computed DOSs (Fig. 3.5) corroborate these results.

Figure 3.8(a) shows the vibrational contributions to the entropy of fusion of Ge, Bi, Sn, and Pb from the inelastic neutron scattering measurements. The difference between the total and vibrational entropies of fusion, denoted ΔS_{extra} , for each element is also shown. Computational results for Ge, Si, Pb, and Li are presented in Fig. 3.8(b). For Ge and Pb, there is excellent agreement between the vibrational entropies from simulations and experiments (see Table 3.2). The dashed horizontal line in Fig. 3.8 depicts the total entropy according to Richard's rule.

Richard's Rule and Anomalous Melting

Figure 3.1 shows numerous deviations from Richard's rule, with values of ΔS_{fus} that span an order of magnitude. A step beyond Richard's rule has been to classify melting as normal or anomalous based on whether materials follow or deviate from $\Delta S_{\text{fus}} = 1.1 k_B$ per atom. However, Fig. 3.1(b) shows that this binary classification

Table 3.2: Thermodynamic contributions to the entropy of fusion from experimental | computational methods.

Element exp. comp.	ΔS_{fus} (k_B per atom)	$\Delta S_{\text{fus,vib}}$ (k_B per atom)	$\Delta S_{\text{fus,config}}$ (k_B per atom)	$\Delta S_{\text{fus,el}}$ (k_B per atom)
Ge	3.67 3.78	1.47 1.48	2.14	0.16
Si	3.58 3.51	1.09	2.24	0.19
Bi	2.50	0.57		
Sn	1.67	0.25		
Pb	0.95 1.03	-0.17 -0.08	1.03	0.07
Li	0.80 0.81	-0.21	1.02	0.00

lacks nuance.

Figure 3.9 shows a trend for all our results. The best fit line shows that $\Delta S_{\text{fus,vib}}$ is zero for $\Delta S_{\text{fus}} \approx 1.2 k_B$ per atom, which is close to the value used for Richard’s rule. If Richard’s rule were representative of all elements, $\Delta S_{\text{fus}} - 1.2 \approx 0$ (all units in k_B per atom), so deviations can be represented as

$$\Delta S_{\text{fus}} - 1.2 = \delta S_{\text{vib}} + \delta S_{\text{config}}, \quad (3.20)$$

where δ denotes the “extra” entropy. The linear relationship of Fig. 3.9 is

$$\Delta S_{\text{fus}} - 1.2 = 1.8 \delta S_{\text{vib}}. \quad (3.21)$$

Equating Eqns. 3.20 and 3.21, the extra configurational entropy is proportional to the extra vibrational entropy

$$\delta S_{\text{config}} = 0.8 \delta S_{\text{vib}}. \quad (3.22)$$

This proportionality of δS_{config} and δS_{vib} indicates that structural changes which increase the number of accessible configurations also decrease the vibrational frequencies. The balance between configurational and vibrational entropies may affect the atomic structures of liquid alloys, surfaces, and interfaces [54].

3.4 Conclusion

The Bayesian learning thermodynamic integration workflow was used to complement INS experiment in the task of quantifying entropy of melting of elements. The computational methods to model melting required large numbers of atoms and employed classical molecular dynamics with machine-learned interatomic potentials. These potentials were trained with ab initio molecular dynamics calculations on smaller systems. Computational results gave changes in vibrational entropies upon

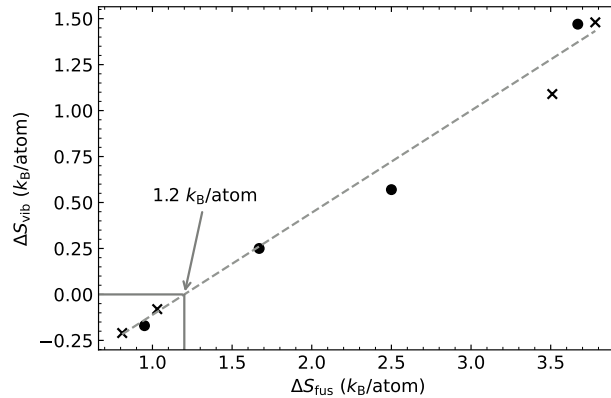


Figure 3.9: Vibrational entropies across the melt versus the total entropy of fusion. Circles (crosses) are from experimental (computational) results. The intercept at $\Delta S_{\text{fus,vib}} = 0$ occurs at $\Delta S_{\text{fus}} \approx 1.2 k_B$ per atom, near the value of Richard’s rule.

melting that were in excellent agreement with the INS results for Ge and Pb and provide results inaccessible in the INS experiment for Li and Si. These simulations also reproduced the total latent heat with good accuracy.

There is an emerging correlation between the latent heat of melting and the difference in vibrational entropies of the solid and liquid phases. To a good approximation, Richard’s rule corresponds to melting with zero change in vibrational entropy, which occurs when $\Delta S_{\text{fus}} \approx 1.2 k_B$ per atom. Deviations from Richard’s rule are proportional to the change in vibrational entropy upon melting. However, these deviations also include an extra ΔS_{config} equal to 80% of ΔS_{vib} .

3.5 Supplemental Materials

Derivation of Free Energy Relations

Reference for Solid

Let us expand the free energy (3.3) around $T = 0$. To that end we split \mathbf{x} into two families of degrees of freedom: x_N and $\tilde{\mathbf{x}} = (x_1, \dots, x_{N-1})$. Let $\beta := T^{-1}$. The determinant of the Jacobian of this transformation is 1 and hence we can write

$$\beta \hat{F}_{\text{ref}}(T) - \hat{S}(T) = -\log \int dx_N \int \exp(-\beta \hat{E}(\tilde{\mathbf{x}}, x_N)) d\tilde{\mathbf{x}}.$$

Because of translational symmetry, we can fix $x_N = 0$ in the inner (second) integral and hence

$$\beta \hat{F}_{\text{ref}}(T) - \hat{S}(T) = -\log \hat{V} - \log \int_{\hat{V}^{N-1}} \exp(-\beta E(\tilde{\mathbf{x}}, 0)) d\tilde{\mathbf{x}}.$$

Now note that for small T , only the energy near the ground state \boldsymbol{x}_0 is relevant. Given a ground state \boldsymbol{x}_0 , it is repeated $(N - 1)!$ times in the integral because of permutation invariance in $E(\tilde{\boldsymbol{x}}, 0)$. Hence

$$\beta \hat{F}_{ref}(T) - \hat{S}(T) = -\log \hat{V} - \log(N - 1)! - \log \int_{\tilde{\boldsymbol{x}} \sim \boldsymbol{x}_0} \exp(-\beta E(\tilde{\boldsymbol{x}}, 0)) d\tilde{\boldsymbol{x}},$$

where the integration is taken specifically around the ground state \boldsymbol{x}_0 . $E(\tilde{\boldsymbol{x}}, 0)$ has a nondegenerate Hessian around the ground state around which we will expand

$$\begin{aligned} \beta \hat{F}_{ref}(T) - \hat{S}(T) &= -\log \hat{V} - \log(N - 1)! + \beta \hat{E}_0 \\ &\quad - \log \int \exp(-\langle \boldsymbol{x} | \tilde{H} | \boldsymbol{x} \rangle / (2T)) d\boldsymbol{x} + O(T), \end{aligned}$$

where \tilde{H} is the Hessian of $E(\tilde{\boldsymbol{x}}, 0)$ at the ground state. Carrying out the integration and calculating yields

$$\begin{aligned} \beta(\hat{F}_{ref}(T) - \hat{E}_0) - \hat{S}(T) &= -\log \hat{V} - \log(N - 1)! \\ &\quad - \log((2\pi T)^{3N-3} / \det \tilde{H})^{1/2} + O(T) \\ &= -\log \hat{V} + \log(N) - \log N! \\ &\quad - \frac{1}{2}(3N - 3) \log(2\pi T) + \frac{1}{2} \log \det \tilde{H} + O(T) \\ &= -\log \hat{V} + \log(N) - N \log N + N - \log(2\pi N) + O(N^{-1}) \\ &\quad - \frac{1}{2}(3N - 3) \log(2\pi T) + \frac{1}{2} \log \det \tilde{H} + O(T) \\ &= N(-\log N + 1 - \frac{3}{2} \log(2\pi T) + \frac{1}{2N} \log \det \tilde{H}) \\ &\quad (-\log \hat{V} + \frac{1}{2} \log(2\pi) + \frac{3}{2} \log(T)) + O(T + N^{-1}). \end{aligned}$$

We can now make the reverse change of variables from $\tilde{\boldsymbol{x}}$ back to \boldsymbol{x} , with $\det \tilde{H} = \det \hat{H}$, where \hat{H} is the $(3N - 3) \times (3N - 3)$ Hessian of \hat{E} computed at the ground state and projected onto the subspace orthogonal to the center of mass $x_c = \frac{1}{N} \sum_i x_i$. And finally, we will use the simplified version of this formula for the intensive quantities

$$\beta(F_{ref}(T) - E_0) - S(T) = -\log N + 1 - \frac{3}{2} \log(2\pi T) + \frac{1}{2N} \log \det \hat{H} + O(T + N^{-1}).$$

Hence for solid, we choose

$$F_{ref}(T) := E_0 + T(-\log(NV) + 1 - \frac{3}{2} \log(2\pi T)),$$

which is the same as (3.4), and then (3.5) follows. We note that we could leave out V from F_{ref} , but then it would enter the expression for $\partial S / \partial V$ and hence create asymmetry with the liquid.

Derivative for Solid

An NVT-thermostatted molecular dynamics used in this work produces the averages

$$\langle f \rangle := \frac{\int f(\mathbf{x}) \exp(-\beta \hat{E}(\mathbf{x})) d\mathbf{x}}{\int \exp(-\beta \hat{E}(\mathbf{x})) d\mathbf{x}}.$$

Here the integral is over \hat{V}^N , and we omit the region of integration when it is clear from the context.

Let us use this formula to find

$$\begin{aligned} \frac{\partial(\beta F_{ref} - S)}{\partial \beta} &= -\frac{\partial}{\partial \beta} \log \int \exp(-\beta E(\mathbf{x})) d\mathbf{x} \\ &= -\left(\int \exp(-\beta E(\mathbf{x})) d\mathbf{x} \right)^{-1} \int (-E(\mathbf{x})) \exp(-\beta E(\mathbf{x})) d\mathbf{x}. \end{aligned}$$

Then we can determine the relation between the mean potential energy and the free energy:

$$\langle E \rangle = \frac{\partial(\beta F_{ref} - S)}{\partial \beta} = -T^2 \frac{\partial(\beta F_{ref} - S)}{\partial T}.$$

Hence

$$\begin{aligned} -\frac{\partial S}{\partial \beta} &= -\frac{\partial(\beta F_{ref})}{\partial \beta} + \langle E \rangle \\ &= -\frac{\partial}{\partial \beta} (\beta E_0 - \log N + 1 - \frac{3}{2} \log(2\pi T)) + \langle E \rangle \\ &= -\frac{\partial}{\partial \beta} (\frac{3}{2} \log(\beta)) + \langle E - E_0 \rangle = \langle E - E_0 \rangle - \frac{3}{2} T, \end{aligned}$$

or

$$\frac{\partial S(T, V)}{\partial T} = T^{-2} \langle E - E_0 \rangle - \frac{3}{2} T^{-1}. \quad (3.23)$$

Let us find a similar expression for the partial derivative with respect to volume V .

$$\begin{aligned} \frac{\partial(\beta F_{ref} - S)}{\partial V} &= -\frac{\partial}{\partial V} \log \int \exp(-\beta E(\mathbf{x})) d\mathbf{x} \\ &= -\left(\int \exp(-\beta E(\mathbf{x})) d\mathbf{x} \right)^{-1} \int \beta \left(-\frac{\partial E(\mathbf{x})}{\partial V} \right) \exp(-\beta E(\mathbf{x})) d\mathbf{x} - 1/V. \end{aligned}$$

Assuming that $-\frac{\partial E(\mathbf{x})}{\partial V} = P(\mathbf{x})$, the formula can be rewritten as

$$\frac{\partial(\beta F_{ref} - S)}{\partial V} = -\left(\int \exp(-\beta E(\mathbf{x})) d\mathbf{x} \right)^{-1} \int \beta P(\mathbf{x}) \exp(-\beta E(\mathbf{x})) d\mathbf{x} - 1/V.$$

From this, we can derive the relation between the mean full pressure (sum of the ideal and virial parts) and free energy

$$\langle P \rangle = -\frac{1}{\beta} \frac{\partial(\beta F_{ref} - S)}{\partial V} - \frac{1}{\beta V}.$$

Hence

$$\begin{aligned} -\frac{\partial S}{\partial V} &= -\frac{\partial(\beta F_{ref})}{\partial V} - \beta \langle P \rangle \\ &= -\frac{\partial}{\partial V} (\beta E_0 - \log(N(V)) + 1 - \frac{3}{2} \log(2\pi T)) - \beta \langle P \rangle - \frac{1}{V} \\ &= \beta(P_0 - \langle P \rangle), \end{aligned}$$

or

$$\frac{\partial S}{\partial V} = \frac{\partial S(T, V)}{\partial V} = T^{-1} \langle P - P_0 \rangle. \quad (3.24)$$

Calculation of the Hessian term

The term $N^{-1} \log \det \hat{H}$ can be calculated by integrating over the crystal Brillouin zone. Hessian is a matrix of second derivatives with respect to displacement.

First, let us define Hessian for the interaction of two atoms. For this system, the Hessian is just a 3×3 matrix calculated as

$$H_{ij} = -\frac{\partial^2 E}{\partial r_i \partial r_j}, \quad i, j \in \{1, 2, 3\}.$$

Here r_i, r_j are the components of the vector \mathbf{r} , and E is the potential energy of the system. The Hessian matrix for a larger system is constructed by adding such 3×3 blocks of two-atom interactions. For simplicity, we will only consider the **fcc** lattice case, which can be easily extended to an arbitrary lattice.

We start by denoting **fcc** the infinite fcc lattice with the point $(0, 0, 0)$ excluded. For a given vector in the k-space \mathbf{k} , cutoff r_{cut} and the per-atom volume V , we define the Fourier transform of the Hessian matrix as

$$\tilde{H}_{ij} = \sum_{\substack{\mathbf{r} \in \text{fcc} \\ |\mathbf{r}| < r_{cut}}} H_{ij}(\mathbf{r}) (1 - \cos(2\pi \mathbf{k} \cdot \mathbf{r})).$$

We also define the auxiliary function

$$\tilde{R}_{ij} = \sum_{\substack{\mathbf{r} \in \text{fcc} \\ |\mathbf{r}| < 1}} (1 - \cos(2\pi \mathbf{k} \cdot \mathbf{r})),$$

which will help us to integrate the singularity at $\mathbf{k} = (0, 0, 0)$.

The vectors \mathbf{k} lie in the Brillouin zone of fcc lattice. The Brillouin zone \mathbf{Br} of fcc lattice is the set of points \mathbf{k} defined as:

$$\mathbf{Br}\{\mathbf{k} : |\mathbf{k}|^2 \leq |\mathbf{k} - \mathbf{x}|^2, \mathbf{x} \in \mathbf{bcc}\}.$$

Finally we express the value of $\log \det \hat{H}$ as follows:

$$\log \det \hat{H} = 2 \left(\int_{0 < k_1, k_2, k_3 < 1, \mathbf{k} \in \mathbf{Br}} \log \det(\tilde{H}/\tilde{R}) \right) + 6 \left(\int_{0 < k_1, k_2, k_3 < 1, \mathbf{k} \in \mathbf{Br}} \log \tilde{R} \right)$$

(note that \tilde{H} is a 3x3 matrix, hence the factor of 6 in the second term).

The material-independent part, $\int_{0 < k_1, k_2, k_3 < 1, \mathbf{k} \in \mathbf{Br}} \log \tilde{R}$ is integrated beforehand with the accuracy of 10^{-15} .

The error of this calculation, for the purpose of feeding it to the Gaussian process regression framework, is as the mean square of accuracy and difference of $\log \det \hat{H}$ values for the nearest cutoffs.

Variance of a nonlinear functional

The melting point, defined as a system of equations (3.12), is a nonlinear functional of Gaussian processes. In this case, we reduce the problem to a linear functional, obtained by expanding the original functional in the Taylor series around the mean of the Gaussian process. We denote the original nonlinear functional as $\mathcal{F} = \mathcal{F}(S)$. Then, the functional is linearized near the solution and the quantity of interest is now approximated with a linear functional, $\mathcal{F}(S) \approx \mathcal{F}(\bar{S}) + \langle S - \bar{S}, J \rangle$, where \bar{S} is the mean predicted entropy, and J is the gradient (Jacobian) of \mathcal{F} evaluated at \bar{S} . We can then evaluate variance, similarly to (3.14)

$$\mathbb{V}[\mathcal{F}] \approx \mathbb{V}[J] = K(J, J) - K(J, \mathbf{X})^T K(\mathbf{X}, \mathbf{X})^{-1} K(J, \mathbf{X}). \quad (3.25)$$

References

- [1] V. Ladygin, I. Beniya, E. Makarov, and A. Shapeev. Bayesian learning of thermodynamic integration and numerical convergence for accurate phase diagrams. *Phys. Rev. B*, 104(10):104102, 2021. doi: <https://doi.org/10.1103/PhysRevB.104.104102>.
- [2] C. M. Bernal-Choban, V. Ladygin, G. Granroth, C. N. Saunders, S. Lohaus, D. L. Abernathy, and B. Fultz. Atomistic origin of the entropy of melting from inelastic neutron scattering and machine learned molecular dynamics. *Comm. Mat.*, 2024. doi: <https://doi.org/10.1038/s43246-024-00695-x>. URL <https://www.nature.com/articles/s43246-024-00695-x>.
- [3] J. R. Morris, C. Z. Wang, K. M. Ho, and C. T. Chan. Melting line of aluminum from simulations of coexisting phases. *Phys. Rev. B*, 49(5):3109–3115, February 1994. doi: 10.1103/PhysRevB.49.3109. URL <https://link.aps.org/doi/10.1103/PhysRevB.49.3109>.
- [4] M. Karthikeyan, Robert C. Glen, and A. Bender. General melting point prediction based on a diverse compound data set and artificial neural networks. *J. Chem. Inf. Model.*, 45(3):581–590, May 2005. ISSN 1549-9596. doi: 10.1021/ci0500132. URL <https://doi.org/10.1021/ci0500132>.
- [5] Q.-J. Hong and A. van de Walle. Solid-liquid coexistence in small systems: A statistical method to calculate melting temperatures. *J. Chem. Phys.*, 139(9):094114, September 2013. ISSN 0021-9606. doi: 10.1063/1.4819792. URL <https://doi.org/10.1063/1.4819792>.
- [6] Q.-J. Hong, S. V. Ushakov, A. van de Walle, and A. Navrotsky. Melting temperature prediction using a graph neural network model: From ancient minerals to new materials. *Proc. Natl. Acad. Sci.*, 119(36):e2209630119, September 2022. doi: 10.1073/pnas.2209630119. URL <https://www.pnas.org/doi/10.1073/pnas.2209630119>.
- [7] F. A. Lindemann. Über die berechnung molekularer eigenfrequenzen. *Phys. Z.*, 11(14):609–612, 1910.
- [8] D. C. Wallace. Melting of elements. *Proc. R. Soc. Lond. Ser. A*, 433(1889):631–661, January 1997. doi: 10.1098/rspa.1991.0068. URL <https://royalsocietypublishing.org/doi/abs/10.1098/rspa.1991.0068>.
- [9] J. Ding, L. Li, N. Wang, L. Tian, M. Asta, R. O. Ritchie, and T. Egami. Universal nature of the saddle states of structural excitations in metallic glasses. *Mater. Today Phys.*, 17:100359, March 2021. ISSN 25425293. doi: 10.1016/j.mtphys.2021.100359. URL <https://linkinghub.elsevier.com/retrieve/pii/S2542529321000201>.

- [10] Q. An, W. L. Johnson, K. Samwer, S. L. Corona, and W. A. Goddard. The first order L-G phase transition in liquid Ag and Ag-Cu alloys is driven by deviatoric strain. *Scr. Mater.*, 194:113695, March 2021. ISSN 13596462. doi: 10.1016/j.scriptamat.2020.113695. URL <https://linkinghub.elsevier.com/retrieve/pii/S1359646220308174>.
- [11] P. Guan and V. Viswanathan. MeltNet: Predicting alloy melting temperature by machine learning. *arXiv preprint arXiv:2010.14048*, October 2020. doi: 10.48550/arXiv.2010.14048. URL <http://arxiv.org/abs/2010.14048>.
- [12] K. K. Bejagam, J. Lalonde, C. N. Iverson, B. L. Marrone, and G. Pilianna. Machine learning for melting temperature predictions and design in polyhydroxyalkanoate-based biopolymers. *J. Phys. Chem. B*, 126(4):934–945, February 2022. ISSN 1520-6106. doi: 10.1021/acs.jpcc.1c08354. URL <https://doi.org/10.1021/acs.jpcc.1c08354>.
- [13] J. H. Jung, P. Srinivasan, A. Forslund, and B. Grabowski. High-accuracy thermodynamic properties to the melting point from ab initio calculations aided by machine-learning potentials. *Npj Comput. Mater.*, 9(1):3, January 2023. ISSN 2057-3960. doi: 10.1038/s41524-022-00956-8. URL <https://www.nature.com/articles/s41524-022-00956-8>.
- [14] B. Fultz. *Phase Transitions in Materials*. Cambridge University Press, Cambridge, 2nd edition, 2020. ISBN 978-1-108-48578-4. doi: 10.1017/9781108641449.
- [15] G. Grimvall. On anomalous entropies of fusion. *Liquid Metals 1976*, pages 90–94, 1977.
- [16] D. C. Wallace. Statistical mechanical theory of liquid entropy. *Int. J. Quantum Chem.*, 52(2):425–435, 1994. ISSN 1097-461X. doi: 10.1002/qua.560520215. URL <http://onlinelibrary.wiley.com/doi/abs/10.1002/qua.560520215>.
- [17] R. K. Schulze, D. C. Wallace, and J. C. Lashley. Density of states features in some anomalous melting elements. *J. Phys.: Condens. Matter*, 25(46):465107, October 2013. ISSN 0953-8984. doi: 10.1088/0953-8984/25/46/465107. URL <https://dx.doi.org/10.1088/0953-8984/25/46/465107>.
- [18] C. K. Das. Anomaly in the behavior of silicon from free energy analysis: A computational study. In V. Suma, X. Fernando, K.-L. Du, and H. Wang, editors, *Evolutionary Computing and Mobile Sustainable Networks*, Lecture Notes on Data Engineering and Communications Technologies, pages 575–592, Singapore, 2022. ISBN 9789811696053. doi: 10.1007/978-981-16-9605-3_39.
- [19] V. F. Sears. Slow-neutron multiple scattering. *Advances in Physics*, 24(1):1–45, January 1975. ISSN 0001-8732, 1460-6976. doi: 10.1080/

00018737500101361. URL <http://www.tandfonline.com/doi/abs/10.1080/00018737500101361>.
- [20] B. N. Brockhouse. Lattice vibrations in silicon and germanium. *Phys. Rev. Lett.*, 2(6):256–258, March 1959. doi: 10.1103/PhysRevLett.2.256. URL <https://link.aps.org/doi/10.1103/PhysRevLett.2.256>.
- [21] S. K. Sinha. Theory of inelastic x-ray scattering from condensed matter. *J. Phys.: Condens. Matter*, 13(34):7511, August 2001. ISSN 0953-8984. doi: 10.1088/0953-8984/13/34/304. URL <https://dx.doi.org/10.1088/0953-8984/13/34/304>.
- [22] T. M. Linker, A. Krishnamoorthy, L. L. Daemen, A. J. Ramirez-Cuesta, K. Nomura, A. Nakano, Y. Q. Cheng, W. R. Hicks, A. I. Kolesnikov, and P. D. Vashishta. Neutron scattering and neural-network quantum molecular dynamics investigation of the vibrations of ammonia along the solid-to-liquid transition. *Nat. Commun.*, 15(1):3911, May 2024. doi: 10.1038/s41467-024-48246-9. URL <https://www.nature.com/articles/s41467-024-48246-9>.
- [23] P. D. Bogdanoff, B. Fultz, J. L. Robertson, and L. Crow. Temperature dependence of the phonon entropy of vanadium. *Phys. Rev. B*, 65(1):014303, December 2001. ISSN 0163-1829, 1095-3795. doi: 10.1103/PhysRevB.65.014303. URL <https://link.aps.org/doi/10.1103/PhysRevB.65.014303>.
- [24] M. Kresch, O. Delaire, R. Stevens, J. Y. Y. Lin, and B. Fultz. Neutron scattering measurements of phonons in nickel at elevated temperatures. *Phys. Rev. B*, 75(10):104301, March 2007. ISSN 1098-0121, 1550-235X. doi: 10.1103/PhysRevB.75.104301. URL <https://link.aps.org/doi/10.1103/PhysRevB.75.104301>.
- [25] H. L. Smith, C. W. Li, A. Hoff, G. R. Garrett, D. S. Kim, F. C. Yang, M. S. Lucas, T. Swan-Wood, J. Y. Y. Lin, M. B. Stone, D. L. Abernathy, M. D. Demetriou, and B. Fultz. Separating the configurational and vibrational entropy contributions in metallic glasses. *Nat. Phys.*, 13(9):900–905, September 2017. ISSN 1745-2481. doi: 10.1038/nphys4142. URL <https://www.nature.com/articles/nphys4142>.
- [26] A. V. Shapeev. Moment tensor potentials: A class of systematically improvable interatomic potentials. *Multiscale Model. Simul.*, 14(3):1153–1173, 2016. doi: 10.1137/15M1054183. URL <https://doi.org/10.1137/15M1054183>.
- [27] I. S. Novikov, K. Gubaev, E. V. Podryabinkin, and A. V. Shapeev. The MLIP package: Moment tensor potentials with MPI and active learning. *Mach. Learn.: Sci. Technol.*, 2(2):025002, 2020.
- [28] J. M. Dickey and A. Paskin. Computer simulation of the lattice dynamics of solids. *Phys. Rev.*, 188(3):1407, 1969.

- [29] M. P. Allen and D. J. Tildesley. *Computer simulation of liquids*. Oxford University Press, 2017.
- [30] A. V. Shapeev. Moment tensor potentials: A class of systematically improvable interatomic potentials. *MMS*, 14(3):1153–1173, 2016.
- [31] Konstantin Gubaev, E. V. Podryabinkin, G. L. W. Hart, and A. V. Shapeev. Accelerating high-throughput searches for new alloys with active learning of interatomic potentials. *Comput. Mater. Sci.*, 156:148–156, 2019.
- [32] G. Kresse and J. Hafner. Ab initio molecular-dynamics simulation of the liquid-metal–amorphous-semiconductor transition in germanium. *Phys. Rev. B*, 49(20):14251–14269, May 1994. doi: 10.1103/PhysRevB.49.14251. URL <https://link.aps.org/doi/10.1103/PhysRevB.49.14251>.
- [33] G. Kresse and J. Furthmüller. Efficient iterative schemes for ab initio total-energy calculations using a plane-wave basis set. *Phys. Rev. B*, 54(16):11169–11186, October 1996. doi: 10.1103/PhysRevB.54.11169. URL <https://link.aps.org/doi/10.1103/PhysRevB.54.11169>.
- [34] P. E. Blöchl. Projector augmented-wave method. *Phys. Rev. B*, 50(24):17953–17979, December 1994. doi: 10.1103/PhysRevB.50.17953. URL <https://link.aps.org/doi/10.1103/PhysRevB.50.17953>.
- [35] A. P. Thompson, H. M. Aktulga, R. Berger, D. S. Bolintineanu, W. M. Brown, P. S. Crozier, P. J. in’t Veld, A. Kohlmeyer, S. G. Moore, T. D. Nguyen, R. Shan, M. J. Stevens, J. Tranchida, C. Trott, and S. J. Plimpton. LAMMPS - a flexible simulation tool for particle-based materials modeling at the atomic, meso, and continuum scales. *Comp. Phys. Comm.*, 271:108171, 2022. doi: 10.1016/j.cpc.2021.108171.
- [36] O. Klimanova, T. Miryashkin, and A. Shapeev. A physics-informed AI method for calculating melting points with uncertainty control and optimal sampling. *arXiv preprint arXiv:2306.13345*, 2023.
- [37] J. L. Niedziela, R. Mills, M. J. Loguillo, H. D. Skorpenske, D. Armitage, H. L. Smith, J. Y. Y. Lin, M. S. Lucas, M. B. Stone, and D. L. Abernathy. Design and operating characteristic of a vacuum furnace for time-of-flight inelastic neutron scattering measurements. *Rev. Sci. Instrum.*, 88(10):105116, October 2017. ISSN 0034-6748, 1089-7623. doi: 10.1063/1.5007089. URL <http://aip.scitation.org/doi/10.1063/1.5007089>.
- [38] D. L. Abernathy, M. B. Stone, M. J. Loguillo, M. S. Lucas, O. Delaire, X. Tang, J. Y. Y. Lin, and B. Fultz. Design and operation of the wide angular-range chopper spectrometer ARCS at the Spallation Neutron Source. *Rev. Sci. Instrum.*, 83(1):015114, January 2012. ISSN 0034-6748. doi: 10.1063/1.3680104. URL <https://aip.scitation.org/doi/10.1063/1.3680104>.

- [39] O. Arnold, J. C. Bilheux, J. M. Borreguero, A. Buts, S. I. Campbell, L. Chapon, M. Doucet, N. Draper, R. Ferraz Leal, M. A. Gigg, V. E. Lynch, A. Markvardsen, D. J. Mikkelsen, R. L. Mikkelsen, R. Miller, K. Palmen, P. Parker, G. Passos, T. G. Perring, P. F. Peterson, S. Ren, M. A. Reuter, A. T. Savici, J. W. Taylor, R. J. Taylor, R. Tolchenov, W. Zhou, and J. Zikovsky. Mantid—Data analysis and visualization package for neutron scattering and μ SR experiments. *Nucl. Instrum. Methods. Phys. Res. A*, 764:156–166, November 2014. ISSN 0168-9002. doi: 10.1016/j.nima.2014.07.029. URL <https://www.sciencedirect.com/science/article/pii/S0168900214008729>.
- [40] F. Akeroyd, S. Ansell, S. Antony, O. Arnold, A. Bekasovs, J. Bilheux, J. Borreguero, K. Brown, A. Buts, S. Campbell, D. Champion, L. Chapon, M. Clarke, S. Cottrell, R. Dalgliesh, D. Dillow, M. Doucet, N. Draper, R. Fowler, M. A. Gigg, G. Granroth, M. Hagen, W. Heller, A. Hillier, S. Howells, S. Jackson, D. Kachere, M. Koennecke, C. Le Bourlot, R. Leal, V. Lynch, P. Manuel, A. Markvardsen, R. McGreevy, D. Mikkelsen, R. Mikkelsen, R. Miller, S. Nagella, T. Nielsen, K. Palmen, P. G. Parker, M. Pascal, G. Passos, T. Perring, P. F. Peterson, F. Pratt, T. Proffen, P. Radaelli, J. Rainey, S. Ren, M. Reuter, L. Sasstry, A. Savici, J. Taylor, R. J. Taylor, M. Thomas, R. Tolchenov, R. Whitley, M. Whitty, S. Williams, W. Zhou, and J. Zikovsky. Mantid: Manipulation and analysis toolkit for instrument data. 10.5286/SOFTWARE/MANTID, 2013. URL <https://doi.org/10.5286/SOFTWARE/MANTID>.
- [41] J. Y. Y. Lin, H. L. Smith, G. E. Granroth, D. L. Abernathy, M. D. Lumsden, B. Winn, A. A. Aczel, M. Aivazis, and B. Fultz. MCViNE – An object oriented Monte Carlo neutron ray tracing simulation package. *Nucl. Instrum. Methods. Phys. Res. A*, 810(C):86 – 99, 02 2016. doi: 10.1016/j.nima.2015.11.118.
- [42] A. Boothroyd. *Principles of neutron scattering from condensed matter*. Oxford University Press, Oxford, 2020. ISBN 978-0-19-886231-4.
- [43] S. M. Chathoth, B. Damaschke, T. Unruh, and K. Samwer. Influence of structural changes on diffusion in liquid germanium. *Appl. Phys. Lett.*, 94 (22):221906, June 2009. ISSN 0003-6951. doi: 10.1063/1.3139753. URL <http://aip-scitation-org/doi/full/10.1063/1.3139753>.
- [44] Andreas Meyer. The measurement of self-diffusion coefficients in liquid metals with quasielastic neutron scattering. *EPJ Web Conf.*, 83:01002, 2015. ISSN 2100-014X. doi: 10.1051/epjconf/20158301002.
- [45] U. Balucani and M. Zoppi. *Dynamics of the liquid state*. Clarendon Press, 1994. ISBN 0-19-851739-4 978-0-19-851739-9.
- [46] B. N. Brockhouse and N. K. Pope. Time-dependent pair correlations in liquid lead. *Phys. Rev. Lett.*, 3(6):259–262, September 1959. doi: 10.1103/PhysRevLett.3.259. URL <https://link.aps.org/doi/10.1103/PhysRevLett.3.259>.

- [47] J.-P. Hansen and I. R. McDonald. *Theory of simple liquids: With applications of soft matter*. Elsevier/AP, Amstersdam, 4th edition, 2013. ISBN 978-0-12-387032-2.
- [48] T. Schneider, R. Brout, H. Thomas, and J. Feder. Dynamics of the liquid-solid transition. *Phys. Rev. Lett.*, 25(20):1423–1426, November 1970. doi: 10.1103/PhysRevLett.25.1423.
- [49] L. Bosio, E. Schedler, and C. G. Windsor. Quasi-elastic neutron scattering from liquid gallium over the temperature range 163 to 333 K. *J. Phys.*, 37(6): 747–753, 1976. doi: 10.1051/jphys:01976003706074700.
- [50] T. Springer. *Quasielastic neutron scattering for the investigation of diffuse motions in solids and liquids*. Number 64 in Springer tracts in modern physics. Springer, Berlin, 1992. ISBN 978-3-540-05808-3 978-0-387-05808-5.
- [51] J. R. D. Copley and S. W. Lovesey. The dynamic properties of monatomic liquids. *Rep. Prog. Phys.*, 38(4):461–563, April 1975. ISSN 0034-4885. doi: 10.1088/0034-4885/38/4/001. URL <https://doi.org/10.1088/0034-4885/38/4/001>.
- [52] O. Soderstrom, J. R. D. Copley, J.-B. Suck, and B. Dorner. Collective excitations in liquid lead. *J. Phys. F: Met. Phys.*, 10(6):L151, June 1980. ISSN 0305-4608. doi: 10.1088/0305-4608/10/6/001. URL <https://dx.doi.org/10.1088/0305-4608/10/6/001>.
- [53] V. Hugouvieux. *A complete simulation of neutron scattering experiments: From model systems to liquid germanium*. Theses, Université Montpellier II - Sciences et Techniques du Languedoc, November 2004.
- [54] K. Kalantar-Zadeh, T. Daeneke, and J. Tang. The atomic intelligence of liquid metals. *Science*, 385(6707):372–373, 2024. doi: 10.1126/science.adn5871. URL <https://www.science.org/doi/abs/10.1126/science.adn5871>.

Chapter 4

DIFFUSE INTENSITY FROM PHONON NOISE IN INELASTIC NEUTRON SCATTERING IN CUPRITE

Adapted from "Diffuse Intensity from Phonon Noise in Inelastic Neutron Scattering" [1].

4.1 Introduction

There are historical and conceptual parallels between INS and elastic scattering measurements of structures of materials by coherent diffraction. The centers and intensities of sharp diffraction peaks have long been used to solve the structures of crystals. Crystals with smaller coherence lengths r show a broadening of diffraction peaks in wavevector, Q , similar to the broadening of phonon peaks in energy, E , from short lifetimes in t . Today, methods that Fourier transform the diffraction data over a wide range of wavevectors \vec{Q} give real-space pair distribution functions (PDFs) of atom positions in \vec{r} . These PDFs show short-range atomic structures not available from sharp peaks from Bragg diffraction [2]. In particular, between and beneath the Bragg peaks is a diffuse elastic scattering that originates from localized disorder in atom positions, as from static displacement disorder or thermal vibrations. Diffuse elastic scattering originates with randomness in the phase of waves scattered from displaced atoms. This differs conceptually from the broadening of Bragg peaks from small crystal sizes, and the two processes are independent — diffuse scattering occurs in large crystals at high temperatures, which also show a Debye-Waller attenuation of their sharp Bragg diffractions [2–5].

The concept of diffuse elastic scattering from displacements in r has an analog in diffuse inelastic scattering in E from randomness in atom movements in t , and this is the subject of the present chapter. For an oscillation in a pure harmonic potential, the phase increases linearly with time as ωt , where ω is angular frequency. The harmonic oscillator follows the circle in phase space with equal phase angles in equal times shown in Fig. 4.1a (with axes scaled suitably in momentum p and position q). The phase advances nonlinearly with time if non-harmonic forces occur in a part of the vibrational cycle. The extreme case of an oscillation in a hard-wall potential is shown in Fig. 4.1a. With hard walls set at a distance of $\pi/2$ from the maximum displacement of a harmonic oscillator having the same p_{\max} , the oscillation period is

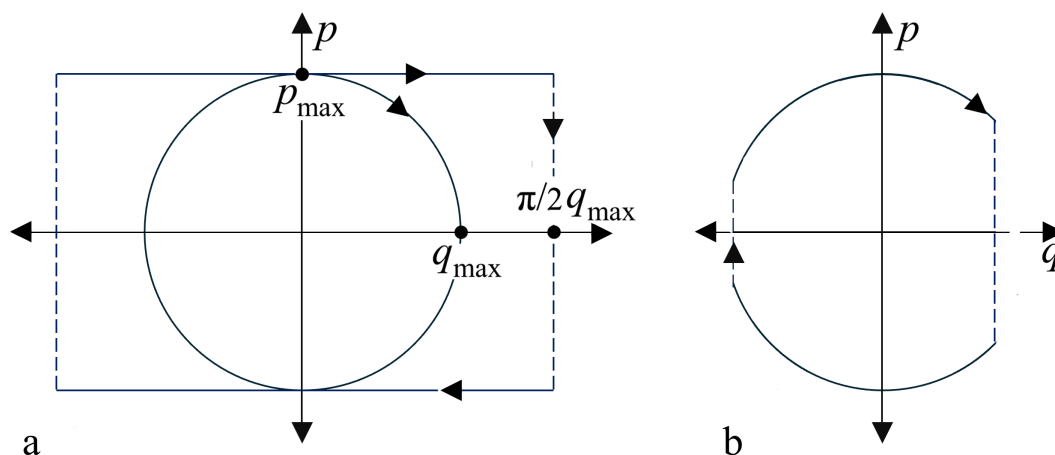


Figure 4.1: Examples of nonlinearities in phase space of an oscillator. (a) Trajectory in p - q (momentum-position) phase space of harmonic oscillator and hard-wall oscillator (rectangle with instant reversal at walls). Both have the same velocity at $q = 0$ and have the same period. (b) Example of phase space for an oscillation with a potential that is harmonic at small q but with moveable hard walls at larger q .

the same as the harmonic oscillator. When the oscillator hits the hard wall, there is a sudden advance of phase of 1.13 radians as its momentum is reversed abruptly. This is depicted as an instantaneous process with the vertical dashed lines. A similarly abrupt advance in phase occurs for the oscillator shown in Fig. 4.1b with a potential that is harmonic at low displacements but has hard walls at higher displacements. These hard walls would have variations in their positions if they originated from neighboring atoms that are themselves moving.

If the potential becomes stiffer as the displacement goes out of the range of harmonic behavior, the phase advances more rapidly with time. This could occur if a vibrating atom interacts with neighboring atoms that behave as stiff spheres. If these interactions were to occur consistently at the same phase in the oscillation cycle, there would be little to distinguish the dynamics measured by inelastic scattering other than a change in frequency. However, randomness in the timings or magnitudes of these phase shifts will give a random component to the phase of inelastic scattering. This analog to phase errors from displacement disorder in atom positions will generate diffuse inelastic scattering (DII) with a broad spread in energy.

Here, my colleagues and I report observations of DII in INS measurements of phonon spectra of cuprite, Cu_2O . In a recent study on phonons and anomalous thermal expansion of cuprite, [6], experimental data showed a substantial broadening of the energies of optical modes at 300 K, along with the appearance of some diffuse

intensity in the inelastic spectrum. At the temperatures of 700 K and 900 K reported here, the optical modes are barely visible as distinct peaks, and DII replaces their spectral intensity at high energies. The simple interpretation of DII is a vibrational mode coupled to a stochastic noise source, modeled with the Schrödinger–Langevin equation. The model includes a damping of the oscillating atom with a coupling to a source of noise. A more realistic analysis with a distribution of phase shifts from interatomic interactions provides a better correspondence with experiment. Molecular dynamics (MD) simulations on cuprite under comparable conditions reproduce some of the DII. The MD simulations provide the DII more reliably when the interatomic potentials are augmented with a more repulsive core. The spectral width of the DII can be used to obtain the time duration of anharmonic interactions between Cu and O-atoms, which is approximately 10 fs, considerably shorter than the coherence time for damping of the phonon modes.

4.2 Experimental Measurements and Ab Initio Simulation

INS measurements

The INS measurements were performed with the time-of-flight wide angular-range chopper spectrometer, ARCS [7], at the Spallation Neutron Source [8]. Phonon dispersions at 10 K and 300 K from the same single crystal were presented previously in Ref. [6]. The data from 700 K and 900 K are presented here for the first time.

Raw data were acquired as time-stamped detections of individual neutrons into pixels of the large-area (π sr) detector array. We used the software Mantid to reduce the single crystal data to the four-dimensional $S(\vec{Q}, \varepsilon)$ [9]. An additional analysis assessed the data statistics, alignment, nonlinearities, and possible abnormalities in the different Brillouin zones. We found no problems, so we folded data throughout \vec{Q} into an irreducible wedge in the first Brillouin zone using symmetry operators. Before folding each zone, we subtracted the multiphonon scattering calculated in the incoherent approximation.

After folding, we thermally weighted the spectral intensities for better visualization of the high energy modes using the factor:

$$\varepsilon \left[1 - \exp\left(\frac{-\varepsilon}{k_B T}\right) \right] \times S(\vec{Q}, \varepsilon) = S_{\text{weighted}}(\vec{Q}, \varepsilon) \quad (4.1)$$

where $\varepsilon = \hbar\omega$. More explanation of this data processing appears in the Supplemental of our prior publication on cuprite [6].

Ab initio and molecular dynamics simulations

Anharmonic vibrational dynamics were first calculated with the method used in our previous work at lower temperatures [6]. Here, a stochastic temperature-dependent effective potential (sTDEP) [10–15] was used to fit an ensemble average of the Hellman-Feynman forces in an *ab initio* simulation of supercells with thermally-displaced atoms. The model potential accounts explicitly for cubic anharmonicity and includes the effects of quartic anharmonicity through renormalizing the harmonic potential. The Supplemental and Ref. [13] explain how the real and imaginary parts of the cubic self-energy correction modify the phonon spectra, following many-body perturbation theory [16, 17]. Results in the Supplemental show that sTDEP account for some, but not all, of the DII in the experimental data of Fig. 5.1.

The DII is most prominent at high temperatures, so classical molecular dynamics (MD) was used for a second, independent, computational effort. We obtained the spectral intensity through the Fourier transform of a velocity-velocity autocorrelation function, projected onto \vec{Q} . These MD calculations required long lengths and extended times for good resolution of phonon features in \vec{Q} and ω [18]. These simulations were performed with a machine learning interatomic potential (MLIP), trained with input from density functional theory (DFT) calculations performed on supercells with VASP [19–22]. The DFT calculations used plane-wave basis sets, the projector augmented wave (PAW) method, exchange-correlation functionals in the generalized gradient approximation (GGA) [23, 24], and supercells generated with thermally-displaced atoms. These training supercells were $3 \times 3 \times 3$, containing 162 atoms. The k -grid was $2 \times 2 \times 2$, and the kinetic energy cutoff was 520 eV. There were 523 supercells in the training set.

Machine-learned moment-tensor potentials [25] were used to model the interatomic interaction in classical MD simulations with the LAMMPS code [26]. The supercell size was $30 \times 30 \times 30$ with 162,000 atoms. The projected velocity-velocity autocorrelation functions came from 20 statistically independent cuts of 80 ps MD trajectories to ensure convergence in the time domain. The results from MD calculations were post-processed in the package VVCORE [27]. The Supplemental provides additional details on MLIP construction, calculations with the temperature-dependent effective potential, other interatomic potentials, and computational data analyses.

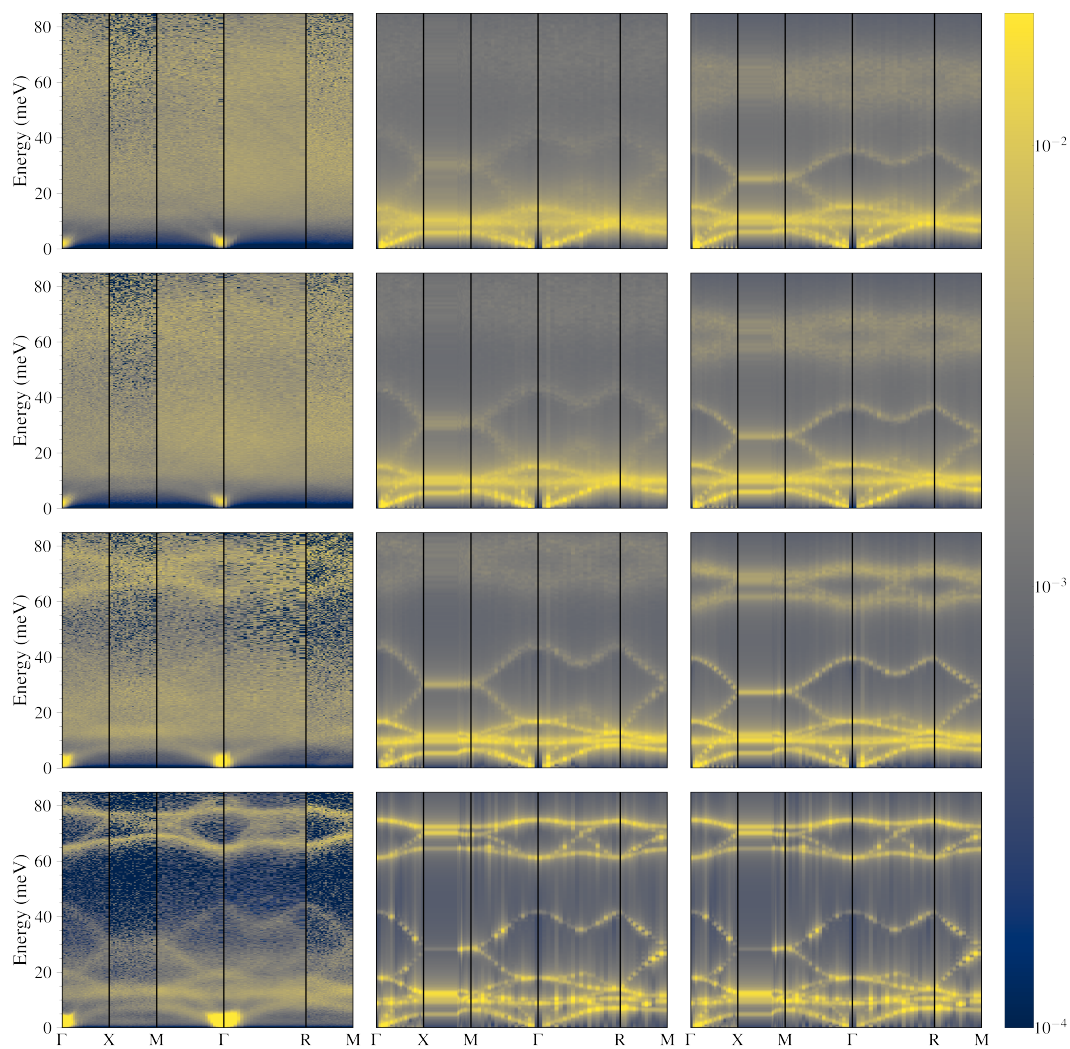


Figure 4.2: Experimental and computational vibrational spectra projected onto high-symmetry directions. Columns from left to right: INS data, MD MLIP with Cu-O bound splined to ZBL potential at low separations; and MD MLIP without ZBL potential. Rows from top to bottom: 900 K, 700 K, 300 K, 10 K. Each panel is normalized with respect to its total inelastic intensity (data are on log scale at right).

4.3 Results and Discussion

INS measurements and simulations

The first column of Fig. 4.2 shows experimental phonon dispersions along some high-symmetry crystallographic directions after folding to include the usable Brillouin zones in the data sets. The lower-energy acoustic dispersions are qualitatively similar at all temperatures. At higher temperatures, the dispersions show obvious changes at energies above 20 meV. Even at 300 K, there is broadening of the highest optical branches, but at 900 K, only a diffuse, featureless band of inelastic intensity is seen at energies above 20 meV. This DII is not a deficiency of data processing; the acoustic dispersions were analyzed simultaneously and retained much of their structure at high temperatures. (The exposure to high temperature did not alter the sample, either. The 10 K data were acquired last.) The DII shows little variation of intensity with \vec{Q} , consistent with inelastic scattering from a system with poor phase coherence.

The right column of Fig. 4.2 shows results from MD simulations with micro-canonical ensembles after thermal equilibration. The middle column of Fig. 4.2 shows results from MD simulations with MTP potential splined to Ziegler-Biersack-Littmark (ZBL [28]) potential for short distances between copper and oxygen atoms. The ZBL part of the potential serves as a stiff wall at close approaches of Cu- and O-atoms, causing phase errors in their vibrations. The major parameters of the ZBL potential in this case are the inner and outer cutoff of the switching function. For Cu-O pairs, the inner cutoff corresponds to the characteristic distance at which potential starts to play a role in the interaction. It was chosen to be the maximum displacement at 900 K and is equal to 1.55 Å. The outer cutoff is selected to be equal to 3 % bond compression or 1.82 Å to ensure negligible contribution from ZBL at 10 K and moderate contribution at 300 K from measures of anharmonicity (Supplemental Material). The contribution of ZBL potential beyond the outer cutoff was set to zero. Overall, these MD simulations account for the experimental spectra temperature dependence with more success than the sTDEP results in the Supplemental that use lower-order anharmonicity. The discrepancies between simulation and experimental results are attributed to the simplified nature of the potential describing small interatomic separations.

4.4 Theory

Schrödinger-Langevin equation

Both classical and quantum Langevin equations are phenomenological equations that include randomness in forces or energies. For the classical Langevin equation, the damping and fluctuations depend on velocity, $\vec{v}(t)$, with time derivatives being accelerations that relate to forces. The Schrödinger equation, based on energy, is adapted as

$$\frac{\partial \psi}{\partial t} = -i(\mathcal{H}/\hbar)\psi - U\psi + l(t)V\psi, \quad (4.2)$$

where \mathcal{H} is the Hamiltonian without fluctuations or damping and U is a constant that gives the rate of damping of ψ . The $l(t)$ gives random fluctuations (normalized as below), and V is a constant giving the strength of coupling between wavefunction and fluctuations. After a time Δt , the wavefunction $\psi(t + \Delta t)$ evolves to

$$\psi(t + \Delta t) = \psi(t) + \frac{\partial \psi}{\partial t} \Big|_t \Delta t, \quad (4.3)$$

$$\psi(t + \Delta t) = \psi(t) \left[1 - i(\mathcal{H}/\hbar)\Delta t - U\Delta t + V \int_t^{t+\Delta t} l(t') dt' \right], \quad (4.4)$$

$$\psi^*(t + \Delta t) = \psi^*(t) \left[1 + i(\mathcal{H}^*/\hbar)\Delta t - U\Delta t + V^\dagger \int_t^{t+\Delta t} l^*(t'') dt'' \right], \quad (4.5)$$

giving the probability density

$$\psi^*(t+\Delta t)\psi(t+\Delta t) = \psi^*(t)\psi(t) - 2\psi^*(t)U\psi(t)\Delta t + \psi^*(t)V^\dagger V\psi(t) \int_{t''=t}^{t+\Delta t} \int_{t'=t}^{t+\Delta t} l^*(t') l(t'') dt' dt'', \quad (4.6)$$

where the imaginary terms have canceled their complex conjugates. The time shifts of dt' and dt'' are independent. Without an absolute reference, the time correlations depend on the difference of the two times, $\tau = t'' - t'$

$$\psi^*(t+\Delta t)\psi(t+\Delta t) = \psi^*(t)\psi(t) - 2\psi^*(t)U\psi(t)\Delta t + \psi^*(t)V^\dagger V\psi(t) \int_0^{\Delta t} \langle l^*(0) l(\tau) \rangle_{\text{th}} d\tau, \quad (4.7)$$

where $\langle \rangle_{\text{th}}$ denotes the thermodynamic average of the integrations in Eq. 4.6.

When U and V are zero, the Schrödinger equation is recovered in Eq. 4.2, and normalization gives $\langle \psi | \psi \rangle_{\text{th}} = 1$. Equation 4.7 shows that the parameter U causes a loss of wavefunction amplitude and probability density, but by setting

$$2U = V^\dagger V, \quad (4.8)$$

if the time correlation $\langle l^*(0) l(\tau) \rangle_{\text{th}}$ is normalized in Δt , there is a cancellation of the last two terms of Eq. 4.7 and

$$\langle \psi(t + \Delta t) | \psi(t + \Delta t) \rangle_{\text{th}} = 1. \quad (4.9)$$

Probability is therefore conserved if fluctuations are the source of the dissipation, as set by Eq. 4.8. This is a result of the fluctuation-dissipation theorem for quantum mechanics. The assumptions that V is a constant and that the time structure of $l(t)$ is included accurately in Eq. 4.7 allows us to neglect the higher powers of Δt in the time evolution of $\psi(t)$.

The Schrödinger-Langevin equation is [29]

$$\frac{\partial \psi}{\partial t} = -i(\mathcal{H}/\hbar)\psi - \frac{1}{2}V^\dagger V\psi + l(t)V\psi . \quad (4.10)$$

The fluctuation function $l(t)$ has a zero mean, so for large τ

$$\frac{1}{\tau} \int_0^\tau l(t) dt = 0 . \quad (4.11)$$

The autocorrelation function of $l(t)$ is $P_l(t)$

$$P_l(t) = \frac{1}{\tau} \int_0^\tau l^*(t+t') l(t') dt' , \quad (4.12)$$

$$P_l(t) = \langle l^*(t) l(0) \rangle_{\text{th}} , \quad (4.13)$$

where the average over time τ is recognized as the thermodynamic average of $l(t)$ shifted with respect to itself.

Inelastic Scattering and Diffuse Inelastic Intensity

In the incoherent approximation, the inelastic intensity is [30–32]

$$I(\omega) = \mathcal{K} \int_{-\infty}^{\infty} \exp(i\omega t) \langle \psi^*(t) \psi(0) \rangle_{\text{th}} dt . \quad (4.14)$$

For cubic crystals \mathcal{K} is

$$\mathcal{K} = \frac{k_f}{k_i} \frac{N}{M} \exp(-2W) \frac{Q^2}{3} \frac{\sigma}{2\pi\hbar} , \quad (4.15)$$

where N is the number of atoms, M is the atomic mass, σ is the neutron scattering cross section, and \vec{Q} is the momentum transfer. The ratio of final to initial wavevectors, k_f/k_i , accounts for the change in flux from the change in the neutron velocity after scattering. The $\psi(t)$ describes the dynamics of the center-of-mass of a nucleus that scatters the neutron.

The inelastic spectrum of Eq. 4.14 requires a product of

$$\psi(0) = \psi_0(0) + l(0)V\psi_0(0) , \quad (4.16)$$

$$\psi^*(t) = \psi_0^*(0) \left[\exp\left(-i\omega_0 t - \frac{1}{2}V^2 t\right) + V^\dagger \int_0^t l^*(t') dt' \right] , \quad (4.17)$$

where ψ_0 is the amplitude of the wavefunction when $V = 0$ and the energy of the oscillator is $\hbar\omega_0$. Following the approach of Eqs. 4.6 to 4.13, the thermodynamic average is

$$\begin{aligned} \langle \psi^*(t)\psi(0) \rangle_{\text{th}} &= |\psi_0|^2 \\ &\times \left[\exp(-i\omega_0 t) \exp\left(-\frac{1}{2}V^2 t\right) + V^2 P_I(t) \right]. \end{aligned} \quad (4.18)$$

There are no cross terms in Eq. 4.18 owing to Eq. 4.11 and $\langle \psi_0^*(0)|\psi_0(0) \rangle = 1$.

After the Fourier transforms of Eq. 4.18, Eq. 4.14 for the inelastic intensity has two terms

$$I(\omega)/\mathcal{K} \propto \frac{V^2}{(\omega - \omega_0)^2 + V^4} + V^2 \tilde{\mathcal{P}}_I(\omega). \quad (4.19)$$

The first term is the familiar spectrum of a damped harmonic oscillator, a Lorentzian function about ω_0 of breadth V^2 , with integrated area of π for all V^2 .

The second term in Eq. 4.19 is from the fluctuations. It is new for inelastic scattering. An instantaneous time correlation $P_I(t) = \delta(t)$ is a simple example. Its Fourier transform, $\tilde{\mathcal{P}}_I(\omega) = 1/\sqrt{2\pi}$, is a flat, diffuse, white-noise background in the inelastic intensity. Although this term is new in the context of inelastic scattering, for elastic scattering a diffuse intensity is well known for disordered materials [3].

The assumption $P_I(t) = \delta(t)$ is convenient, but brings unphysical consequences. Its spectrum extends to infinite ω , which is a consequence of an instantaneous shift in phase. This discontinuity in t gives an infinite $\partial\psi/\partial t$ (or an infinite energy in Eq. 4.2), and the area of $\tilde{\mathcal{P}}_I(\omega)$ is divergent. Physically, $P_I(t) = \delta(t)$ must be moderated with a breadth in time. We expect $P_I(t)$ to peak at $t = 0$ with some spread in time, τ_1 , as in the generalized Langevin equation [33]. Its Fourier transform, $\tilde{\mathcal{P}}_I(\omega)$, suppresses the DII at large ω . A large τ_1 gives more suppression of high frequencies in the inelastic spectrum.

DII in cuprite

The two-fold coordination of Cu-atoms in cuprite (Fig. 4.3a) is unusually low. Figure 4.3b (derived from Fig. 3 in Ref. [6]) shows the partial phonon DOS of Cu-atoms and of O-atoms in cuprite at 300 K. It suggests a natural approximation for the partial DOS of Cu-atoms as a mode with frequency 3 THz (12 meV), and the partial DOS of O-atoms as a mode of 17 THz (70 meV). With these very different frequencies, the dynamics of Cu- and O-atoms can be treated as independent, local Einstein oscillator modes.

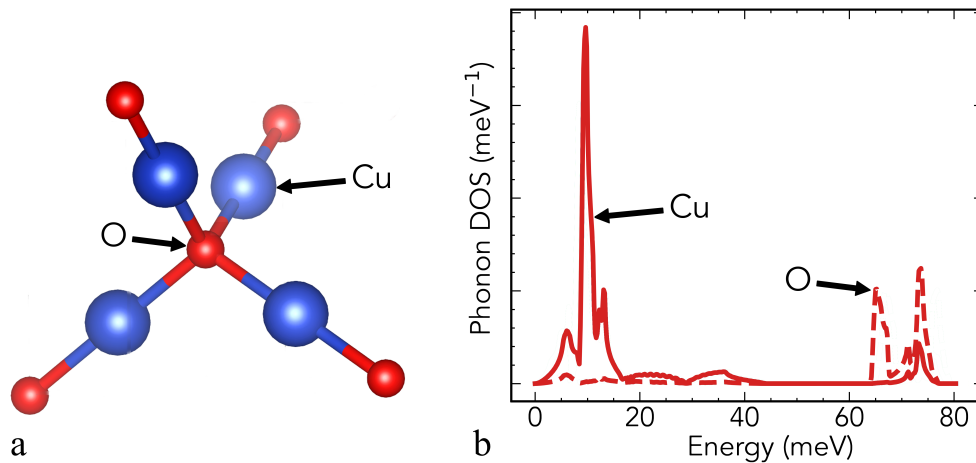


Figure 4.3: Atom arrangement and phonon density of states in cuprite. (a) Tetrahedral arrangement of Cu-atoms about O-atom in cuprite. (b) Phonon partial DOS from sTDEP calculations using second-order terms at 300 K. Solid curves are Cu-atoms, dashed are O-atoms.

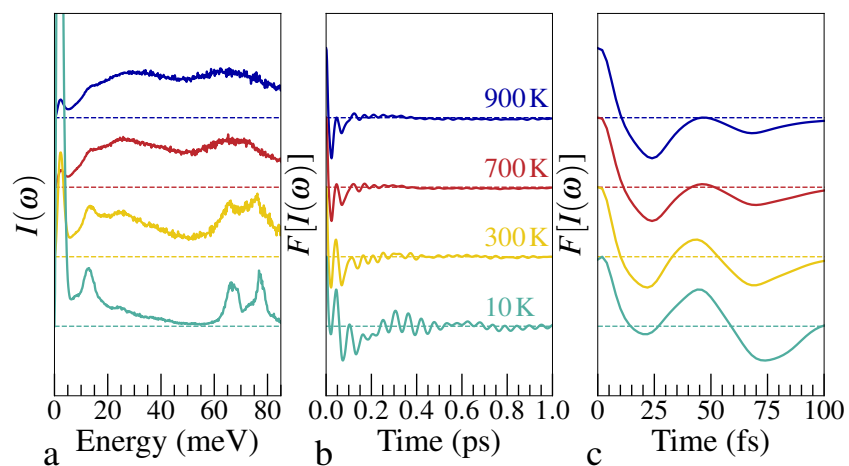


Figure 4.4: Characteristic timescale of DII in cuprite from Fourier transform of vibrational spectra. (a) Average inelastic intensity from left column of Fig. 2, and (b) its Fourier transform. (c) Fourier transform from 0 to 100 fs. ($F[I(\omega)] \equiv P(t)$) Temperatures from top to bottom are 900 K, 700 K, 300 K, and 10 K.

With small vibrational displacements at low temperatures, the interatomic forces are approximately harmonic, having a linear increase in phase with time (Fig. 4.1a). Crisp phonon dispersions are seen at 10 K in Fig. 5.1. When the atoms vibrate with larger amplitudes, the interatomic forces depart from harmonic behavior as the O- and Cu-atom neighbors approach each other more closely.

Intensities and energies

The scattering intensity from the Schrödinger-Langevin equation, Eq. 4.19, has two terms that depend on V , which parameterizes both the damping and the coupling to the noise function, $l(t)$. The Lorentzian function for the damped harmonic oscillator is normalized, but the DII is not normalizable without further information on how high frequencies in the spectrum are suppressed by the finite time of the Cu-O interactions. We can, however, compare the maximum intensities of the two features, since the maximum height of the Lorentzian goes as V^{-2} and the broad DII goes as $V^2/\sqrt{2\pi}$ (for a δ -function time correlation of $l(t)$). Assuming the peaks at 12 and 70 meV in Fig 4.4a are Lorentzian functions, and taking the DII at 45 meV, we obtain relative values of V^2 of approximately 0.63 at 10 K, 1.6 at 300 K, 2.7 at 700 K, 3.6 at 900 K. These relative values show that V^2 increases approximately linearly with temperature, T .

A calibration for the physical values of V^2 is possible using the breadths of the phonon peaks. Assuming they are Lorentzian functions, their energy broadening from 10 K to 300 K gives a V^2 at 300 K, allowing the scaling of the relative values of V^2 for O-atoms for higher temperatures of $V^2 \simeq 1.6 \times 10^{11} + 9.5 \times 10^8 T$ in units of s^{-1} (and T in K). This trend is approximately 60% smaller for the modes associated with Cu-atoms, but this lower-energy region of the phonon spectrum has contributions from multiple phonon branches and is less reliable.

Intensities and times

Figure 4.4b shows Fourier transforms of the experimental scattering intensities. The shortest periodicities, which are visible at low temperatures, are at 17 THz. Their time structure at 10 K shows a modulation at 3 THz. These frequencies of 3 and 17 THz correspond to oscillation frequencies of Cu and O-atoms shown in the partial DOS curves of Fig. 4.3b. The oscillations at 17 THz are strongly damped at higher temperatures, consistent with the broadened peaks in Fig. 4.4a centered around 25 and 70 meV. These broadenings in Fig. 4.4a can be used to extract coherence times, τ_c in the usual way for damped harmonic oscillators of Lorentzian lineshape, and assuming no lifetime broadening at 10 K. The peak around 70 meV, in the range of O-atom vibrations, has a τ_c of approximately 1,000 fs at 300 K, 600 fs at 700 K, 400 fs at 900 K. The diffuse band around 25 meV is more difficult to analyze because it is in the range of multiple lower-energy phonon branches, and is not entirely consistent with Cu atom dynamics, which are centered around

12 meV and not 25 meV. Nevertheless, the broad spectral feature around 25 meV has approximate τ_c of 2,700 fs at 300 K, 1,700 fs at 700 K, 1,000 fs at 900 K. (The peak broadenings at 10 K are dominated by the energy spread of the phonon bands and the resolution of the instrument.)

Figure 4.4c shows the shortest time correlations at the four temperatures. The peak at $t=0$ has a narrow breadth, but it is wider than the δ -function obtained for a flat background over the same range of energy. This breadth does not change significantly with temperature, but dominates the area of the time correlation function $P(t)$ at high temperature. It is consistent with the experimental DII of Fig. 5.1 which has an intensity that grows with temperature (the intensity of the DII clearly dominates the area of the $I(\omega)$ in the top curve of Fig. 4.4a), but has a shape that remains approximately the same with temperature. The limited range of energy of the phonon spectrum and the overlap of the DII with phonon peaks impair the quantitative information at the shortest time scales. From Fig. 4.4c I obtain an anharmonic interaction time of Cu and O-atoms of approximately 10 fs or less. This seems consistent with the characteristic time of a collision between stiff spheres. For comparison, the half-period of the O-atom vibrations is approximately 30 fs, and for Cu-atoms it is 160 fs. By modeling the spectra as broadened Lorentzian function on a background of DII, the fraction of DII in the spectra is 40% at 300 K, 70% at 700 K, 80% at 900 K.

In summary, the DII originates from the shortest time correlations, consistent with anharmonic interaction times of approximately 10 fs or less during close approaches of the O- and Cu-atoms as the phase advances more rapidly than for a harmonic oscillation. Although the 17 THz oscillations of the O-atom extend to long times at 10 K in Fig. 4.4b, they are damped at 300 K and higher temperatures, consistent with the broadening of peaks at 70 meV. These broadened peaks become a smaller fraction of the total intensity as the DII builds up across the energy range of the measured phonon spectra.

Model of semi-periodic phase shifts

Some periodicity in the anharmonic interactions is expected as O-atoms vibrate against Cu neighbors with a frequency $\omega_O/(2\pi) = 17$ THz. The second model assumes the anharmonic interactions occur twice per period of the O-atom vibration, when the O-atom is at its largest displacements and closest to its neighbors. The interactions occur at multiples of half-periods, $\tau = \pi/\omega_O$, but there is a distribution

in their strengths, and even their sign because for approximately half the interactions the neighboring O and Cu atoms may be displaced in the same direction. We assume the distribution of times for interactions are Gaussian functions centered at $n\tau$, and each Gaussian has a greater width with larger n as the memory of the initial interaction is lost.

The model in this section retains the approximation that the phase shifts are abrupt. Because each peak in $\psi(t)$ will have an overlap with a peak in $\psi(t - t')$ within the Gaussian spread in time, the net overlaps for $P(t)$ will remain constant and $P(t)$ is normalized. In this model, the changes in phase average to zero, but the mean-squared error in phase grows with time. For the first interaction, the stochastic change of $\psi_O(t)$ for O-atoms is assumed to have a standard deviation γ for its Gaussian probability distribution, so for the first interaction near the time 1τ

$$P_1(t) = \frac{1}{\sqrt{\pi} \gamma} \exp[-(t - \tau)^2/\gamma^2] . \quad (4.20)$$

The second change in phase adds to the phase uncertainty of the O-atom. With respect to the phase at the initial time, the time distribution is the convolution of Eq. 4.20 with itself, giving a Gaussian with standard deviation $\sqrt{2}\gamma$. The convolution with Eq. 4.20 is performed at each time interval $n\tau$

$$P_n(t) = \frac{1}{\sqrt{\pi} \gamma} \exp[-(t - \tau)^2/\gamma^2] * P_{n-1}(t) , \quad (4.21)$$

giving a total time correlation function for the phase errors of

$$P^{gd}(t) = \sum_{n=-\infty}^{\infty} \frac{1}{\sqrt{|n|} \pi \gamma} \exp[-(t - n\tau)^2/(|n| \gamma^2)] . \quad (4.22)$$

This $P^{gd}(t)$ is a sum of Gaussians spaced by intervals of τ , with widths increasing as $\sqrt{|n|}$. The case $n = 0$ can be taken as the limit $n \rightarrow 0$, giving a δ -function of unit area. (Terms with negative n give the time distributions of interactions that give the reference phase at $t = 0$.)

The intensity from Eq. 4.14 is calculated with the time correlation function of Eq. 4.22. Its Fourier transform is

$$\begin{aligned} P^{gd}(\omega) &= \int_{-\infty}^{\infty} \exp(-i\omega t) \\ &\times \sum_{n=-\infty}^{\infty} \frac{1}{\sqrt{|n|} \pi \gamma} \exp[-(t - n\tau)^2/(|n| \gamma^2)] dt . \end{aligned} \quad (4.23)$$

Substituting $t' = t - n\tau$ and taking Fourier transforms of the series of Gaussian functions:

$$P^{gd}(\omega) = \sum_{n=-\infty}^{\infty} \exp(-\omega^2 |n| \gamma^2 / 4) \exp(-in\omega\tau) . \quad (4.24)$$

Evaluating Eq. (4.24) as two geometric series for positive and negative n

$$P^{gd}(\omega) = \frac{1}{1 - \exp[-\omega^2 \gamma^2 / 4 + i\omega\tau]} + \text{c.c.} - 1 . \quad (4.25)$$

Reduction to a form with all terms being real is convenient, giving the intensity

$$\frac{I(\omega)}{V^2 \mathcal{K}} = \frac{1 - \exp[-\omega^2 \gamma^2 / 2]}{1 + \exp(-\omega^2 \gamma^2 / 2 - 2) \exp[-\omega^2 \gamma^2 / 4] \cos(\omega\tau)} . \quad (4.26)$$

The ratio γ/τ is the fractional amount of phase shift per half cycle.

Physical features of DII

A time-time correlation function $P^{gd}(t)$ is shown in Fig. 4.5a for $\gamma = \tau/3$. The corresponding $I(\omega)$ of Eq. (4.26) is shown in Fig. 4.5b for this $\gamma/\tau = 1/3$ and two other values, with a sharper peak at $\omega_0 = 2\pi/\tau$ for smaller γ/τ . For small and moderate values of γ/τ , at small ω the $I(\omega)$ of Eq. 4.26 rises with ω , and has a plateau at approximately $2\omega_0$. The roll-off at low frequencies seems consistent with the experimental intensity, as shown in Fig. 4.5c. Notably, there is little intensity variation with Q , which is presented vertically in Fig. 4.5c.

An assumption of the model from Sect. 4.4 is that the phase noise has only an instantaneous time correlation, so $P_1(t)$ of Eq. 4.20 is a Gaussian distribution from δ -functions having overlaps at different times. The instantaneous time correlation of $P(t=0) = \delta(t)$ requires an instantaneous change in the positions of neighboring atoms responsible for $l(t)$. Classically, this requires an infinite force, or quantum mechanically, the energy operator $i\hbar \partial\psi/\partial t$ is infinite. Physically, we expect interatomic anharmonic forces to be comparable to the forces on vibrating atoms, so the time correlation of $P(t)$ should be some fraction of the atom's vibrational period. A function with a spread of interaction times should be convoluted with $P(t)$, broadening it. This convolution is equivalent to multiplying the $I(\omega)$ in Fig. 4.5b by $\tilde{\mathcal{P}}_l(\omega)$ as in Eq. 4.19. So although the $I(\omega)$ from instantaneous interatomic interactions extends to infinity in ω , the finite time of the interaction provides attenuation at large ω . In principle, it should be possible to determine a characteristic time of anharmonic interatomic interactions by experimental measurements of the

width of the DII. The present measurements do allow a semi-quantitative analysis, as discussed with Fig. 4.4.

Two new parameters in the previous discussion are V and γ . The parameter V gives the coupling amplitude between a vibrational mode and the surrounding thermal bath. It plays the role of $\Phi(\vec{k}_1, \vec{k}_2, \vec{k}_3)$ in three-phonon processes, but V ignores the details of the wavevectors and the kinematics of energy and momentum conservation. On the other hand, the parameter V includes the phonon occupancy numbers, so V is expected to increase with T . In classical dynamics, the parameter γ gives the distribution of the changes in the phase of an O-atom for each non-harmonic interaction with a Cu-atom. The parameter γ value should also increase with larger thermal displacements at larger T .

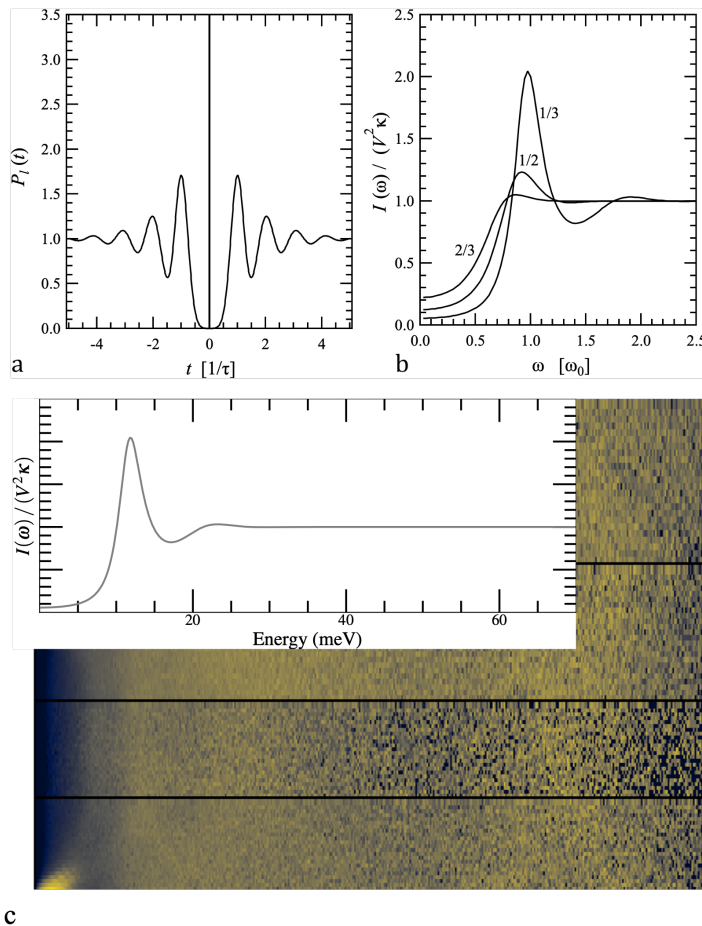


Figure 4.5: Illustration of semi-periodic model application to cuprite. (a) Time-time correlation function of Eq. (4.22) for $\gamma = \tau/3$. (b) Intensity $I(\omega)$ of Eq. 4.26 from Fourier transform of panel a, for different ratios of γ/τ (c) Comparison of predicted spectral weight from Cu-atoms with the experimental data from cuprite at 700 K.

The DII in cuprite is large and replaces the optical dispersions at high temperatures, but other anharmonic crystals retain discernible phonon dispersions without obvious DII. Nevertheless, DII may exist beneath phonon peaks in the spectra of other anharmonic crystals. DII looks like a background from other sources, so it may have been discarded in some previous experimental studies. There is evidence for DII in the phonon DOS of Ag_2O , which is structurally similar to cuprite and has weakly constrained O-M-O (M=Cu, Ag) bonds [34]. Other crystals that may show such DII include skutterudites, clathrate inclusion compounds, and methylammonium lead iodide perovskite. Rattling motions of atoms or molecules within the confines of hard walls give random departures from harmonic potentials and incoherent phase shifts [35–37]. The nonlinear interactions in these systems should be possible to study from the spectral features of DII. Open quantum systems are systems that interact with their environments, leading to loss of coherence and introduction of noise into their dynamics, as in the Caldeira–Leggett model, for example, [38, 39]. The DII gives new information on how phase noise depends on interatomic potentials, and gives physical estimates of characteristic decoherence times.

4.5 Summary and Conclusion

Cuprite, Cu_2O , has rapidly vibrating O-atoms with neighboring Cu-atoms having much slower dynamics. The bonds between O 2p and Cu 3d states have a nonlinear force-distance curve, with an increase in stiffness as the first-neighbor Cu and O atoms approach each other. During the close approach, there is a brief advance in phase of both Cu and O-atoms, compared to the dynamics in a harmonic potential. For the O-atoms, these phase shifts depend on the dynamics of their Cu neighbors, which are largely uncorrelated to the O-atom dynamics. The random timings of these brief phase shifts from anharmonic interactions cause diffuse inelastic intensity (DII). The DII from cuprite is largely incoherent, and has a broad energy spectrum owing to the brief 10 fs anharmonic interactions. The DII is present even at 300 K where it coexists with inelastic intensity from damped phonons. As the DII increases with temperature, there is a decrease in the spectral weight of the distinct phonon peaks.

A model based on the Schrödinger–Langevin equation gives inelastic scattering from damped phonons and shows how DII arises from phase shifts with random timings. The intensity and shape of the DII depend on the strength of coupling to the noise bath and the timing of the anharmonic interactions. At higher temperatures, the coupling to the noise source, and the intensity of the DII, increase linearly with

T . The coupling parameter V^2 increases with temperature from approximately 10^{11} to 10^{12} s^{-1} .

Ab initio simulations of Cu_2O with stochastic temperature-dependent effective potentials showed some diffuse features that resemble DII, but not with the intensity and breadth of the experimental measurements. Molecular dynamics simulations gave better spectral intensities when a Langevin thermostat was used (see Supplemental), but this thermostat did not account for the correlation between the atom positions and the phase noise. Simulations with the best agreement with experiment included the addition of a harder potential at closer approaches of the Cu- and O-atoms.

4.6 Supplemental Materials

Multiphonon correction

The multiphonon correction was performed in the incoherent scattering approximation. The procedure is iterative, and was described in [40]. The general formula for n -phonon scattering is

$$S_n(q, \varepsilon) = s_n(q) \int_{-\infty}^{\infty} A_1(\varepsilon - \varepsilon') A_{n-1}(\varepsilon') d\varepsilon' , \quad (4.27)$$

or using $*$ to denote convolution

$$S_n(q, \varepsilon) = s_n(q) (A_1(\varepsilon) * A_{n-1}(\varepsilon)) , \quad n \geq 2 , \quad (4.28)$$

where $A_1(\varepsilon)$ is the one-phonon density of states (DOS). The $s_n(q)$ are obtained from the expansion of the Debye-Waller factor.

$$s_n(q) = \frac{(2W(q))^n}{n!} e^{-2W(q)} . \quad (4.29)$$

Here $s_n(q)$ depends only on the magnitude of the momentum transfer $q = |\vec{Q}|$. The $A_1(\varepsilon)$ is obtained iteratively, starting with an approximation for the phonon DOS, and using it to correct the experimental data set for multiphonon scattering at all q , recovering a more reliable $A_1(\varepsilon)$ for each iteration.

Figure 4.6 shows the scattering intensity and the multiphonon correction as a function of $|\vec{Q}|$ for the single crystal of cuprite at 900 K. The $|\vec{Q}|$ ranges from 0 to 10 \AA^{-1} , which accounts for all zones in the single crystal data. Each zone was corrected for multiphonon scattering before folding into the first Brillouin zone. Figure 4.6 shows the intensity of the multiphonon scattering, although the subtraction was

performed in 3D space in different zones. Some of the higher zones were not used if they suffered from too much multiphonon scattering (comparable to the 1-phonon scattering), or were truncated by the kinematics of the time-of-flight technique.

Higher-Order Anharmonicity and Coherence

The previous report on the thermal expansion of cuprite near room temperature [6] describes in detail the sTDEP computations used for the results in Fig. 4.7 (left column) below. This earlier work suggested that phonon interactions beyond the third order are required, even at 300 K. A comparison of Fig. 1 to the experimental dispersions in the main text shows that the linewidths from sTDEP are qualitatively inadequate to account for the phonon spectra of cuprite at 700 K and 900 K. The phonon self-energy corrections for the fourth-order loop diagram do not have an imaginary component, so better calculations with a many-body theory approach may require five-phonon processes or higher. The phase space for such multiphonon kinematics is vast. To my knowledge, there are no reports of complete calculations with five-phonon processes. Higher-order perturbation theory may not be appropriate for calculations of DII.

In principle, the MLIP calculations include effects from higher-order phonon anharmonicity (although it was not practical to isolate the contributions from 5-phonon diagrams, for example). With the MLIP approach, the main text shows a significant improvement in the agreement with the experimental results at 700 K and 900 K when the Langevin thermostat is employed (right column of Fig. 4.7). The Langevin thermostat gives a random component to the nuclear accelerations, which causes shifts in phase of the vibrational dynamics. This is evidence that the generation of DII requires randomness in the anharmonic interactions, not just large anharmonicity. Although the Langevin thermostat offers more accurate simulations, it gives random phase shifts at each time step, and not at the closest approach of Cu- and O-atoms. The Langevin thermostat does not account fully for the time dynamics of the O-atoms in cuprite, but it generates DII that is more realistic than obtained in the NVE ensemble.

Machine Learning Interatomic Potentials (MLIP) Construction

I used moment tensor potentials (MTP) [25] to model the interatomic interactions. Moment tensors are flexible basis functions helpful in learning the lattice dynamics of a system, including anharmonic effects [41]. The construction of machine learning interatomic potentials (MLIP) followed the procedure of Ref. [42]. I gen-

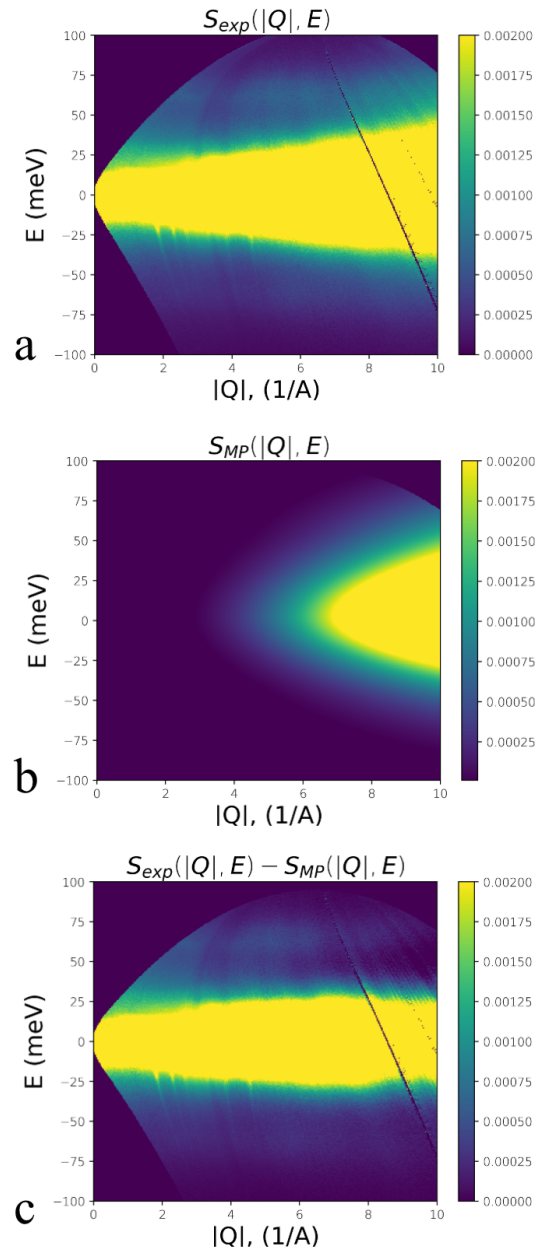


Figure 4.6: Illustration of subtraction of multiphonon correction of cuprite at 900 K. (a) $S_{exp}(|Q|, E)$, reduced data after background subtraction and rebinning into $|\vec{Q}|$. (b) calculated multiphonon correction $S_{MP}(|Q|, E)$ for $2 \geq n \leq 8$. (c) data of panel a after subtraction of multiphonon scattering, to the total scattering function $S_{exp}(|Q|, E)$.

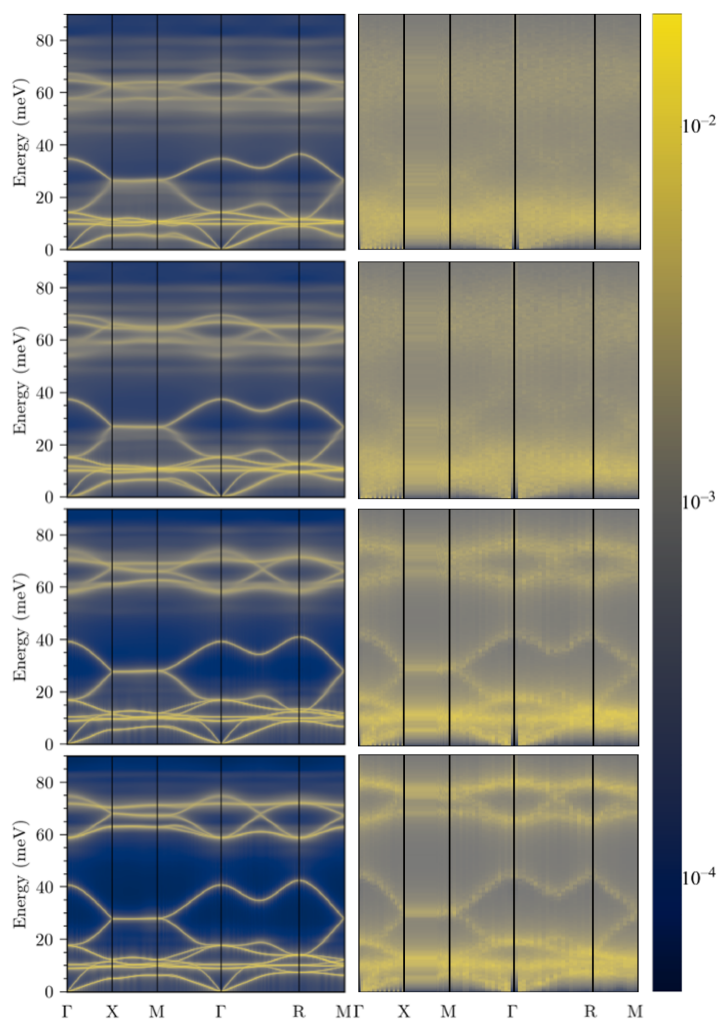


Figure 4.7: Comparison between vibrational spectra computed with sTDEP and autocorrelation function analyses. (left column) Calculated sTDEP phonon dispersions along high-symmetry directions. (right column) MD simulations with noise from Langevin thermostat. Temperatures from top to bottom: 900 K, 700 K, 300 K, and 10 K.

erated the MLIP from configurations actively sampled from molecular dynamics simulations at temperatures from 10 K to 900 K. The training set contained 523 configurations post-processed with VASP providing reference energies, forces, and stresses [19–22]. The average difference between the fitted potential and the potential from the *ab initio* model was 0.4 meV/atom. Using Eq. 3.17, I calculated a relative difference of 5 % in forces, and 4 % in stresses.

ZBL potential

To evaluate the effects of hard (or stiff) sphere interactions between adjacent Cu and O atoms, the MTP potential was modified with a ZBL potential [28] at low atomic separations. The transition between interatomic potentials is done by adding a function that smoothly decays to zero between an inner core radius and an outer cutoff. The potential energies along Cu-O bonds in cuprite of MTP and MTP-ZBL potentials are shown in Fig. 4.9 right panel. To calculate the curve, oxygen was displaced from its equilibrium position in Cu₂O octahedra along its nearest-neighbor direction.

Analyses of characteristic damping time

To estimate the coherence time of vibrations in cuprite, I first obtained an averaged inelastic intensity for the experimental data, and for molecular dynamics simulations with MTP-ZBL potential, using the data that provided the left and the middle column of Fig. 1 in the main text. I then performed Fourier transforms of these spectra. Their squared norms are presented in Fig. 4.8. From Fig. 4.8b and e, I can estimate the characteristic decay time of the autocorrelation function to be approximately equal 3×10^{-13} s ($\gamma/\tau_O = 6$) at 300 K to 1×10^{-13} s ($\gamma/\tau_O = 2$) at 900 K. These are consistent with the estimates in the main text.

In Fig. 4.8a and d the longer periodicity in the time domain, approximately 4×10^{-13} s corresponds to an energy of about 10 meV, which is the peak in the partial phonon DOS of Cu atoms [6]. The very short oscillations in Fig. 4.8b and e are truncation effects from the edge of the energy interval. Nevertheless, Fig. 4.8b shows that at high temperatures, the time correlation function becomes nearly a δ -function, consistent with the approximate $P_I(t)$ for the DII used in the main text.

The FWHM of the peak around $t = 0$ in Fig. 4.8c corresponds to the characteristic time of the measured DII from stiff Cu-O interactions. Figure 4.8c shows that this time is approximately 10 fs. The Fourier analyses of spectra obtained with the ZBL-MTP potential give a similar interaction time of 10 fs in Fig. 4.8f.

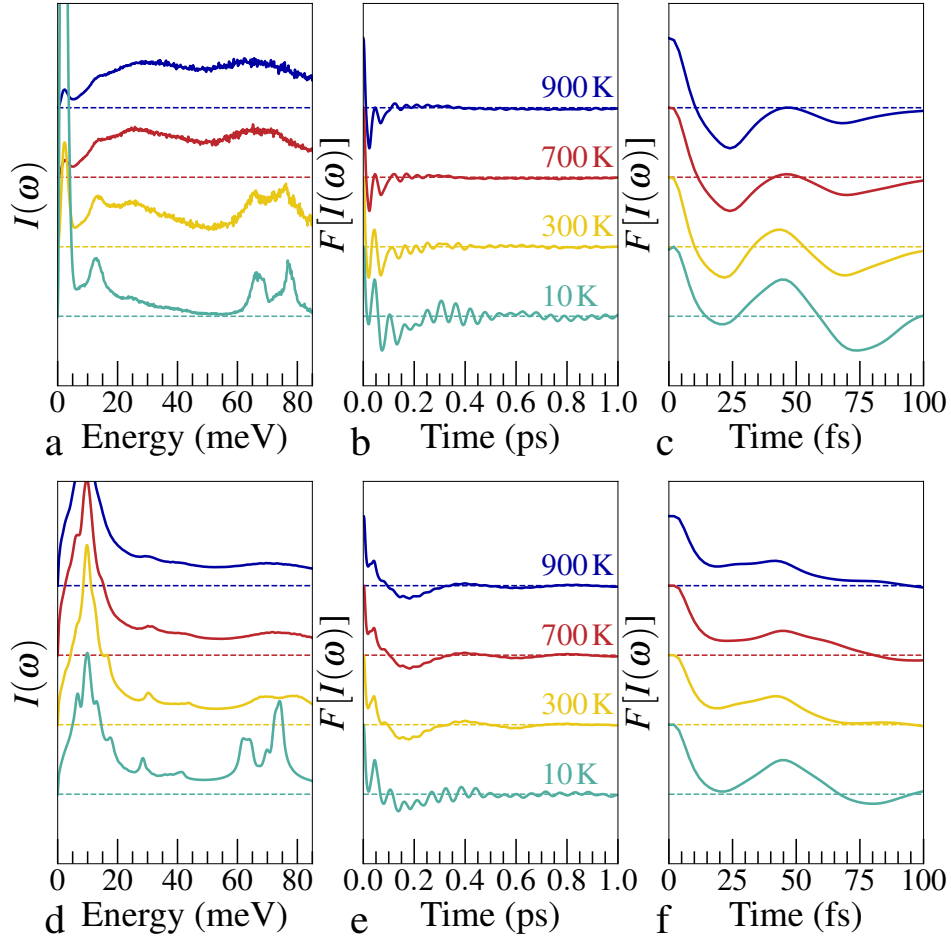


Figure 4.8: Average phonon density of states from Fig. 1 in the main text (left) and its Fourier transform (right). (a), (b), (c) for experimental data, and (d), (e), (f) for molecular dynamics simulations with a MTP-ZBL potential. Temperatures from top to bottom are: 900 K, 700 K, 300 K, and 10 K.

Measure of anharmonicity

To quantify anharmonicity in Cu_2O , I followed the procedure introduced in [43] and later used in [44]. The method analyzes how much the forces in molecular dynamics simulations deviate from the forces of an effective harmonic model, $F_{I,\alpha}^{(2)}$, with effective harmonic force constants $\Phi_{\alpha,\beta}^{I,J}$

$$F_{I,\alpha}^{(2)} = - \sum_{J,\beta} \Phi_{\alpha,\beta}^{I,J} \Delta R_J^\beta . \quad (4.30)$$

The anharmonic measure is computed as a relative error of an effective harmonic model averaged over the MD trajectory.

$$\sigma_{MD}^A = \sqrt{\frac{\sum_{I,\alpha} \left\langle \left(F_{I,\alpha}^{MD} - F_{I,\alpha}^{(2)} \right)^2 \right\rangle_T}{\sum_{I,\alpha} \left\langle \left(F_{I,\alpha}^{MD} \right)^2 \right\rangle_T}}, \quad (4.31)$$

where T is the time average over the MD trajectory. Similarly, an anharmonic contribution beyond second order can be introduced.

$$\sigma_{MD}^A = \sqrt{\frac{\sum_{I,\alpha} \left\langle \left(F_{I,\alpha}^{MD} - F_{I,\alpha}^{(2)} - F_{I,\alpha}^{(3)} \right)^2 \right\rangle_T}{\sum_{I,\alpha} \left\langle \left(F_{I,\alpha}^{MD} \right)^2 \right\rangle_T}}. \quad (4.32)$$

The $F_{I,\alpha}^{(3)}$ is the contribution to the force from third-order forceconstants $\Phi_{\alpha,\beta,\gamma}^{I,J,K}$

$$F_{I,\alpha}^{(3)} = -\frac{1}{2} \sum_{J,K,\beta,\gamma} \Phi_{\alpha,\beta,\gamma}^{I,J,K} \Delta R_J^\beta \Delta R_K^\gamma. \quad (4.33)$$

The configurations for anarmonicity quantification were sampled from 2 ps MD trajectories with 162 atoms supercell and a time step of 1 fs, resulting in a dataset of 2000 configurations for model fitting. Before sampling, a system was equilibrated for 20 ps at the corresponding temperature. The results are shown in Figure 4.9. The data indicate that the Cu_2O dynamics is anharmonic, especially when the inner potential is described by a ZBL potential. The anarmonicity measure for simulation with ZBL, $\sigma_{MD}^A > 0.8$, may give a threshold for candidates for materials to exhibit DII in vibrational spectra. Since DII originates from random phase alterations of atomic vibrations similar to interaction in hard wall potential, including high order forceconstants does not have a significant impact on the measure as seen from dashed lines in Figure 4.9. Comparing the corresponding value to the tables in [43], the potential candidates are perovskites and noble metal halides. However, I should note that using effective harmonic forceconstants reduces the anharmonic measure compared to the one presented in [43] since it partially includes anharmonic effects through dynamical matrix normalization.¹

¹In [43] the calculations assumes $\Phi_{\alpha,\beta}^{I,J}$, $\Phi_{\alpha,\beta,\gamma}^{I,J,K}$ obtained with finite differences method of the lattice Hamiltonian with respect to displacement, whereas in our work we use TDEP values which are temperature dependent computed from residue fitting of potential energy surface.

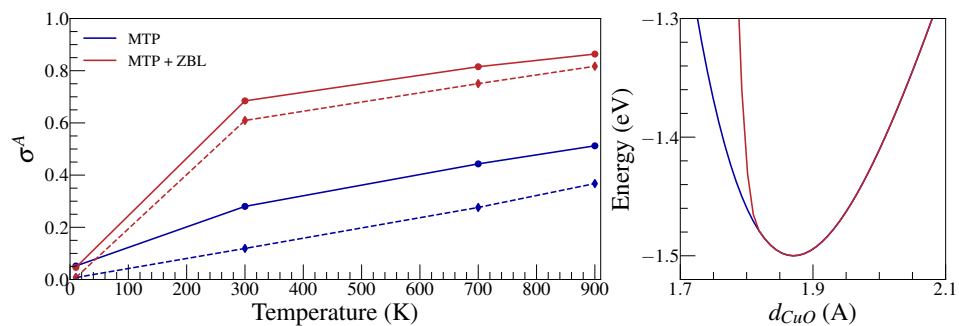


Figure 4.9: Anharmonicity quantification in cuprite. Left panel: anharmonicity measure for temperatures in Figure 2 of the main text. The blue color corresponds to Molecular Dynamics simulations with MTP describing interatomic interaction; results with MTP potential splined to ZBL are red; the anharmonicity measure after including third-order forceconstant contribution is shown with dashed lines. Right panel: potential energy along Cu-O bond for MTP (blue) and MTP-ZBL (red) potentials.

References

- [1] C. Saunders, V. Ladygin, D. Kim, C. Bernal-Choban, S. Lohaus, G. Granroth, D. L. Abernathy, and B. Fultz. Diffuse intensity from phonon noise in inelastic neutron scattering. *Phys. Rev. Mater.*, 9:024602, Feb 2025. doi: 10.1103/PhysRevMaterials.9.024602. URL <https://link.aps.org/doi/10.1103/PhysRevMaterials.9.024602>.
- [2] T. Egami and S. J. L. Billinge. *Underneath the Bragg Peaks*, volume 16 of *Pergamon Materials Series*. Pergamon, 2012. doi: <https://doi.org/10.1016/B978-0-08-097133-9.09992-5>. URL <https://www.sciencedirect.com/science/article/pii/B978008097133909992>.
- [3] J. M. Cowley. *Diffraction Physics*. North-Holland Personal Library. Elsevier, Amsterdam, 3 edition, 1995. doi: <https://doi.org/10.1016/B978-0-444-82218-5.50025-0>. URL <https://www.sciencedirect.com/science/article/pii/B9780444822185500250>.
- [4] B. Fultz and J. M. Howe. *Transmission Electron Microscopy and Diffractometry of Materials Fourth Edition*. Springer-Verlag, Heidelberg, 2013. doi: <https://doi.org/10.1007/978-3-642-29761-8>.
- [5] D. Olds, C. N. Saunders, M. Peters, T. Proffen, J. Neuefeind, and K. Page. Precise implications for real-space pair distribution function modeling of effects intrinsic to modern time-of-flight neutron diffractometers. *Acta Crystallogr. A*, 74(4):293–307, 2018. doi: 10.1107/S2053273318003224. URL <https://doi.org/10.1107/S2053273318003224>.
- [6] C. N. Saunders, D. S. Kim, O. Hellman, H. L. Smith, N. J. Weadock, S. T. Omelchenko, G. E. Granroth, C. M. Bernal-Choban, S. H. Lohaus, D. L. Abernathy, and B. Fultz. Thermal expansion and phonon anharmonicity of cuprite studied by inelastic neutron scattering and *ab initio* calculations. *Phys. Rev. B*, 105:174308, May 2022. doi: 10.1103/PhysRevB.105.174308. URL <https://link.aps.org/doi/10.1103/PhysRevB.105.174308>.
- [7] D. L. Abernathy, M. B. Stone, M. J. Loguillo, M. S. Lucas, O. Delaire, X. Tang, J. Y. Y. Lin, and B. Fultz. Design and operation of the wide angular-range chopper spectrometer ARCS at the Spallation Neutron Source. *Rev. Sci. Instrum.*, 83(1):015114, 2012. doi: 10.1063/1.3680104. URL <https://doi.org/10.1063/1.3680104>.
- [8] T.E. Mason, D. Abernathy, I. Anderson, J. Ankner, T. Egami, G. Ehlers, A. Ekkebus, G. Granroth, M. Hagen, K. Herwig, J. Hodges, C. Hoffmann, C. Horak, L. Horton, F. Klose, J. Larese, A. Mesecar, D. Myles, J. Neuefeind, M. Ohl, C. Tulk, X-L. Wang, and J. Zhao. The Spallation Neutron Source in Oak Ridge: A powerful tool for materials research. *Physica B Condens. Matter*, 385-386:955–960, 2006. ISSN 0921-4526. doi: 10.1016/j.physb.2006.05.

281. URL <https://www.sciencedirect.com/science/article/pii/S092145260601177X>.
- [9] O. Arnold, J. C. Bilheux, J. M. Borreguero, A. Buts, S.I. Campbell, L. Chapon, M. Doucet, N. Draper, R. Ferraz Leal, M. A. Gigg, V. E. Lynch, A. Markvardsen, D. J. Mikkelson, R. L. Mikkelson, R. Miller, K. Palmen, P. Parker, G. Passos, T. G. Perring, P. F. Peterson, S. Ren, M. A. Reuter, A. T. Savici, J. W. Taylor, R. J. Taylor, R. Tolchenov, W. Zhou, and J. Zikovsky. Mantid—data analysis and visualization package for neutron scattering and μ sr experiments. *Nucl. Instrum. Meth. A*, 764:156–166, 2014. ISSN 0168-9002. doi: <https://doi.org/10.1016/j.nima.2014.07.029>. URL <https://www.sciencedirect.com/science/article/pii/S0168900214008729>.
- [10] O. Hellman, I. A. Abrikosov, and S. I. Simak. Lattice dynamics of anharmonic solids from first principles. *Phys. Rev. B*, 84:180301(R), 2011. doi: 10.1103/PhysRevB.84.180301. URL <https://link.aps.org/doi/10.1103/PhysRevB.84.180301>.
- [11] O. Hellman, P. Steneteg, I. A. Abrikosov, and S. I. Simak. Temperature dependent effective potential method for accurate free energy calculations of solids. *Phys. Rev. B*, 87:104111, Mar 2013. doi: 10.1103/PhysRevB.87.104111. URL <https://link.aps.org/doi/10.1103/PhysRevB.87.104111>.
- [12] O. Hellman and I. A. Abrikosov. Temperature-dependent effective third-order interatomic force constants from first principles. *Phys. Rev. B*, 88:144301, Oct 2013. doi: 10.1103/PhysRevB.88.144301. URL <https://link.aps.org/doi/10.1103/PhysRevB.88.144301>.
- [13] D. S. Kim, O. Hellman, J. Herriman, H. L. Smith, J. Y. Y. Lin, N. Shulumba, J. L. Niedziela, C. W. Li, D. L. Abernathy, and B. Fultz. Nuclear quantum effect with pure anharmonicity and the anomalous thermal expansion of silicon. *Proc. Natl. Acad. Sci. USA*, 115(9):1992–1997, 2018. ISSN 0027-8424. doi: 10.1073/pnas.1707745115. URL <https://www.pnas.org/content/115/9/1992>.
- [14] F. Knoop, N. Shulumba, A. Castellano, J. P. Alvarinhas Batista, R. Farris, M. J. Verstraete, M. Heine, D. Broido, D. S. Kim, J. Klarbring, et al. Tdep: Temperature dependent effective potentials. *J. Open Source Software*, 9(94), 2024.
- [15] A. Castellano, J. P. A. Batista, and M. J. Verstraete. Mode-coupling theory of lattice dynamics for classical and quantum crystals. *J. Chem. Phys.*, 159(23):234501, 12 2023. ISSN 0021-9606. doi: 10.1063/5.0174255. URL <https://doi.org/10.1063/5.0174255>.

- [16] A. A. Maradudin and A. E. Fein. Scattering of neutrons by an anharmonic crystal. *Phys. Rev.*, 128:2589–2608, 1962. doi: 10.1103/PhysRev.128.2589. URL <https://link.aps.org/doi/10.1103/PhysRev.128.2589>.
- [17] D. C. Wallace. *Thermodynamics of Crystals*. J. Wiley, New York, 1998.
- [18] J. Lahnsteiner and M. Bokdam. Anharmonic lattice dynamics in large thermodynamic ensembles with machine-learning force fields: CsPbBr₃, a phonon liquid with Cs rattlers. *Phys. Rev. B*, 105:024302, Jan 2022. doi: 10.1103/PhysRevB.105.024302. URL <https://link.aps.org/doi/10.1103/PhysRevB.105.024302>.
- [19] G. Kresse and J. Hafner. Ab initio molecular dynamics for liquid metals. *Phys. Rev. B*, 47:558–561, 1993. doi: 10.1103/PhysRevB.47.558. URL <https://link.aps.org/doi/10.1103/PhysRevB.47.558>.
- [20] G. Kresse and J. Hafner. Ab initio molecular-dynamics simulation of the liquid-metal–amorphous–semiconductor transition in germanium. *Phys. Rev. B*, 49:14251–14269, 1994. doi: 10.1103/PhysRevB.49.14251. URL <https://link.aps.org/doi/10.1103/PhysRevB.49.14251>.
- [21] G. Kresse and J. Furthmüller. Efficiency of *ab initio* total energy calculations for metals and semiconductors using a plane-wave basis set. *Comput. Mater. Sci.*, 6(1):15 – 50, 1996. ISSN 0927-0256. doi: 10.1016/0927-0256(96)00008-0. URL <http://www.sciencedirect.com/science/article/pii/0927025696000080>.
- [22] G. Kresse and J. Furthmüller. Efficient iterative schemes for *ab initio* total-energy calculations using a plane-wave basis set. *Phys. Rev. B*, 54:11169–11186, 1996. doi: 10.1103/PhysRevB.54.11169. URL <https://link.aps.org/doi/10.1103/PhysRevB.54.11169>.
- [23] G. Kresse and D. Joubert. From ultrasoft pseudopotentials to the projector augmented-wave method. *Phys. Rev. B*, 59:1758–1775, Jan 1999. doi: 10.1103/PhysRevB.59.1758. URL <https://link.aps.org/doi/10.1103/PhysRevB.59.1758>.
- [24] J. P. Perdew, K. Burke, and M. Ernzerhof. Generalized gradient approximation made simple. *Phys. Rev. Lett.*, 77:3865–3868, Oct 1996. doi: 10.1103/PhysRevLett.77.3865. URL <https://link.aps.org/doi/10.1103/PhysRevLett.77.3865>.
- [25] A. V. Shapeev. Moment tensor potentials: A class of systematically improvable interatomic potentials. *Multiscale Modeling & Simulation*, 14(3): 1153–1173, 2016. doi: 10.1137/15M1054183. URL <https://doi.org/10.1137/15M1054183>.

- [26] A. P. Thompson, H. M. Aktulga, R. Berger, D. S. Bolintineanu, W. M. Brown, P. S. Crozier, P. J. in't Veld, A. Kohlmeyer, S. G. Moore, T. D. Nguyen, R. Shan, M. J. Stevens, J. Tranchida, C. Trott, and S. J. Plimpton. LAMMPS - a flexible simulation tool for particle-based materials modeling at the atomic, meso, and continuum scales. *Comp. Phys. Comm.*, 271:108171, 2022. doi: 10.1016/j.cpc.2021.108171.
- [27] C. N. Saunders. *Thermal Behavior of Cuprous Oxide: a Comprehensive Study of Three-Body Phonon Effects and Beyond*. PhD thesis, California Institute of Technology, 2022. URL <https://resolver.caltech.edu/CaltechTHESIS:05262022-015714738>.
- [28] J. F. Ziegler and J. P. Biersack. The stopping and range of ions in matter. In *Treatise on heavy-ion science: Volume 6: Astrophysics, Chemistry, and Condensed Matter*, pages 93–129. Springer, 1985.
- [29] N. G. Van Kampen. *Stochastic Processes in Physics and Chemistry*. North-Holland Personal Library. Elsevier, Amsterdam, 3 edition, 2007. doi: <https://doi.org/10.1016/B978-044452965-7/50020-9>.
- [30] L. Van Hove. Correlations in Space and Time and Born Approximation Scattering in Systems of Interacting Particles. *Phys. Rev.*, 95:249–262, 1954. doi: 10.1103/PhysRev.95.249. URL <https://link.aps.org/doi/10.1103/PhysRev.95.249>.
- [31] S. W. Lovesey. *Theory of Neutron Scattering from Condensed Matter*. Clarendon Press, United Kingdom, 1984. ISBN 0-19-852017-4. URL http://inis.iaea.org/search/search.aspx?orig_q=RN:16036521.
- [32] G. L. Squires. *Introduction to the Theory of Thermal Neutron Scattering*. Cambridge University Press, 3 edition, 2012. doi: 10.1017/CBO9781139107808.
- [33] N. Pottier. *Nonequilibrium Statistical Physics: Linear Irreversible Processes*. Oxford University Press, 2009.
- [34] T. Lan, C. W. Li, O. Hellman, D. S. Kim, J. A. Muñoz, H. Smith, D. L. Abernathy, and B. Fultz. Phonon quarticity induced by changes in phonon-tracked hybridization during lattice expansion and its stabilization of rutile TiO_2 . *Phys. Rev. B*, 92:054304, Aug 2015. doi: 10.1103/PhysRevB.92.054304. URL <https://link.aps.org/doi/10.1103/PhysRevB.92.054304>.
- [35] J. Dong, O. F. Sankey, G. F. Ramachandran, and P. F. McMillan. Chemical trends of the rattling phonon modes in alloyed germanium clathrates. *J. Appl. Phys.*, 87(11):7726–7734, 2000. doi: 10.1063/1.373447. URL <https://doi.org/10.1063/1.373447>.
- [36] I. Sergueev, K. Glazyrin, I. Kantor, M. A. McGuire, A. I. Chumakov, B. Klobes, B. C. Sales, and R. P. Hermann. Quenching rattling modes in skutterudites

- with pressure. *Phys. Rev. B*, 91:224304, Jun 2015. doi: 10.1103/PhysRevB.91.224304. URL <https://link.aps.org/doi/10.1103/PhysRevB.91.224304>.
- [37] A. C. Ferreira, S. Paofai, A. Létoublon, J. Ollivier, S. Raymond, B. Hehlen, B. Rufflé, S. Cordier, C. Katan, J. Even, and P. Bourges. Direct evidence of weakly dispersed and strongly anharmonic optical phonons in hybrid perovskites. *Commun. Phys.*, 3(1):48, Mar 2020. ISSN 2399-3650. doi: 10.1038/s42005-020-0313-7. URL <https://doi.org/10.1038/s42005-020-0313-7>.
- [38] A. O. Caldeira and A. J. Leggett. Path integral approach to quantum brownian motion. *Phys. A: Stat. Mech. Appl.*, 121(3):587–616, 1983.
- [39] A. O. Caldeira and A. J. Leggett. Influence of damping on quantum interference: An exactly soluble model. *Phys. Rev. A*, 31(2):1059, 1985.
- [40] V. F. Sears, E. C. Svensson, and B. M. Powell. Phonon density of states in vanadium. *Can. J. Phys.*, 73(11-12):726–734, 1995.
- [41] V. V. Ladygin, P. Yu. Korotaev, A. V. Yanilkin, and A. V. Shapeev. Lattice dynamics simulation using machine learning interatomic potentials. *Comput. Mater. Sci.*, 172:109333, 2020. ISSN 0927-0256. doi: <https://doi.org/10.1016/j.commatsci.2019.109333>. URL <https://www.sciencedirect.com/science/article/pii/S0927025619306329>.
- [42] I. S. Novikov, K. Gubaev, E. V. Podryabinkin, and A. V. Shapeev. The mlip package: moment tensor potentials with mpi and active learning. *Mach. Learn.: Sci. Technol.*, 2(2):025002, 2020. doi: 10.1088/2632-2153/abc9fe.
- [43] F. Knoop, Thomas A. R. Purcell, M. Scheffler, and C. Carbogno. Anharmonicity measure for materials. *Phys. Rev. Mat.*, 4(8):083809, 2020.
- [44] A. Castellano, J. P. Batista, and M. J. Verstraete. Mode-coupling theory of lattice dynamics for classical and quantum crystals. *J. Chem. Phys.*, 159(23), 2023.

Chapter 5

PHONON SECOND HARMONIC GENERATION IN SODIUM BROMIDE

Adapted from "Phonon second harmonic generation in NaBr studied by inelastic neutron scattering and computer simulation" [1].

5.1 Introduction

The classical theory of nonlinear media offers a simplified framework for understanding wave interactions in a nonlinear medium. In contrast to linear systems, the response of a nonlinear medium includes intermodulation branches¹ at the sums and differences of two strongly-excited frequencies, as reported for NaBr [2]. Also predicted are second harmonics (SH) of these frequencies, which are expected with intensities comparable to those of the if they are indeed phonon intermodulations. Second harmonic generation (SHG) is well-known in nonlinear optics, but has not been reported to date for anharmonic phonons. The prior study of NaBr [2] did not use an incident neutron beam of sufficient energy measure them, so a new set of measurements was undertaken to confirm the presence of IPS branches and to seek the SHG of phonons in NaBr.

In this chapter I report observations of SHG, with a new branch at 33 meV in INS spectra of NaBr. This SH feature is attributable to the frequency doubling of the transverse optical (TO) mode. The SH spectrum becomes increasingly broadened with temperature from 300, 425, 550, and 650 K. The origin of the SH branch is found with *ab initio* calculations and perturbation theory with cubic perturbations to second order. Molecular dynamics (MD) simulation on NaBr under comparable conditions reproduces the temperature dependence of the SHG in the classical limit. The quantum model predicts formation of second harmonic and intensity distribution between TO, IPS and SHG. The measured temperature dependence of the SH spectral intensity was fit with Planck factors for one excitation of 33 meV, and with two excitations of half the frequency. The temperature dependence of the SH feature is that of a single excitation at its (doubled) energy, which is the behavior of an independent quasiparticle of high energy.

¹Attributed to use intermodulation phonon sidebands (IPS) in the case of phonon intermodulation as defined in Section 2.

5.2 Experiment

The INS measurements were performed with the time-of-flight wide angular range chopper spectrometer, ARCS [3], at the Spallation Neutron Source [4]. I used the same single crystal studied previously in Ref. [2]. However, I took a new set of measurements with a higher incident energy of the neutron beam, and with less mass in the aluminum sample holder to suppress background and better reveal fine features in phonon spectra. The measurements were performed with the sample assembly in an electrical resistance furnace in vacuum at temperatures of 300 K, 425 K, 550 K, and 650 K. Data postprocessing included subtraction of background from the sample holder and sample environment, along with correction for multiphonon scattering in the incoherent approximation [5] at each Brillouin zone in the dataset. Some of the higher zones were incomplete owing to the kinematical limitations of the measurements or had a high fraction of multiphonon scattering. These were not included in the subsequent processing. After subtraction of the unwanted scattering, the data were folded back into an irreducible wedge in the first Brillouin zone. Additional details of experimental data postprocessing are given in the Supplemental Material section.

Figure 5.1 shows experimental phonon dispersions along high-symmetry crystallographic directions, after folding back to the first Brillouin zone. Especially at 300 K, the phonon dispersions at energies below 27 meV are consistent with the branches expected from a harmonic model. Nevertheless, the flat intermodulation sideband around the points X and K at approximately 27 meV is prominent, confirming the previous result [2]. A new feature is seen as a flat branch at all \vec{Q} around 33 meV at twice the energy of the bright horizontal branch at approximately 16.5 meV. These two new features are most clear in the data at 300 K. They shift to lower energies at 425 K. At high temperatures, the features begin to overlap with the optical modes. The TO mode shifts to lower energy with temperature from approximately 16.5 meV at 300 K to 15 meV at 650 K. The SH feature softens gradually with temperature, shifting from 33 meV at 300 K to 30 meV at 650 K. The breadth of this SH feature undergoes significant broadening with temperature, as seen by comparing the data at 300 K and 425 K.

5.3 Computation

Temperature dependent effective potential

Results in the Supplemental Material show that sTDEP predicts semi-quantitatively the formation of high-energy branches from IPS and SHG. Phonon lineshapes at

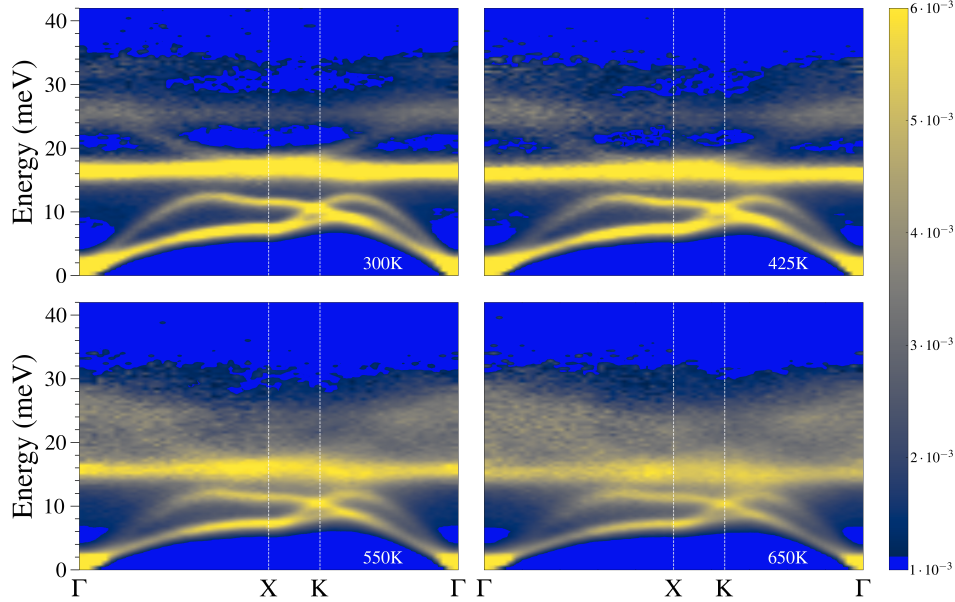


Figure 5.1: Inelastic neutron scattering data from NaBr single crystal. Each panel is normalized with respect to its total inelastic intensity (data are on a linear scale).

300 K from the sTDEP method are shown in Fig. 5.2a. The effective harmonic dispersion for the TO branch and the intensity from SHG are shown with white and orange lines, respectively. To analyze the origin of second harmonic in terms of three-phonon processes, I used a branch elimination technique similar to [2]. Specifically, I eliminated contributions from all three-phonon processes involving the transverse optical branch in the energy range between 14 meV and 16 meV (Fig. 5.2b). This involved setting to zero all three-phonon matrix elements $\Phi_{s's''}^{\vec{q}\vec{q}'\vec{q}''}$ in Eq. 2.11 that correspond to effective harmonic phonon frequencies $\omega_{\vec{q},s}$, $\omega_{\vec{q}',s'}$ or $\omega_{\vec{q}'',s''}$ in this energy interval.

Finally, I estimated the contributions to the scattering function around 31 meV from the coupling of harmonic modes through three phonon interactions. The total scattering function in the limit of small self-energies was approximated as

$$\sigma_{s,s'}^{q,q'}(\Omega) \propto \frac{2\omega_s^q \Gamma_{s,s'}^{q,q'}}{\left(\Omega^2 - (\omega_s^q)^2\right)^2}. \quad (5.1)$$

Figure 5.2c shows diffuse intensity around 31 meV as the original phonon lineshape obtained with sTDEP. The intensity was calculated as the partial contribution to the phonon spectral function at 31 meV and is computed for harmonic branches along high symmetry directions using Eqs. 2.11 and 5.1. The major contribution to the second harmonic spectral function is from the coupling between TO modes.

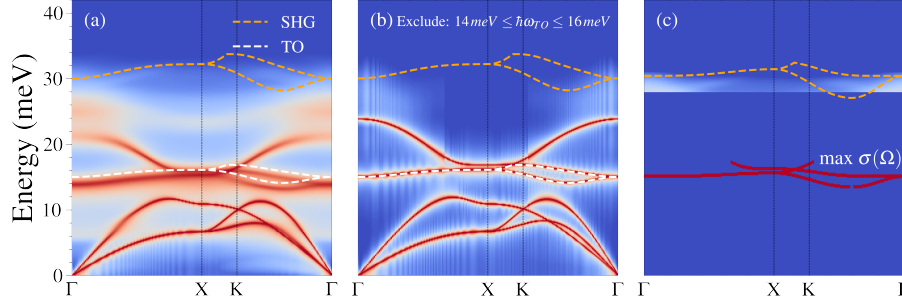


Figure 5.2: Illustration on band elimination technique. (a) sTDEP phonon dispersions along high-symmetry directions at 300 K. (b) phonon lineshapes at 300 K where contributions from three-phonon processes associated with transverse optical mode are set to zero. (c) harmonic modes that give the maximum contribution to the second harmonic spectral lineshape through three-phonon processes.

Molecular dynamics simulations with machine learning interatomic potential

The coupling of vibrational modes is an anharmonic phenomenon. It is expected to be stronger at higher temperatures, so classical molecular dynamics (MD) was used to simulate SHG. The spectral intensity was obtained by the Fourier transformation of a velocity-velocity autocorrelation function, projected onto \vec{Q} . These MD calculations required large supercells and extended times for good resolution of phonon features in \vec{Q} and ω [6]. The simulations were performed with a machine learning interatomic potential (MLIP), trained with input from density functional theory (DFT) calculations performed with VASP [7–10]. The DFT calculations used plane-wave basis sets, projector augmented wave (PAW) pseudopotentials, exchange-correlation functionals in the generalized gradient approximation (GGA) [11, 12], and supercells generated with thermally-displaced atoms with the sTDEP method [13]. These training supercells were $5 \times 5 \times 5$, containing 250 atoms. The k -grid was $3 \times 3 \times 3$, and the kinetic energy cutoff was 550 eV. The final training set contained 352 configurations.

A machine-learned moment-tensor potential [14] was used to model the interatomic interaction in classical MD simulations with the LAMMPS code [15]. The supercell size was $30 \times 30 \times 30$ with 216,000 atoms. The projected velocity-velocity autocorrelation functions came from 200 statistically independent cuts of 50 ps MD trajectories to ensure convergence in the time domain. The results from MD calculations were post-processed with the package VVCORE [16]. The Supplemental provides additional details on MLIP construction and computational data analyses.

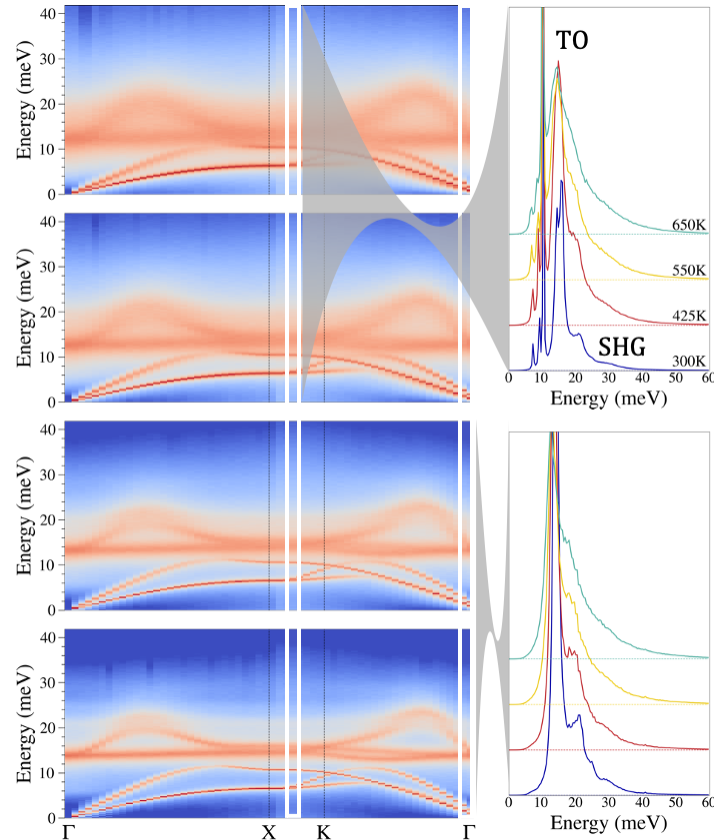


Figure 5.3: Vibrational spectra of NaBr obtained with autocorrelation function analyses. (left column) Phonon dispersions along high-symmetry directions calculated by projected velocity-velocity autocorrelation function method. (right column) Temperature dependence of vibrational spectrum at particular q -cuts. Temperatures from top to bottom: 650 K, 550 K, 425 K, and 300 K.

The vibrational spectra along high symmetry directions obtained from autocorrelation function analyses of MD trajectories are shown in Fig. 5.3. The calculations using MLIP better reproduce the temperature dependence of the second harmonic. The SH is the flat spectral branch around 30 meV at 300 K. At high temperatures, this branch is expected to soften in energy by twice as much as the TO mode. However, the vibrational spectra are spreading above 40 meV at 650 K owing to the substantial decrease in the lifetime of the SH. The shortening of the SH is shown in Fig. 5.3 (right column) for individual q -points. The SH is distinct at 300 K and 425 K, but it merges with the optical modes at 550 K and 650 K.

5.4 Theory

Nonlinear medium

The process of second harmonic generation can be understood with a classical model of two oscillations in a nonlinear medium. The input wavefunction ψ_{in} is a superposition of two damped harmonic oscillator waves with frequencies ω_a and ω_b and characteristic damping parameters γ_a and γ_b

$$\psi_{in} = \psi_{in}^a + \psi_{in}^b, \quad (5.2)$$

$$\begin{aligned} \psi_{in} &= A/2(e^{i\omega_a t} + e^{-i\omega_a t})e^{-\gamma_a t} \\ &+ B/2(e^{i\omega_b t} + e^{-i\omega_b t})e^{-\gamma_b t}. \end{aligned} \quad (5.3)$$

For a linear medium, the output ψ_{out} is proportional to the input wavefunction ψ_{in} . For a nonlinear medium, ψ_{out} is a sum of linear and coupling terms

$$\begin{aligned} \psi_{out} &= \psi_{out}^{(1)} + \psi_{out}^{(2)} + \dots \\ \psi_{out} &= \sum_{a'} \chi_{a'}^{(1)} \psi_{in}^{a'} + \sum_c \sum_{a'b'} \psi_{in}^{a'} \chi_{a'b'c}^{(2)} \psi_{in}^{b'} + \dots \end{aligned} \quad (5.4)$$

I consider only the first nonlinear contribution to the output wavefunction

$$\psi_{out}^{(2)} = 2\psi_{in}^a \tilde{\chi}_{ab}^{(2)} \psi_{in}^b + \psi_{in}^a \tilde{\chi}_{aa}^{(2)} \psi_{in}^a + \psi_{in}^b \tilde{\chi}_{bb}^{(2)} \psi_{in}^b, \quad (5.5)$$

where $\tilde{\chi}_{a'b'}^{(2)} = \sum_c \chi_{a'b'c}^{(2)}$. Writing ψ_{in}^a and ψ_{in}^b in Eq. 5.3 in the form of cosines,

$$\psi_{out}^{(2)} = \left[\left\{ \tilde{\chi}_{aa} A^2 / 2 e^{-2\gamma_a t} + \tilde{\chi}_{bb} B^2 / 2 e^{-2\gamma_b t} \right\} \right. \quad (5.6)$$

$$\left. + \tilde{\chi}_{ab} AB \left\{ \cos(\omega_a + \omega_b) + \cos(\omega_b - \omega_a) \right\} e^{-(\gamma_a + \gamma_b)t} \right. \quad (5.7)$$

$$\left. + \left\{ \tilde{\chi}_{aa} A^2 \cos(2\omega_a) e^{-2\gamma_a t} + \tilde{\chi}_{bb} B^2 \cos(2\omega_b) e^{-2\gamma_b t} \right\} \right]. \quad (5.8)$$

Expressions 5.7 and 5.8 give new peaks in the phonon spectra of an anharmonic crystal with frequencies $\omega_a + \omega_b$, $\omega_b - \omega_a$, $2\omega_a$ and $2\omega_b$. The components $\omega_a + \omega_b$ and $\omega_a - \omega_b$ were discussed in [2]. Here, I report the observation of the second harmonic with frequency $2\omega_a$ in the anharmonic vibrational spectrum.

The new modes are shown in Fig. 5.4. The positions and broadenings of the SH and IPS spectral features were obtained from the centers and linewidths of transverse acoustic and optical modes at lower energies. The final lineshapes of the IPS and SH take into account the resolution function calculated as a limit of linewidth at zero temperature. The parameters A and B are equal to the area under the Lorentzian peak at the corresponding q -point. This is in agreement with the wavefunction

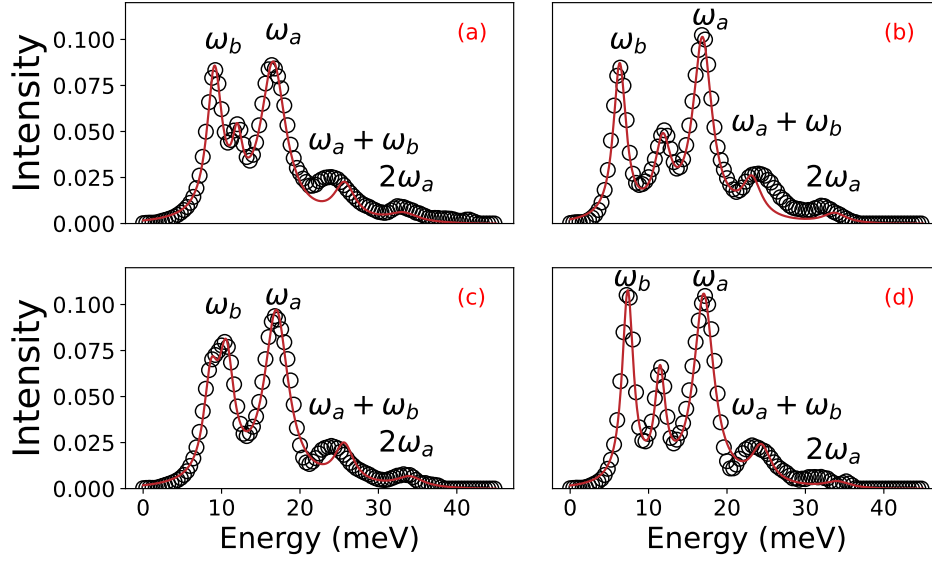


Figure 5.4: Predictions of the classical model of a nonlinear medium (solid red line) for experimental spectra (open circles) at 300 K for (a) $\vec{Q} = [0.6 \ 0 \ 0.6]$, (b) $[0.6 \ 0 \ 0]$, (c) $[0.75 \ 0 \ 0.75]$, (d) $[1 \ 0 \ 0]$.

representation of the oscillations in Eq. 5.3. The coupling constants $\tilde{\chi}_{aa}$ and $\tilde{\chi}_{ab}$ were calculated from the ratio of second harmonic intensity and squared intensity of the transverse optical mode corrected with thermal occupancy factors as shown below. The $\tilde{\chi}_{aa}$ exhibits some variation ranging from approximately 1.2-1.6 meV at the zone center to 0.6-0.7 meV at the zone edge. For the modeling, I choose a mean value of 1.1 meV for the zone. The corresponding coupling constant for the IPS, $\tilde{\chi}_{ab}$, was evaluated near the zone edge to minimize overlapping contributions from the longitudinal optical branch. The resulting average coupling constant for IPS is 3.7 meV. This value is in excellent agreement with the previous report [2].

Heisenberg-Langevin equation

For later comparison to SHG, I first summarize phonon sideband generation by solving a quantum Hamiltonian for three coupled phonons j, j', j'' as in [2]

$$H_{sys} = H_0 + \hbar \frac{\eta}{2} (\hat{a}_j^\dagger + \hat{a}_j) (\hat{a}_{j'}^\dagger + \hat{a}_{j'}) (\hat{a}_{j''}^\dagger + \hat{a}_{j''}), \quad (5.9)$$

where $H_0 = \sum_{k=j,j',j''} \hbar \omega_k \left(\hat{a}_k^\dagger \hat{a}_k + 1/2 \right)$ is the Hamiltonian of three uncoupled oscillators. Taking $j = j'$ as a simplified example and denoting $\hat{a}_j = \hat{a}$ and $\hat{a}_{j''} = \hat{b}$ Hamiltonian takes a form

$$H_{sys} = H_0 + \hbar \frac{\eta}{2} (\hat{a}^\dagger + \hat{a})^2 (\hat{b}^\dagger + \hat{b}). \quad (5.10)$$

Neglecting terms in the rotating wave approximation (RWA) in quantum optics, and neglecting terms that do not conserve energy ($a^\dagger a^\dagger b^\dagger$ and aab)

$$H_{\text{sys}} = H_0 + \hbar \frac{\eta}{2} (\hat{a}^\dagger \hat{a} + \hat{a} \hat{a}^\dagger) (\hat{b}^\dagger + \hat{b}). \quad (5.11)$$

If the phonons are coupled to a thermal bath, the spectral function at equilibrium can be found with the Heisenberg–Langevin equation [2]

$$S_{ab}[\omega] = \frac{\hbar \gamma_a (n_a + \frac{1}{2})}{2m\omega_a} |\chi_a + 2i\omega_b g^2 \chi_a^2 \chi_{ab} \bar{\chi}_{ab}|^2, \quad (5.12)$$

where χ_a and χ_{ab} , are defined as phonon propagation susceptibility functions for oscillators a and b , and n is the Planck thermal occupation factor $n(\omega, T) = [\exp(\hbar\omega/k_b T) - 1]^{-1}$.

$$\chi_a^{-1} = -i(\omega - \omega_a) + \frac{\gamma_a}{2}, \quad (5.13)$$

$$\chi_{ab}^{-1} = -i(\omega - \omega_a - \omega_b) + \frac{\gamma_b}{2}, \quad (5.14)$$

$$\bar{\chi}_{ab}^{-1} = -i(\omega - \omega_a + \omega_b) + \frac{\gamma_b}{2}. \quad (5.15)$$

Here, ω and γ are frequency and decay rate of the oscillator.

The formation of phonon second harmonics is similar. I use Eq. 5.12 with two modes being degenerate but having an independent set of quantum operators, following the quantum optics analogy for second harmonic generation and downconversion [17]. In [17], the authors treat SHG and laser impulse with sets of quantum operators that do not commute. As a result, Eq. 5.12 transforms into

$$S_{aa}[\omega] = \frac{\hbar \gamma_a (n_a + \frac{1}{2})}{2m\omega_a} |\chi_a + 2i\omega_a g^2 \chi_a^2 \chi_{aa} \bar{\chi}_{aa}|^2, \quad (5.16)$$

where χ_a and χ_{aa} , are defined as phonon propagation susceptibility functions for oscillator a and its SH

$$\chi_{aa}^{-1} = -i(\omega - 2\omega_a) + \frac{\gamma_a}{2}, \quad (5.17)$$

$$\bar{\chi}_{aa}^{-1} = -i\omega + \frac{\gamma_a}{2}. \quad (5.18)$$

In Eq. 5.12 for the IPS formation and Eq. 5.16 for the SHG, the first term corresponding to $g = 0$ is the Lorentzian peak at frequency ω_a . The two equations differ in their last terms. The spectral intensity for the TO mode a , the IPS, and the

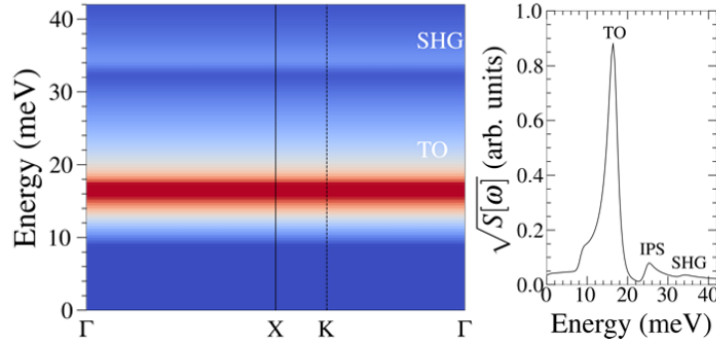


Figure 5.5: Results from the Heisenberg–Langevin model for SHG at 300 K in the medium-strong coupling regime. (left) Spectral function from Heisenberg–Langevin applied to two coupled TO phonons. (right) Intensity distribution between TO, IPS and SHG.

SH are obtained by combining the second terms of Eq. 5.12 and Eq. 5.16

$$S[\omega] = \frac{\hbar\gamma_a(n_a + \frac{1}{2})}{2m\omega_a} |\chi_a + 2i\omega_b g^2 \chi_a^2 \chi_{ab} \bar{\chi}_{ab} + 2i\omega_a g^2 \chi_a^2 \chi_{aa} \bar{\chi}_{aa}|^2. \quad (5.19)$$

Predictions at 300 K for medium-strong coupling ($g \simeq \gamma_a$) are shown in Fig. 5.5. In the left panel the TO mode, ω_a , is represented as a flat energy branch with a center at 16.5 meV and FWHM γ_a equal to 3 meV. Equation 5.16 predicts the formation of a diffuse second harmonic around 33 meV. In the right panel the intensity distribution is estimated for the TO, IPS and SH features using the Eq. 5.19 with ω_b and γ_b equal to 8.2 meV and 2.1 meV. The integrated intensities of TO, IPS and SHG peaks $I_{TO} : I_{IPS} : I_{SH}$ are in the ratio of 26:2:1, in agreement with the experimental values of 27:4:1.

Second Harmonic Generation in NaBr

Measurements from 300 to 650 K were used to obtain thermal trends of the intensities of the TO modes and the SH features. I obtained temperature-dependent lifetimes and thermal shifts of these features in the experimental data by averaging over the first Brillouin zone with a grid of $171 \times 171 \times 171$ points in reciprocal space after the data were corrected by the single crystal postprocessing procedures explained earlier. (This included the subtraction of multiphonon scattering in the incoherent approximation.) Fitting the spectral features gave average energies, breadths, and intensities (details of peak fitting are presented in the Supplemental) The fits and results are presented in Fig. 5.6.

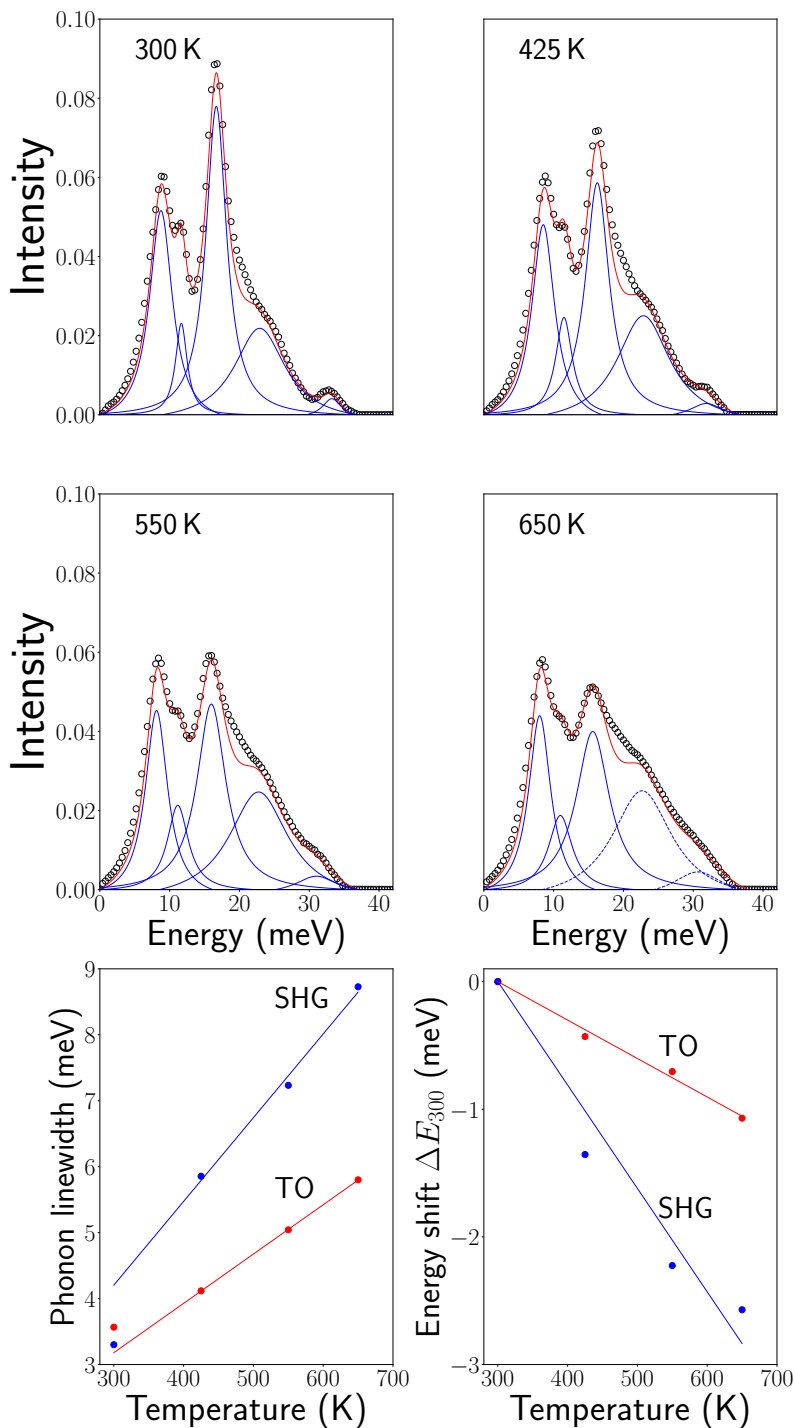


Figure 5.6: Temperature dependence of averaged vibrational spectra: left and center columns - vibrational spectra at 300 K, 425 K, 550 K, 650 K with fitted peaks. Spectra are normalized to 1. (bottom left) temperature dependence of the phonon breadth, and (bottom right) phonon energy shift, with respect to 300 K data for transverse optical (TO) mode and second harmonic generation (SHG). Slopes of the bottom plots are presented in the text.

Figure 5.6 shows how the average energies shift with temperature. The SH peak around 33 meV shifts approximately twice as much as the corresponding TO peak ($7 \cdot 10^{-3}$ meV/K for TO versus $13 \cdot 10^{-3}$ meV/K for SH). This is as expected if the TO energy is doubled for the SH. The temperature dependence of the broadening ($-3 \cdot 10^{-3}$ meV/K for TO versus $-8 \cdot 10^{-3}$ meV/K for SH) shows that at all temperatures, the widths in energy of the SH peak are approximately twice the widths of the TO peaks. From Eq. 5.8 I expect the lifetime of the SH to be approximately half as long as the lifetime of its corresponding TO modes. The temperature dependence of the shifts and broadenings of the spectral features are consistent with SHG, but do not definitively differentiate between a quasiparticle with an energy of 33 meV, or the creation of two phonons of 16.5 meV (although 2-phonon scattering was subtracted from the data).

To distinguish SHG from the excitation of two TO phonons, I analyzed thermal occupancy based on intensities from Fig. 5.6 before normalization and thermal factor corrections. The temperature dependences of intensities were fit to the sum of Planck occupancy factors for one phonon with energy $2\omega_{TO}$, and two phonon occupancy factors with energy ω_{TO} .

$$I(T) = I_0(300) + I_1 n(2\omega_{TO}, T) + I_2 n^2(\omega_{TO}, T), \quad (5.20)$$

where $I_0(300)$ is the intensity of the feature at 300 K, and $n(\omega, T)$ is the Planck occupancy factor for frequency ω and temperature T . The expression of Eq. 5.20 was fit to the intensities of spectral features in the experimental data at $2\omega_{TO}$, and it was found that the term I_1 accounts for 88 % of the temperature dependence of the mode at 33 meV. The SH can be treated as an independent quasiparticle from the viewpoint of statistical mechanics. The distinct SH peak in Fig. 5.6 allows for a thermal analysis that was not practical for the data from the IPS in [2]. To check the method of fitting with Eq. 5.20, I fit to the temperature dependence of the TO modes. This gave 94 % of the TO mode as originating with single phonon scattering, nearly the 100% that is expected.

I obtained an anharmonic coupling constant $\tilde{\chi}_{aa}$ as

$$\tilde{\chi}_{aa} \approx \frac{I_{SHG}}{n(\omega_{SHG}, T)} \bigg/ \frac{I_{TO}^2}{n^2(\omega_{TO}, T)}. \quad (5.21)$$

Here, I_{TO} and I_{SHG} are the integrated intensities of the TO and SH peaks. Planck factors $n(\omega, T)$ account for the thermal occupancy difference between two modes. The estimated coupling constant lies in the range from 1 meV at 300 K to 3 meV at

650 K. This is in agreement with the value from [2] and corresponds to a medium-strong coupling regime.

5.5 Discussion

The formation of SH intensity is a coherent phenomenon involving two TO phonons entangled in a quantum sense. The TDEP calculations show that the lifetime of the SH feature is related to the lifetime of the TO mode through the corresponding three-phonon process. This agrees with experimental data for the INS data at 300 K. For higher temperatures, many-body theory beyond the third order is required to account for the short lifetimes of the SH feature. At high temperatures, the output of two interacting modes in a nonlinear medium is better described by the classical model (Eq. 5.5) and classical MD simulations. A more accurate treatment of spectral intensity requires solving the Heisenberg–Langevin equations without the rotating wave approximation, and including high-order phonon processes in the Hamiltonian. Finally, none of the models presented here account for the q -dependence of the phonon sidebands or the second harmonic. As shown in [18] and [2], the approximation of flat branches works well for the alkali halide crystals where the TO mode is approximately flat in the Brillouin zone and the TA mode exhibits small variation across the energy region responsible for the IPS formation. If the branches are dispersive, an anharmonic crystal can still have SH and IPS features, but they will have a broad energy spectrum.

The anharmonicity of NaBr is dominated by interactions along the nearest neighbor bond ($\Phi_{NaNaBr}^{\alpha\alpha\alpha}$ or $\Phi_{NaBrBr}^{\alpha\alpha\alpha}$) [19]. These interactions play a major role in the decay and recombination processes involving TO phonons. Second harmonic generation from phonon-phonon coupling likely appears in other anharmonic systems with flat branches of high intensity. This effect alters the total phonon intensity distribution, which might significantly impact thermodynamic properties at finite temperatures. Other candidates for SHG are alkali halides [2, 18] and thermoelectrics [20, 21] where intrinsic localized modes were observed, and perovskite materials and cuprites that have anharmonic phonons in flat bands.

5.6 Conclusion

The observation of second harmonics in phonon spectra completes the picture of a excitations in a nonlinear medium which predicts new frequencies of $\omega_a + \omega_b$, $\omega_a - \omega_b$, and $2\omega_a$ or $2\omega_b$. The present measurements were performed with a redesigned sample environment having less aluminum to create background intensity than in

[2], and the subtraction of multiphonon scattering should have eliminated 2-phonon processes from the experimental spectral intensity. An analysis of the temperature dependence of the spectral feature from the second harmonic of TO modes showed that the thermal occupancy was that of a single excitation at high frequency, and not two single excitations. For purposes of statistical mechanics, the second harmonic behaves as a single quasiparticle.

5.7 Supplemental Material

Stochastic Temperature-Dependent Effective Potential Method Lineshapes in the limit of small self energies

When Γ and Δ are small, the one-phonon neutron cross section is [22, 23]

$$\sigma_s^q(\Omega) \propto \frac{2\omega_s^q \Gamma_s^q}{\left[\Omega^2 - (\omega_s^q)^2 - 2\omega_s^q \Delta_s^q\right]^2 + \left(2\omega_s^q \Gamma_s^q\right)^2}. \quad (5.22)$$

I simplify Eq. 5.22 when Γ and Δ are small. By replacing Γ with $\Gamma_{s,s'}^{q,q'}$ I get Eq. 3.2 of the main text.

$$\sigma_{s,s'}^{q,q'}(\Omega) \propto \frac{2\omega_s^q \Gamma_{s,s'}^{q,q'}}{\left[\Omega^2 - (\omega_s^q)^2\right]^2}. \quad (5.23)$$

Machine Learning Interatomic Potentials (MLIP) Construction

I used moment tensor potentials (MTP) [14] to model the interatomic interactions. Moment tensors are flexible basis functions helpful in learning the lattice dynamics of a system, including anharmonic effects [24]. The construction of machine learning interatomic potentials (MLIP) followed the procedure of Ref. [25]. I generated the MLIP from configurations actively sampled from molecular dynamics simulations at temperatures from 300 K to 650 K. The training set contained 352 configurations post-processed with VASP providing reference energies, forces, and stresses [7–10]. The average difference between the fitted potential and the potential from the *ab initio* model was 0.1 meV/atom. Using Eq. 3.17, I calculated a relative difference of 3 % in forces, and 4 % in stresses.

Analyses of Second Harmonic Generation through third order anharmonicity and beyond

To perform sTDEP computations of temperature dependent phonon lineshapes presented in Fig. 5.7 I followed the procedure described in Supplemental of [26].

Compared to the experimental spectral function in the main text, the linewidths from sTDEP reproduce the features in the phonon spectra of NaBr at 300 K and 425 K, and even account for the frequency shift of the second harmonic feature. However, the lifetime broadening of SHG at 550 K and 650 K is not reproduced. The phonon self-energy corrections for the fourth-order loop diagram do not have an imaginary component, so better calculations with many-body theory perturbation theory may require five-phonon processes or higher. The phase space for such multi-phonon kinematics is vast. To my knowledge, there are no reports of complete calculations with five-phonon processes.

Fitting to Lorentzian peaks

The phonon peaks in Fig. 2 of the main text were fit to the sum of the Lorentzian functions.

$$I(x) = y_0 + \frac{A}{\pi} \frac{\gamma/2}{(x - \mu)^2 + (\gamma/2)^2}, \quad (5.24)$$

where x denotes energy; μ is the center of the Lorentzian; γ is the width of the corresponding peak at half maximum; A is the area under the Lorentzian peak, and the y_0 is the offset chosen to be the same for all peaks. The parameters of peak fits to the data of Fig. 2 of the main text are shown in Table 5.2.

I also analyzed data at several points of the high symmetry directions of the NaBr Brillouin zone. The results, along with peak fits of Eq. 5.24, gave TO and SHG shifts and broadenings as shown in Fig. 5.8. The temperature dependencies of the shifts and broadenings of the transverse optical mode and second harmonic spectral components are also shown in Fig. 5.8. Both the shifts and broadenings of the SHG components are twice that of the TO spectral components. The trend in thermal linewidth supports the argument that the lifetime of the second harmonic component is half as long as the lifetime of the transverse optical mode at each temperature. Numerical values are given in Table 5.1.

Planck factor for quasiparticle

An important step in the data reduction was removal of 2-phonon scattering in the incoherent approximation. Nevertheless, I made an effort to assess the SH feature at 33 meV as either a 2-phonon process or as a single excitation that could be considered an independent quasiparticle. The approach was to use the temperature dependence of its intensity, and fit the intensity $I(T)$ to a single Planck factor for an excitation of

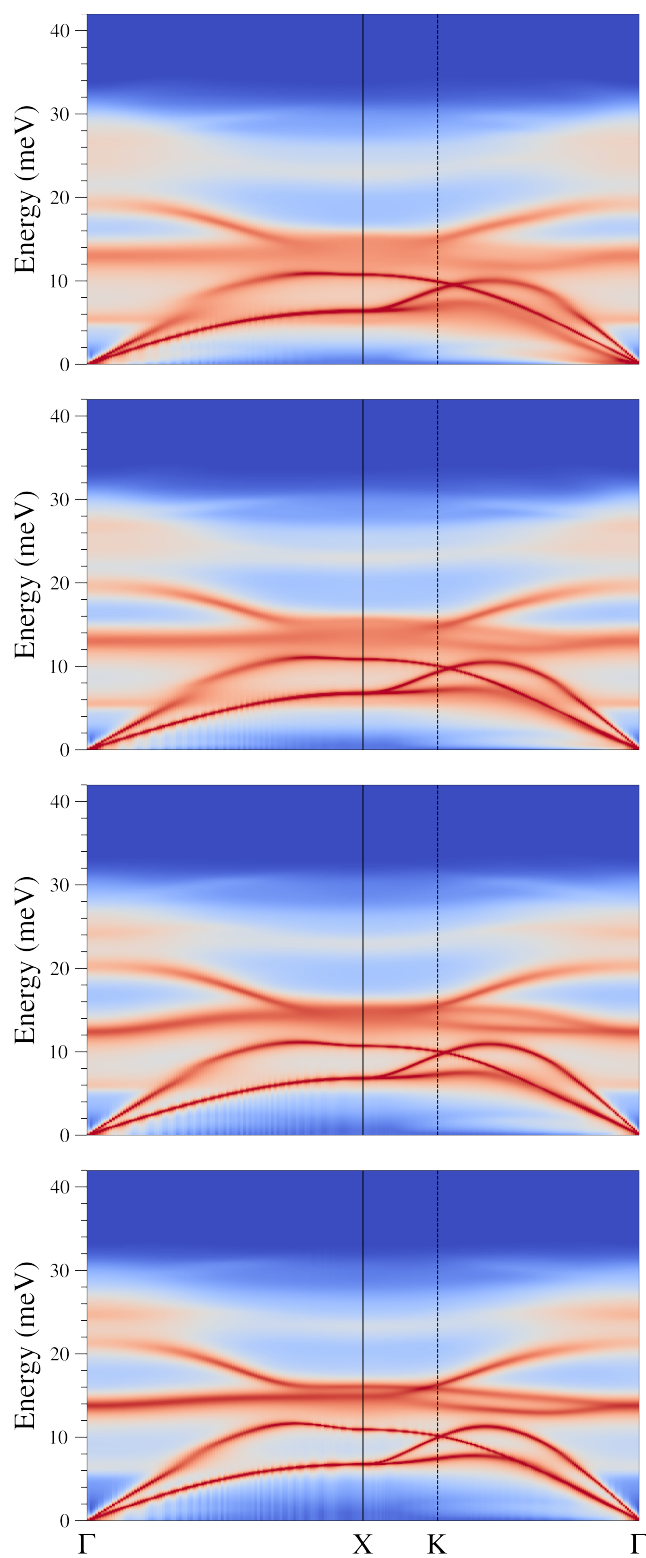


Figure 5.7: Calculated sTDEP phonon dispersions along high-symmetry directions for temperatures from top to bottom: 650 K, 550 K, 425 K, and 300 K.

33 meV, or a product of two Planck factors for excitations at 16.5 meV. As discussed in the main text with Eq. 21, the intensities were fit to the expression

$$I(T) = I_0(300) + I_1 n(2\omega_{TO}, T) + I_2 n^2(\omega_{TO}, T) , \quad (5.25)$$

where $I_0(300)$ is the intensity of the feature at 300 K, and $n(\omega, T)$ is the Planck occupancy factor for frequency ω and temperature T . As a check with the fitting procedure, the same approach was used for the TO mode itself as

$$I(T) = I_0(300) + I_1 n(\omega_{TO}, T) + I_2 n^2(\omega_{TO}/2, T) , \quad (5.26)$$

Figure 5.9 shows the results of the fits, and shows that the contribution from the one-phonon term I_1 of energy energy $2\omega_{TO}$ accounts for 88 % of the temperature dependence of the mode at 33 meV.

Table 5.1: Slopes of peaks shift and width temperature dependence in Fig. 5. Slopes are given in meV/K·10³.

Position	Fig. 5	Lifetime		Shift	
		TO	SHG	TO	SHG
[0.4 0.0 0.0]	(i),(f)	4.9(2)	7.1(1)	-4.0(2)	-7.6(5)
[0.6 0.0 0.0]	(k),(l)	4.0(6)	6.3(7)	-4.7(2)	-7.2(1)
[0.6 0.0 0.6]	(q),(r)	5.1(2)	9.7(6)	-3.2(1)	-8.2(4)
[0.2 0.0 0.2]	(w),(x)	5.5(4)	8.7(3)	-4.5(2)	-10.0(6)

Table 5.2: Fitting parameters for peaks in Fig. 2 of main text. μ and γ are given in meV.

Peak fitting function: $y_0 + \frac{A}{\pi} \frac{\gamma/2}{(x-\mu)^2 + (\gamma/2)^2}$					
Panel of Fig. 2	a	b	c	d	
Temperature	300 K	425 K	500 K	650 K	
Offset, y_0	-0.0009(1)	-0.0010(1)	-0.0011(2)	-0.0012(2)	
1st. peak	Center, μ_1	8.75(1)	8.51(3)	8.12(3)	8.0(3)
	Width, γ_1	4.0(1)	4.0(1)	3.9(2)	3.9(2)
	Area, A_1	0.342(3)	0.319(5)	0.293(6)	0.284(9)
2nd. peak	Center, μ_2	11.67(2)	11.48(2)	11.17(3)	10.97(3)
	Width, γ_2	2.0(1)	2.9(1)	3.7(1)	4.1(1)
	Area, A_2	0.074(6)	0.114(8)	0.13(1)	0.13(1)
3rd. peak	Center, μ_3	16.68(4)	16.25(4)	15.98(8)	15.6(1)
	Width, γ_3	3.6(1)	4.1(1)	5.0(3)	5.8(6)
	Area, A_3	0.44(1)	0.38(1)	0.38(1)	0.37(1)
4th. peak	Center, μ_4	22.9(5)	22.9(7)	22.7(9)	23(1)
	Width, γ_4	8.9(4)	9.3(6)	10.4(8)	11(1)
	Area, A_4	0.34(1)	0.41(1)	0.46(2)	0.47(3)
5th. peak	Center, μ_5	33.2(1)	31.9(1)	31.0(3)	30.7(6)
	Width, γ_5	3.3(2)	5.9(3)	7.2(6)	8.7(9)
	Area, A_5	0.025(2)	0.035(3)	0.053(5)	0.091(9)

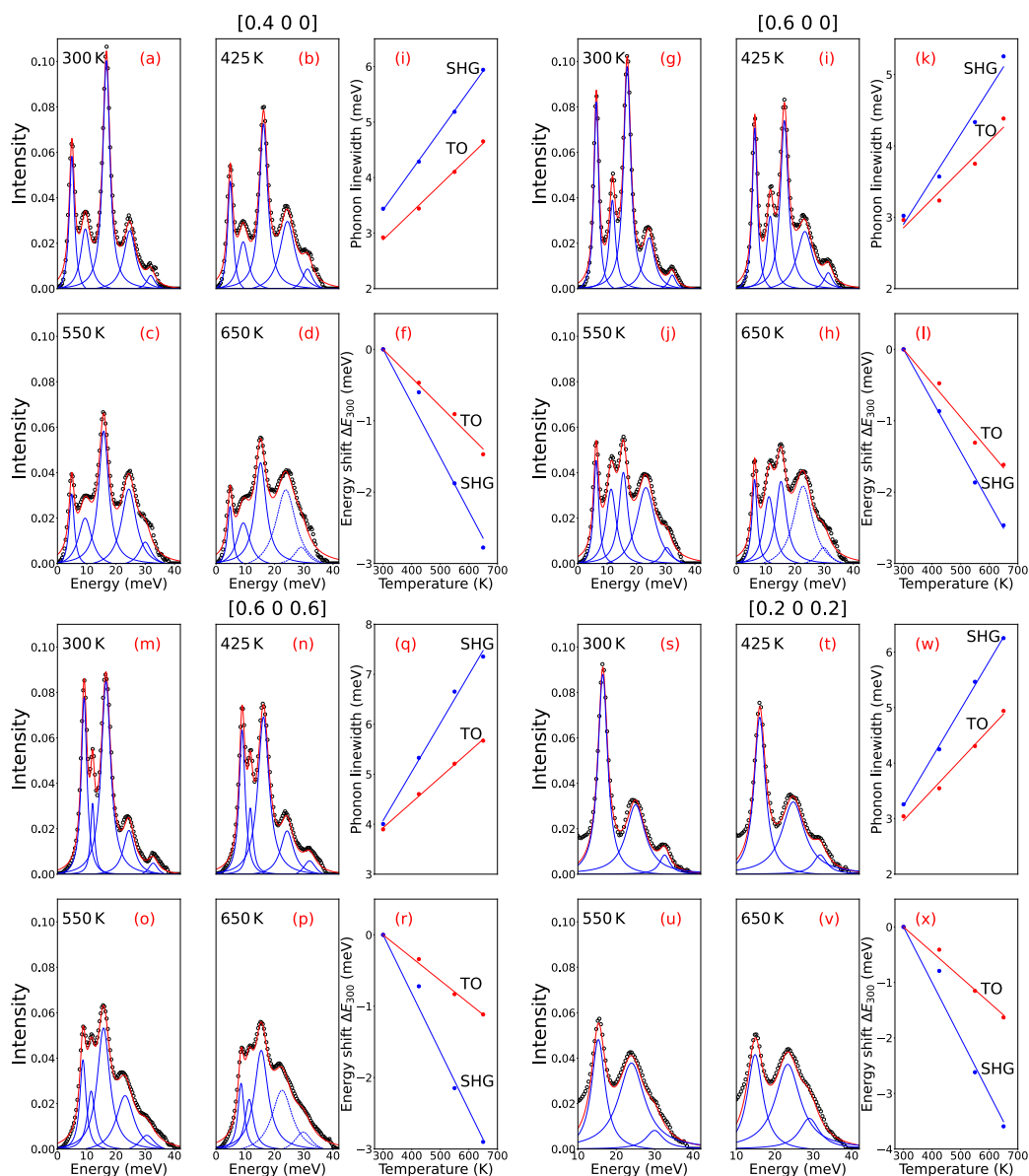


Figure 5.8: Temperature dependence of averaged vibrational spectra at high symmetry points of NaBr Brillouin zone: a)-f) - $[0.4\ 0\ 0]$; g)-l) - $[0.6\ 0\ 0]$; m)-r) - $[0.6\ 0\ 0.6]$; m)-r) - $[0.2\ 0\ 0.2]$. The panels e), f), k), l), q), r), w), x) correspond to the temperature dependence of the phonon lifetime and energy shift with respect to 300 K data for transverse optical mode (TO) and second harmonic generation (SHG) (slope of the data temperature dependence is given in the caption). Other panels show vibrational spectra at 300 K, 425 K, 550 K, 650 K with fitted peaks.

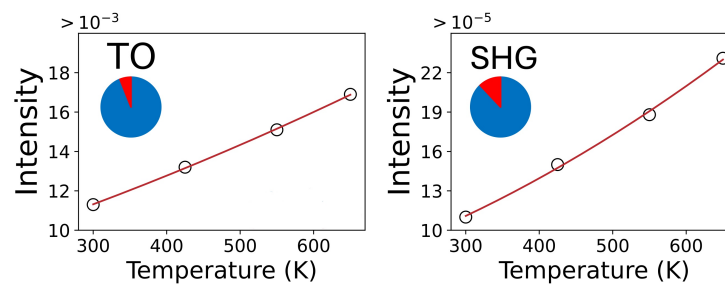


Figure 5.9: Temperature dependence of thermal occupation of (left) TO mode, and (right) SHG. Red solid line is a fit to the model function representing the sum of occupancy factors related to one and two phonon processes as fit with Eq. 5.26 for the TO mode at left and Eq. 5.20 for SHG at right.

References

- [1] V. V. Ladygin, C. N. Saunders, C. M. Bernal-Choban, D. L. Abernathy, M. E. Manley, and B. Fultz. Phonon second harmonic generation in nabr studied by inelastic neutron scattering and computer simulation. *Physical Review Materials*, 9:015002, Jan 2025. doi: 10.1103/PhysRevMaterials.9.015002. URL <https://link.aps.org/doi/10.1103/PhysRevMaterials.9.015002>.
- [2] Y. Shen, C. N. Saunders, C. M. Bernal, D. L. Abernathy, T. J. Williams, M. E. Manley, and B. Fultz. Prediction and observation of intermodulation sidebands from anharmonic phonons in NaBr. *Phys. Rev. B*, 103(13):134302, 2021.
- [3] D. L. Abernathy, M. B. Stone, M. J. Loguillo, M. S. Lucas, O. Delaire, X. Tang, J. Y. Y. Lin, and B. Fultz. Design and operation of the wide angular-range chopper spectrometer ARCS at the Spallation Neutron Source. *Rev. Sci. Instrum.*, 83(1):015114, 2012. doi: 10.1063/1.3680104. URL <https://doi.org/10.1063/1.3680104>.
- [4] T. E. Mason, D. Abernathy, I. Anderson, J. Ankner, T. Egami, G. Ehlers, A. Ekkebus, G. Granroth, M. Hagen, K. Herwig, J. Hodges, C. Hoffmann, C. Horak, L. Horton, F. Klose, J. Larese, A. Mesecar, D. Myles, J. Neufeind, M. Ohl, C. Tulk, X-L. Wang, and J. Zhao. The Spallation Neutron Source in Oak Ridge: A Powerful Tool for Materials Research. *Physica B Condens. Matter*, 385-386:955–960, 2006. ISSN 0921-4526. doi: 10.1016/j.physb.2006.05.281. URL <https://www.sciencedirect.com/science/article/pii/S092145260601177X>.
- [5] V. F. Sears, E. C. Svensson, and B. M. Powell. Phonon density of states in vanadium. *Can. J. Phys.*, 73(11-12):726–734, 1995.
- [6] J. Lahnsteiner and M. Bokdam. Anharmonic lattice dynamics in large thermodynamic ensembles with machine-learning force fields: $CsPbBr_3$, a phonon liquid with Cs rattlers. *Phys. Rev. B*, 105:024302, Jan 2022. doi: 10.1103/PhysRevB.105.024302. URL <https://link.aps.org/doi/10.1103/PhysRevB.105.024302>.
- [7] G. Kresse and J. Hafner. Ab initio molecular dynamics for liquid metals. *Phys. Rev. B*, 47:558–561, 1993. doi: 10.1103/PhysRevB.47.558. URL <https://link.aps.org/doi/10.1103/PhysRevB.47.558>.
- [8] G. Kresse and J. Hafner. Ab initio molecular-dynamics simulation of the liquid-metal–amorphous–semiconductor transition in germanium. *Phys. Rev. B*, 49:14251–14269, 1994. doi: 10.1103/PhysRevB.49.14251. URL <https://link.aps.org/doi/10.1103/PhysRevB.49.14251>.
- [9] G. Kresse and J. Furthmüller. Efficiency of *ab initio* total energy calculations for metals and semiconductors using a plane-wave basis set. *Comput. Mater.*

- Sci.*, 6(1):15 – 50, 1996. ISSN 0927-0256. doi: 10.1016/0927-0256(96)00008-0. URL <http://www.sciencedirect.com/science/article/pii/0927025696000080>.
- [10] G. Kresse and J. Furthmüller. Efficient iterative schemes for *ab initio* total-energy calculations using a plane-wave basis set. *Phys. Rev. B*, 54:11169–11186, 1996. doi: 10.1103/PhysRevB.54.11169. URL <https://link.aps.org/doi/10.1103/PhysRevB.54.11169>.
- [11] G. Kresse and D. Joubert. From ultrasoft pseudopotentials to the projector augmented-wave method. *Phys. Rev. B*, 59:1758–1775, Jan 1999. doi: 10.1103/PhysRevB.59.1758. URL <https://link.aps.org/doi/10.1103/PhysRevB.59.1758>.
- [12] J. P. Perdew, K. Burke, and M. Ernzerhof. Generalized gradient approximation made simple. *Phys. Rev. Lett.*, 77:3865–3868, Oct 1996. doi: 10.1103/PhysRevLett.77.3865. URL <https://link.aps.org/doi/10.1103/PhysRevLett.77.3865>.
- [13] D. S. Kim, O. Hellman, J. Herriman, H. L. Smith, J. Y. Y. Lin, N. Shulumba, J. L. Niedziela, C. W. Li, D. L. Abernathy, and B. Fultz. Nuclear quantum effect with pure anharmonicity and the anomalous thermal expansion of silicon. *Proc. Natl. Acad. Sci. USA*, 115(9):1992–1997, 2018. ISSN 0027-8424. doi: 10.1073/pnas.1707745115. URL <https://www.pnas.org/content/115/9/1992>.
- [14] A. V. Shapeev. Moment tensor potentials: A class of systematically improvable interatomic potentials. *Multiscale Modeling & Simulation*, 14(3): 1153–1173, 2016. doi: 10.1137/15M1054183. URL <https://doi.org/10.1137/15M1054183>.
- [15] A. P. Thompson, H. M. Aktulga, R. Berger, D. S. Bolintineanu, W. M. Brown, P. S. Crozier, P. J. in’t Veld, A. Kohlmeyer, S. G. Moore, T. D. Nguyen, R. Shan, M. J. Stevens, J. Tranchida, C. Trott, and S. J. Plimpton. LAMMPS - a flexible simulation tool for particle-based materials modeling at the atomic, meso, and continuum scales. *Comp. Phys. Comm.*, 271:108171, 2022. doi: 10.1016/j.cpc.2021.108171.
- [16] C. N. Saunders. *Thermal Behavior of Cuprous Oxide: a Comprehensive Study of Three-Body Phonon Effects and Beyond*. PhD thesis, California Institute of Technology, 2022. URL <https://resolver.caltech.edu/CaltechTHESIS:05262022-015714738>.
- [17] I. E. Protsenko, L. A. Lugiato, and C. Fabre. Spectral analysis of the degenerate optical parametric oscillator as a noiseless amplifier. *Phys. Rev. A*, 50(2):1627, 1994.

- [18] M. E. Manley, A. J. Sievers, J. W. Lynn, S. A. Kiselev, N. I. Agladze, Y. Chen, A. Llobet, and A. Alatas. Intrinsic localized modes observed in the high-temperature vibrational spectrum of NaI. *Phys. Rev. B*, 79(13):134304, 2009.
- [19] Yang Shen, Claire N Saunders, Camille M Bernal, Douglas L Abernathy, Michael E Manley, and Brent Fultz. Anharmonic origin of the giant thermal expansion of nabr. *Phys. Rev. Let.*, 125(8):085504, 2020.
- [20] M. E. Manley, J. W. Lynn, D. L. Abernathy, E. D. Specht, O. Delaire, A. R. Bishop, R. Sahul, and J. D. Budai. Phonon localization drives polar nanoregions in a relaxor ferroelectric. *Nat. Commun.*, 5(1):3683, 2014.
- [21] M. E. Manley, O. Hellman, N. Shulumba, A. F. May, P. J. Stonaha, J. W. Lynn, V. O. Garlea, A. Alatas, R. P. Hermann, J. D. Budai, et al. Intrinsic anharmonic localization in thermoelectric pbse. *Nat. Commun.*, 10(1):1928, 2019.
- [22] A. A. Maradudin and A. E. Fein. Scattering of neutrons by an anharmonic crystal. *Phys. Rev.*, 128(6):2589, 1962.
- [23] R. A. Cowley. Anharmonic crystals. *Rep. Prog. Phys.*, 31(1):123, 1968.
- [24] V. V. Ladygin, P. Yu. Korotaev, A. V. Yanilkin, and A. V. Shapeev. Lattice dynamics simulation using machine learning interatomic potentials. *Comput. Mater. Sci.*, 172:109333, 2020. ISSN 0927-0256. doi: <https://doi.org/10.1016/j.commatsci.2019.109333>. URL <https://www.sciencedirect.com/science/article/pii/S0927025619306329>.
- [25] I. S. Novikov, K. Gubaev, E. V. Podryabinkin, and A. V Shapeev. The MLIP package: moment tensor potentials with MPI and active learning. *Mach. Learn.: Sci. Technol.*, 2(2):025002, 2020. doi: 10.1088/2632-2153/abc9fe.
- [26] N. Benshalom, G. Reuveni, R. Korobko, O. Yaffe, and O. Hellman. Dielectric response of rock-salt crystals at finite temperatures from first principles. *Phys. Rev. Mat.*, 6(3):033607, 2022.

Chapter 6

ANHARMONIC PHONONS AND NUCLEAR QUANTUM EFFECTS IN ZINC

6.1 Introduction

As shown in [1], anharmonic effects are not limited to high temperatures. They can be significant at low temperatures through the zero-point occupancy of anharmonic modes. For some thermophysical properties, the self-energies of thermally-populated modes can be altered by anharmonic coupling to higher-energy modes having only zero-point occupancy. In [2], such anharmonicity with nuclear quantum effects explained the negative thermal expansion of silicon below room temperature. A similar explanation accounted for the negative thermal expansion of cuprite [3]. For INS spectra at cryogenic temperatures, it is plausible that zero-point occupancy could lead to phonon IPS or SH features through cubic or high-order terms of the crystal Hamiltonian.

Here I report phonon dispersions measured on a single crystal of Zn at temperatures of 15 K, 300 K, 450 K, and 690 K. With increasing T , the dispersions broaden and shift to lower energies. At high T , I find pronounced diffuse intensity above the top of the phonon dispersions at 27 meV. With decreasing T , the intensity reduces as expected. However, even at 15 K, I find a measurable diffuse intensity, indicating anharmonic phonon recombination caused by nuclear quantum effects (NQE). The classical molecular dynamics simulations gave diffuse intensity at the higher temperatures, but no diffuse intensity was obtained at 15 K. Diffuse intensity was found at 15 K from ab initio calculations with the temperature-dependent effective potential (TDEP) method when zero-point contributions were added, and with path integral molecular dynamics (PIMD) calculations that account for zero-point dynamics.

A quantum Heisenberg-Langevin analysis for phonon interactions, developed previously [4], was used to calculate the shape of the diffuse intensity at the K point in the Brillouin zone, compared to the intensity of the TO mode. With a phonon-phonon interaction parameter determined from the experimental phonon linewidths, and the assumption of a medium-strong coupling to a thermal phonon bath, the calculated intermodulation phonon sidebands (IPS) were in good agreement with experiment for a medium-strong coupling of the TA + TO and TO + TO modes.

In [5, 6], it was shown that Zn, a hexagonal crystal (but not close-packed), has significantly different coefficients of linear thermal expansion in the a - b basal plane, β_a , than along the c -direction, β_c (where $\beta_\zeta = \frac{1}{\zeta} \frac{\partial \zeta}{\partial T}$ (ζ is a or c). At temperatures below 100 K, β_c is positive but β_a is negative. These coefficients of thermal expansion are found from the dependence of the free energy on a and c . The internal energy is dominated by elastic energy U_{el} , and the entropy is primarily from atom vibrations, S_{vib} . With a change in temperature, the lattice parameters a and c change to keep the free energy functional $F(a, c, T) = U_{el} - TS_{vib}$ at a minimum.

The TDEP method was versatile for determining the free energy from phonons and lattice expansion, with and without zero point contributions. Adding the zero point to the mode occupancies (a nuclear quantum effect) in TDEP calculations improved considerably the thermal expansion calculated for temperatures around 40 K. Comparing the accuracy of anisotropic thermal expansion calculations by path integral molecular dynamics (PIMD) simulations and by classical molecular dynamics also showed the need to include nuclear quantum effects. For example, calculations of the negative thermal expansion for the a parameter below 70 K improved by more than a factor of 3 when the zero-point energy was included in the calculations.

6.2 Experimental Details

A large single crystal of high-purity zinc was grown by a modified Bridgman technique [7]. Molten zones approximately 2.5 cm long were passed through a rod of approximately 1.5 m in length. The single crystal was cut from a section in the rod 35 cm in length that was zone-refined for chemical purity. The resulting [001]-oriented untwinned Zn single crystal was cut to an oval plate of 37×33 mm in area and 10 mm thick, chemically polished, and suspended in a vanadium holder for all measurements. The Supplemental Material shows images of the crystal and sample holder.

The INS measurements were performed with the time-of-flight wide angular range chopper spectrometer, ARCS [8], at the Spallation Neutron Source [9], using neutrons with an incident energy of 70 meV. These measurements used a Fermi chopper with a slit width of 1.5 mm, and spinning at 120 Hz, to monochromate the beam. The [001] basal plane was in the plane of the spectrometer as the sample was rotated over 192 increments in angle in a vacuum furnace at 300 K, 500 K and 690 K or a helium displax refrigerator at 15 K. An empty vanadium holder was measured

under the same conditions, although scattering from the holder was much weaker than the holder plus sample. Data processing included normalization of detector response with respect to white beam vanadium measurement [10], subtraction of background from the sample holder and the sample environment, then a correction for multiphonon scattering in the incoherent approximation [11] for each Brillouin zone of the dataset. After these corrections, the data were folded back into an irreducible wedge in the first Brillouin zone to show intensities of the experimental dispersions along conventional high symmetry directions in reciprocal space. Phonon density of states (DOS) curves were obtained by averaging the intensities over the first Brillouin zone with a grid of $171 \times 171 \times 171$ points in reciprocal space. The Supplemental gives additional details of the data processing.

The experimental phonon dispersions along high-symmetry crystallographic directions are presented in Fig. 6.1. The phonon dispersions at 15 K in panel (a) are consistent with the harmonic model, although some weak diffuse intensity is found above the harmonic phonon dispersions in panel (e). From 300 K to 690 K, the diffuse intensity grows around the high symmetry points Γ and A at energies around 25-30 meV, and from K to M at approximately 30-35 meV. At 690 K the diffuse intensity reaches 35 meV or more for all reciprocal space points in Fig. 6.1(d),(h). The phonon DOS Fig. 6.1(e)-(h) confirms the trend of formation of separate features of intensity at 30 and 35 meV. The plots also show how the intensities of these features increase with temperature. Figure 6.2 shows the intensities of dispersions at 15 K in more detail, using a log scale with a low-intensity cutoff. Along the K - M path, there is some diffuse intensity, as in a high-temperature spectra. The diffuse features are qualitatively similar to those at 300 K in Fig. 6.1(b).

6.3 Ab Initio Simulations

Temperature-dependent effective potential method

Anharmonic phonons from TDEP

Phonon lineshapes at 15 K from the sTDEP method are shown in Fig. 6.3(a). To analyze the origin of high-energy diffuse intensity near the K point in terms of its contributing three-phonon processes, I used a branch elimination technique similar to [4, 12]. I eliminated contributions from all three-phonon processes attributed to optical modes in the energy range between 22 meV and 24 meV (Fig. 6.3(b)). This involved setting to zero all three-phonon matrix elements $\Phi_{s's''}^{\vec{q}\vec{q}'\vec{q}''}$ in Eq. 2.11 that correspond to effective harmonic phonon frequencies $\omega_{\vec{q},s}$, $\omega_{\vec{q}',s'}$ or $\omega_{\vec{q}'',s''}$ in this

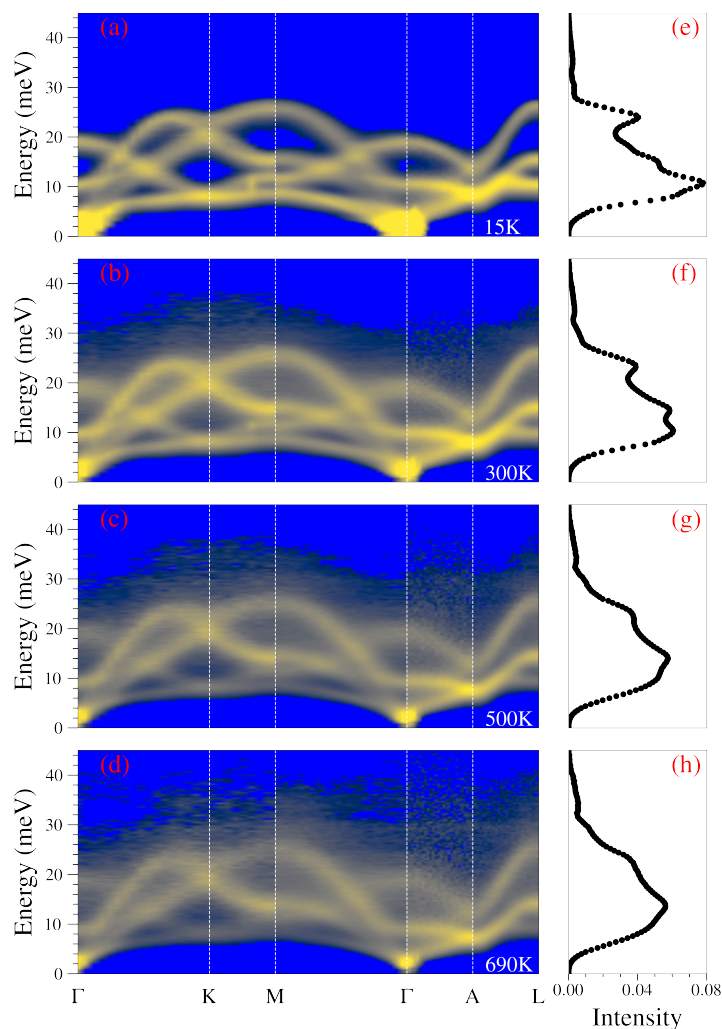


Figure 6.1: Inelastic neutron scattering data from Zn single crystal (a)-(d) with phonon DOS (e)-(h). Each panel is normalized with respect to its total inelastic intensity (data are on a log scale).

energy interval.

I estimated the contributions of individual harmonic phonon modes to the scattering function from the corresponding three phonon processes. The total scattering function in the limit of small self-energies was approximated as in Eq. 5.1. Figure 6.3(c),(e) shows diffuse intensity around 40 meV and 35 meV as the original phonon lineshape obtained with sTDEP. The intensity was calculated as the partial contribution to the phonon spectral function at 40 meV and 35 meV, computed for harmonic branches along high symmetry directions using Eqs. 2.11 and 5.1. Even at 15 K, there is some diffuse intensity above 32 meV owing to the anharmonic coupling of the zero point motion of high energy modes.

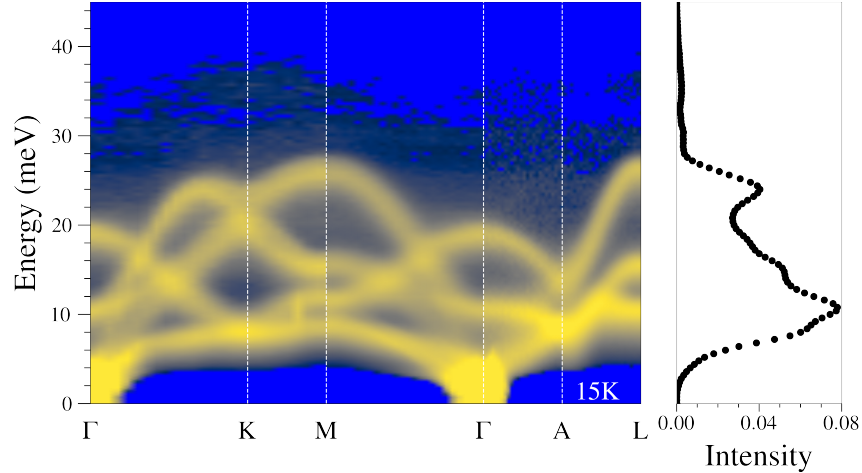


Figure 6.2: Inelastic neutron scattering data from Zn single crystal at 15 K with fine spectral features (data are on a log scale).

The anharmonic coupling in the Brillouin zone is projected onto the basal plane of phonon wavevectors in Fig. 6.3(d),(f). The intensity contributions are computed at 40 meV (Fig. 6.3(d)) and 35 meV (Fig. 6.3(f)) where diffuse intensity is observed in TDEP spectra. As $\vec{q} \rightarrow \vec{q}_K$, the intensity can be understood as a frequency doubling of the original mode (as in [12]). The 35 meV intensity originates from the coupling of transverse acoustic and transverse optical vibrations (Fig. 6.3(e)) at energies around 6 and 22 meV. From Fig. 6.3(f) the coupling at the K^* point in this region is from vibrations localized at equivalent K^3 high symmetry points.

Thermal Expansion from TDEP

For volume relaxation with stochastic TDEP, I start with the free energy expansion up to second order in the volume $\delta V = (V - V_0)$

$$F(\delta V) = -P\delta V + \frac{1}{V}B\delta V^2, \quad (6.1)$$

$$P = -\frac{\partial F}{\partial V}, \quad B = V\frac{\partial^2 F}{\partial V^2} \quad (6.2)$$

where P is the pressure and B is the bulk modulus.

In TDEP formalism the free energy is defined as

$$F = U_0^{\text{TDEP}} + F_{ph}^{\text{TDEP}}, \quad (6.3)$$

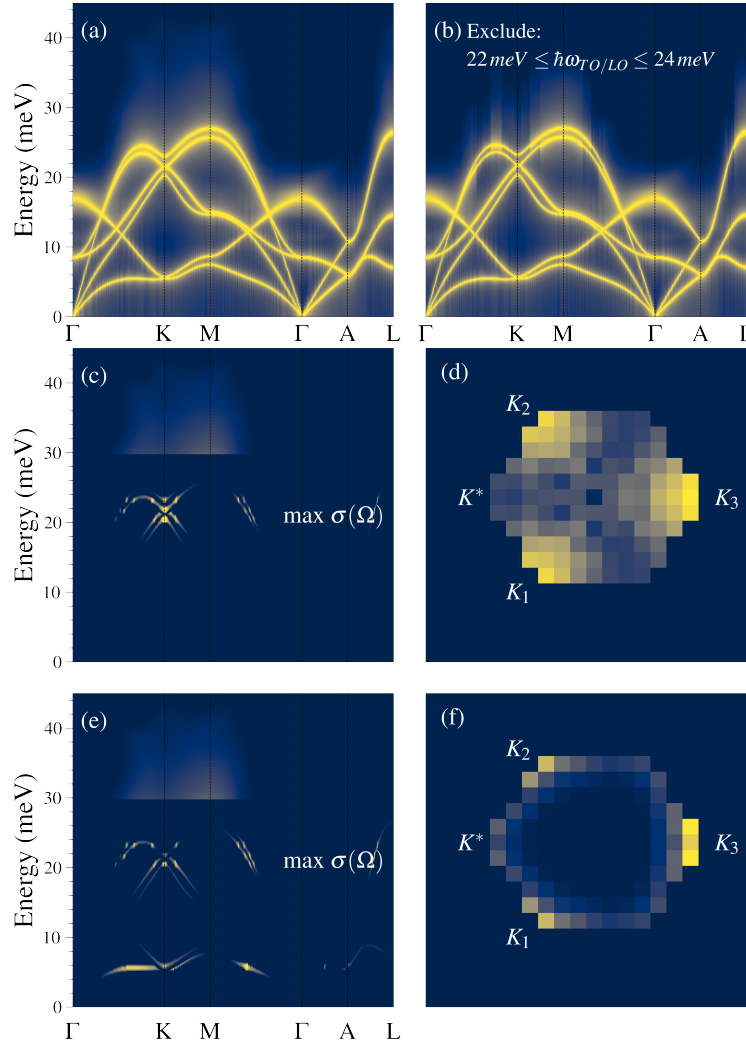


Figure 6.3: Band elimination analyses of Zn vibrational spectra. (a) sTDEP phonon dispersions along high-symmetry directions at 15 K. (b) Phonon lineshapes at 15 K where contributions from three-phonon processes associated with the optical modes in the range of 22 to 24 meV are set to zero. (c) Harmonic modes that give the maximum contribution to the second harmonic spectral lineshape through three-phonon processes at 40 meV, and (e) 35 meV. Coupling at K high symmetry point over the Brillouin zone of hexagonal crystal projected on the q_x, q_y plane at 40 meV (d) and 35 meV (f).

$$U_0^{TDEP} = \left\langle U_{DFT}(T, V) - \frac{1}{2} \sum_{i,j} \sum_{\alpha,\beta} \Phi_{i,j}^{\alpha,\beta}(T, V) u_i^\alpha u_j^\beta - \frac{1}{6} \sum_{i,j,k} \sum_{\alpha,\beta,\gamma} \Phi_{i,j,k}^{\alpha,\beta,\gamma}(T, V) u_i^\alpha u_j^\beta u_k^\gamma \right\rangle, \quad (6.4)$$

$$F_{ph}^{TDEP} = \sum_{\vec{q},\nu} \left[\frac{1}{2} \hbar \omega_{\vec{q},\nu} + k_B T \ln(1 - e^{-\beta \hbar \omega_{\vec{q},\nu}}) \right], \quad (6.5)$$

where $\omega_{\vec{q},\nu}$ is the angular frequency of a phonon with momentum \vec{q} and polarization ν ; $\Phi_{i,j}^{\alpha,\beta}$ and $\Phi_{i,j,k}^{\alpha,\beta,\gamma}$ are the second- and third-order forceconstants.

The stress tensor $\sigma_{\alpha\beta}$ of the system is obtained as the derivative of free energy with respect to the strain tensor $\varepsilon_{\alpha\beta}$

$$\begin{aligned} \sigma_{\alpha\beta} &= \frac{1}{V} \frac{\partial F}{\partial \varepsilon_{\alpha\beta}} = \frac{1}{V} \frac{\partial U_0}{\partial \varepsilon_{\alpha\beta}} + \frac{1}{V} \frac{\partial F_{ph}}{\partial \varepsilon_{\alpha\beta}} \\ &= \sigma_{\alpha\beta}^0 + \sigma_{\alpha\beta}^{ph}, \end{aligned} \quad (6.6)$$

where $\sigma_{\alpha\beta}^0$ and $\sigma_{\alpha\beta}^{ph}$ are the static and phonon parts of the stress tensor.

Using phonon part of free energy in TDEP formalism (Eq. 6.5), the phonon part of the stress tensor is computed as

$$\sigma_{\alpha\beta}^{ph} = \frac{1}{V} \sum_{\vec{q},\nu} \hbar \omega_{\vec{q},\nu} \gamma_{\vec{q},\nu}^{\alpha\beta} \left(\frac{1}{2} + n_{\vec{q},\nu} \right), \quad (6.7)$$

with the mode-projected Grüneisen tensor for the phonon mode \vec{q}, ν and Cartesian components α, β given by [13]

$$\gamma_{\vec{q},\nu}^{\alpha\beta} = -\frac{V}{6\omega_{\vec{q},\nu}^2} \sum_{i,j,k} \sum_{\gamma\delta} \frac{\epsilon_{\vec{q},\nu}^{i\gamma} \epsilon_{\vec{q},\nu}^{j\delta}}{\sqrt{m_i m_j}} r_k^\alpha \Phi_{i,j,k}^{\gamma,\delta,\beta} \exp[\vec{q} \cdot \vec{r}], \quad (6.8)$$

where ϵ is the phonon eigenvector, and m and \vec{r} are the atomic mass and position. The derivation of the static part of the stress tensor from U_0^{TDEP} defined in Eq. 6.4 is given in the Supplemental.

Using the stress tensor, I redefine the free energy expression in Eq. 6.1 as a function of deformation

$$\frac{1}{V} F(\varepsilon) = \sigma_\rho \varepsilon_\rho + c_{\rho\zeta} \varepsilon_\rho \varepsilon_\zeta, \quad (6.9)$$

where I used the Voigt notation ρ [14] instead of Cartesian indexes $\alpha\beta$. The stress tensor σ_ρ plays the role of pressure, P , and the elastic constants $c_{\rho\zeta}$ are used instead of bulk modulus, B . The equilibrium deformation is predicted by minimizing the free energy functional.

$$\varepsilon_\rho = -(c^{-1})_{\rho\zeta} \sigma_\zeta = -s_{\rho\zeta} \sigma_\zeta \quad (6.10)$$

The corresponding primitive cell $\mathcal{A}_{\alpha\beta}$ update is

$$\mathcal{A}_{\alpha\beta}^{(n+1)} = \mathcal{A}_{\alpha\beta}^{(n)} + \varepsilon_{\alpha\beta} \mathcal{A}_{\alpha\beta}^{(n)}. \quad (6.11)$$

Finally, the updated cell is used in the next step of sTDEP, closing the self-consistent loop.

Molecular Dynamics Simulations with Machine Learning Interatomic Potential

A machine-learned moment-tensor potential (MLIP) [15] was used to model the interatomic interactions in classical MD simulations with the LAMMPS code [16]. The supercell size was $60 \times 60 \times 30$ with 216,000 atoms. The Supplemental provides additional details on MLIP construction and computational data analyses. The results from MD calculations were post-processed in the package VVCORE [17]. The projected velocity-velocity autocorrelation functions came from 40 statistically independent 10 ps MD trajectories to ensure convergence in the time domain. I obtained the spectral intensity through the Fourier transform of a velocity-velocity autocorrelation function, projected onto \vec{Q} . These MD calculations required long lengths and extended times for good resolution of phonon features in \vec{Q} and ω [18].

The MLIP was trained with input from density functional theory (DFT) calculations performed with VASP [19–22]. The DFT calculations used plane-wave basis sets, exchange-correlation functionals in the generalized gradient approximation (GGA) [23, 24], the projector augmented wave (PAW) method, and supercells generated with thermally-displaced atoms. These training supercells were $4 \times 4 \times 2$, containing 64 atoms. Zinc as a metallic solid is known for slow convergence with respect to a number of k -points and energy cutoff [25, 26]. I used a dense k -grid ($7 \times 7 \times 7$), and a kinetic energy cutoff of 600 eV. The final training set contained 117 configurations.

Vibrational spectra along high symmetry directions, obtained from autocorrelation functions of classical MD trajectories are shown in Fig. 6.4. The calculations using MLIP reproduce the formation of diffuse intensity at the higher temperatures. Since classical MD does not include nuclear quantum effects at low temperatures, it does not reproduce the diffuse intensity at 15 K. At 300 K, some diffuse intensity is found above 20 meV at the the K point. At higher temperatures, this diffuse feature softens in energy following the trend of the phonon branches that are coupled. However, at 690 K the spectral features above 30 meV broaden considerably, owing to the substantial decrease in the lifetime of these vibrational excitations.

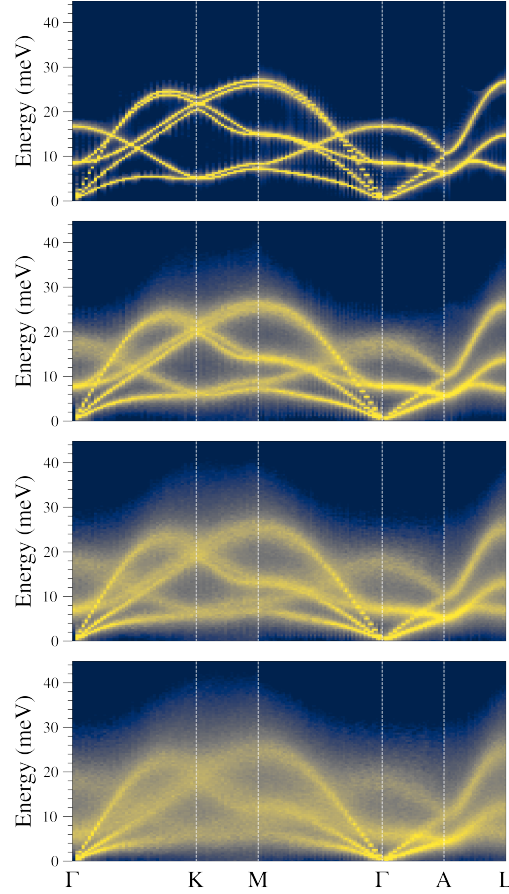


Figure 6.4: Phonon dispersions along high-symmetry directions calculated with classical MD and projected velocity-velocity autocorrelation function method. Temperatures from top to bottom: 15 K, 300 K, 500 K, 690 K.

6.4 Heisenberg-Langevin Equation

The origin of diffuse intensity at the high symmetry K point can be explained with a combination of two distinct coupling processes. Hence, I write Eq. 5.12 for the third mode c

$$S_{ac}[\omega] = \frac{\hbar\gamma_a(n_a + \frac{1}{2})}{2m\omega_a} |\chi_a + 2i\omega_c g^2 \chi_a^2 \chi_{ac} \bar{\chi}_{ac}|^2, \quad (6.12)$$

where χ_{ac} are defined as phonon propagation susceptibility functions for oscillator c

$$\chi_{ac}^{-1} = -i(\omega - \omega_a - \omega_c) + \frac{\gamma_c}{2}, \quad (6.13)$$

$$\bar{\chi}_{ac}^{-1} = -i(\omega - \omega_a + \omega_c) + \frac{\gamma_c}{2}. \quad (6.14)$$

In Eq. 5.12 and Eq. 6.12 for sideband formation, the first term corresponding to $g = 0$ is the Lorentzian peak at frequency ω_a . These two equations differ in their

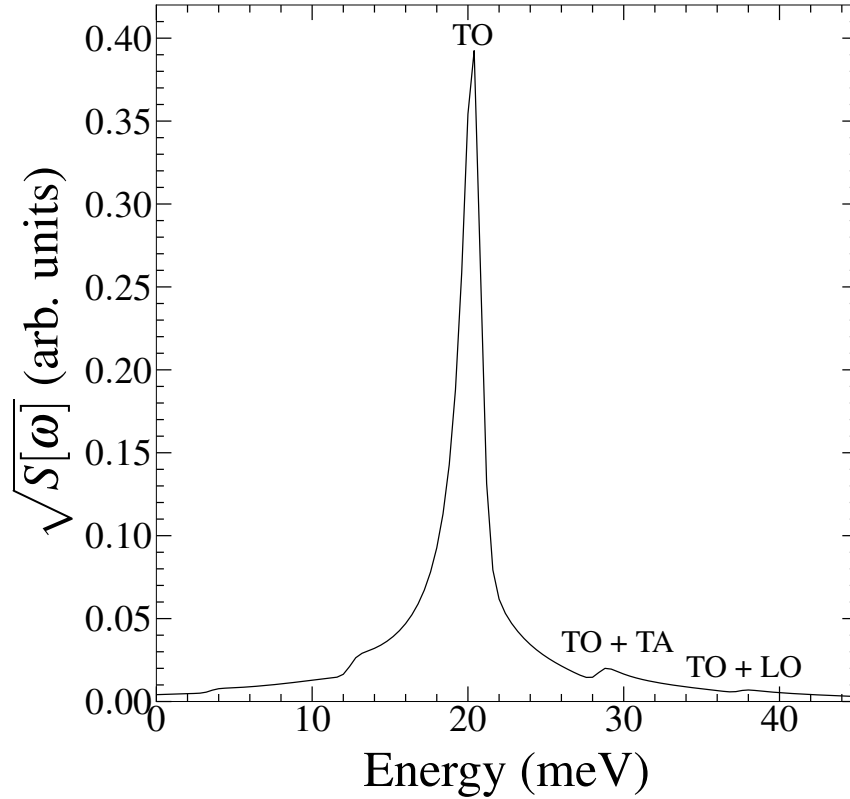


Figure 6.5: Results from the Heisenberg–Langevin model for high energy diffuse intensity formation at 15 K in the medium-strong coupling regime.

last terms. The final spectral intensity obtained by combining the last terms of Eq. 5.12 and Eq. 6.12 is

$$S[\omega] = \frac{\hbar\gamma_a(n_a + \frac{1}{2})}{2m\omega_a} |\chi_a + 2i\omega_b g^2 \chi_a^2 \chi_{ab} \bar{\chi}_{ab} + 2i\omega_c g^2 \chi_a^2 \chi_{ac} \bar{\chi}_{ac}|^2. \quad (6.15)$$

The prefactor in Eq. 6.15 ($n_a + \frac{1}{2}$) accounts for nuclear quantum effects at low temperature. Predictions at 15 K for medium-strong coupling ($g \simeq \gamma_a$) are shown in Fig. 6.5. The TO mode, ω_a , gives the peak centered at 20.5 meV and FWHM γ_a of 1.5 meV. Equation 5.19 gives the sidebands at around 29 meV and 38 meV from the coupling of the TA mode (center 8 meV and FWHM of 1.5 meV) and the LO mode (center 17 meV and FWHM of 1.5 meV). The model correctly predicts the formation of sidebands and intensity distribution between sidebands and TO mode at 15 K. The intensities of TO, TO + TA, and TO + LO peaks $I_{TO} : I_{TO+TA} : I_{TO+LO}$ are in the ratio of 13:2:1, in agreement with the experimental values of 15:2:1.

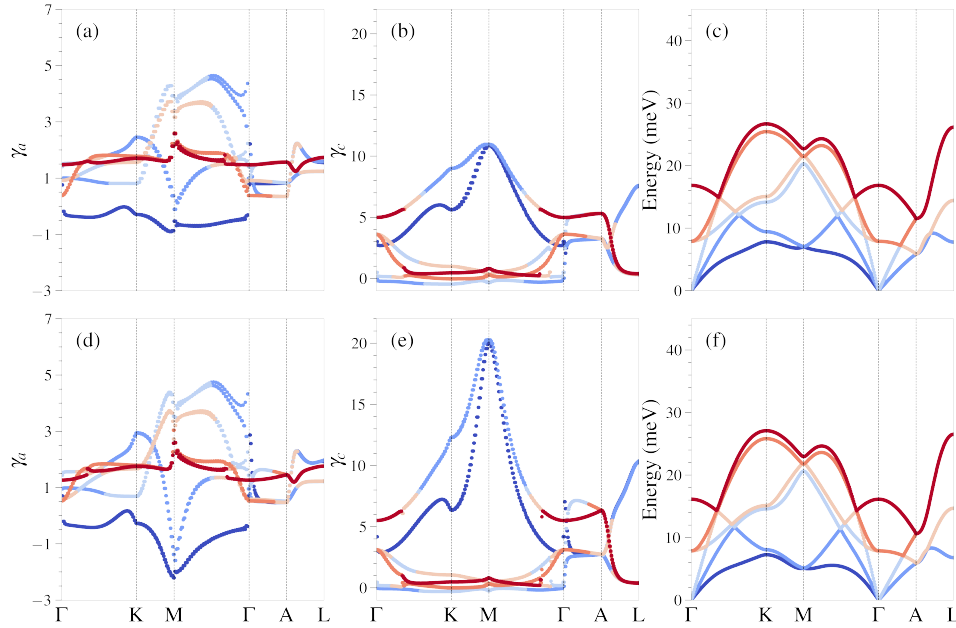


Figure 6.6: Mode Grüneisen parameters for dispersions, shaded to match their corresponding dispersions at (a-b) 15 K and (d-e) 300 K. Phonon dispersions from sTDEP calculations at (c) 15 K and (f) 300 K colored to correspond with their matching mode Grüneisen parameters.

6.5 Thermal Expansion

The right-hand panels in Fig. 6.6 are phonon dispersions from the harmonic part of the sTDEP method, with color coding that matches the mode Grüneisen parameters at left for the a - b axes, γ_a , and the c -axis, γ_c . The mode Grüneisen parameters were obtained from Eq. 6.8 for sTDEP calculations at 15 and 300 K.

The Grüneisen parameters are consistent with the quasiharmonic (QH) rule for the negative thermal expansion (NTE) at low temperatures – the NTE corresponds to negative Grüneisen parameters for low-energy phonons. The a lattice constant, which is known to have NTE at low temperatures, has negative Grüneisen parameters along the a - b plane at the zone edge, whereas the Grüneisen parameters projected on the z direction are comparatively large and positive. The largest Grüneisen parameters are near the point K in the Brillouin zone. The negative values of the Grüneisen parameter along the a - b plane at 15 K are less negative at 300 K. This QH picture is consistent with the positive values of thermal expansion in a - b plane at medium and high temperatures. The Grüneisen parameters projected on the z axis are large and positive, consistent with the positive thermal expansion along c . While this qualitative agreement with expectations from the QH model is appealing, the NTE predicted by the QH model is not accurate, as discussed below.

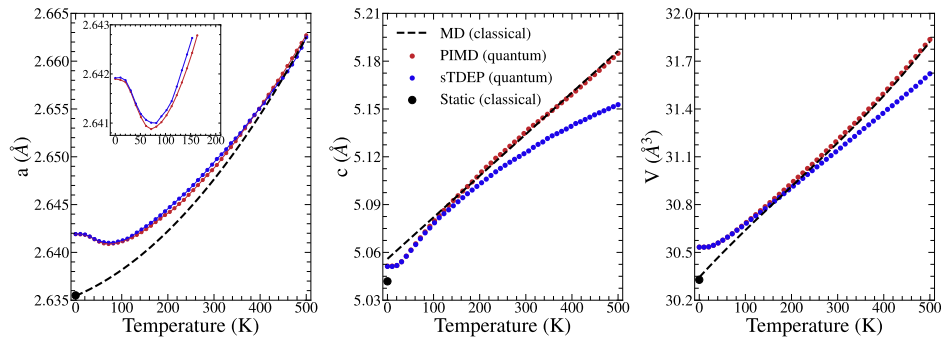


Figure 6.7: Computational lattice constants (left and center) and volume (right) as a function of temperature of hexagonal Zn. Path Integral MD and sTDEP calculations are shown with red and blue dots, respectively. Classical MD simulation and static relaxation calculation at zero temperature are shown with dashed black line and black dot. (Inset) Calculations at temperatures with NTE.

Figure 6.7 shows the temperature dependence of lattice parameters obtained with the sTDEP relaxation procedure (blue line and dots) and PIMD simulation in the NPT ensemble (constant number of atoms, pressure, energy). Results from classical MD simulations in the NPT ensemble with static relaxation at zero temperature are shown for comparison. As described in [2], nuclear quantum effects (NQE) result in anharmonic interactions between phonons, changing their self-energies and altering the volume dependence of the free energy. The PIMD and sTDEP methods are constructed to include NQE, and give the similar results in the region of NTE. Both are in good agreement with experiment. Additionally, the PIMD and sTDEP calculations converge to the black curve from classical simulations at around 400 K for the a lattice constant and 300 K for c . The sTDEP results diverge from PIMD at high temperatures (especially for c axis and volume temperature dependence). This might come from high-order anharmonic processes affecting the lattice dynamics of Zn.

Some linear coefficients of thermal expansion along the a - and c -axis are compared with experimental results in Fig. 6.8. The quasiharmonic (QH) results were obtained by finding the minimum of free energy with respect to the a and c lattice parameters, $F(a, c)$. Although the QH calculations give qualitative trends, they are quantitatively inaccurate. Figure 6.8 shows that anharmonicity must be treated accurately, together with zero-point dynamics. The thermal expansion calculated from Eq. 6.3 depends only on the temperature dependence of U through the electronic energy and the temperature dependence of S through the phonon frequencies $d\omega_{q,s}/dT$. With anharmonicity, $\omega_{q,s}$ depends independently on both T and V as $\omega_{q,s}(V, T)$, but

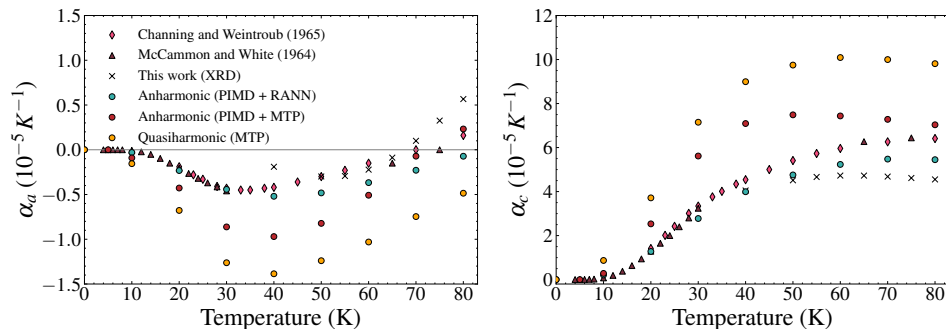


Figure 6.8: Calculated and experimental coefficients of linear thermal expansion of a-axis (left) and c-axis (right) of hexagonal Zn. Calculations are shown with circles (PIMD with MTP, red; PIMD with RANN, cyan; QH calculation, orange). Experimental data from Channing and Weintraub and McCannon are presented with diamond and triangle markers. Crosses are from present X-ray diffraction measurements of zinc powder.

the QH approximation assumes $\omega_{q,s}(V(T))$, so phonon frequencies cannot change with T alone. Figure 6.8 shows that PIMD simulations with MTP give much better coefficients of thermal expansion than QHA. Nitol [25] showed that PIMD with an Artificial Neural Network (ANN) potential gave reasonable agreement to experimental lattice constants, and Fig. 6.8 shows that this potential gave good agreement with experiment in the region of NTE at low temperatures. The coefficients extracted from X-ray diffraction patterns of zinc powder (corresponding lattice parameters were obtained through Reitveld refinement with GSAS-II software) are in agreement with previous results in predicting NTE along a-axis at low temperatures. Details of XRD data collection, diffraction patterns, and extracted lattice parameters are presented in the Supplemental Materials. The ANN is trained on DFT data with LDA exchange-correlation functionals, but this results in an underestimation of the coefficient of thermal expansion above 50 K.

Thermal expansion is inversely proportional to the bulk modulus, and errors in bulk modulus are consistent with some of the discrepancies between experimental thermal expansion coefficients and those calculated with DFT methods. The bulk modulus from ANN trained on DFT data with an LDA exchange-correlation functional is 93.19 GPa [25]. This is greater than the experimental value equal to 80 GPa [27]. On the other hand, the bulk modulus from the MTP calculations, trained with DFT data obtained from the GGA functional (PBE), predicts a lower value of 59.48 GPa, comparable to previous studies on Zn with PBE functionals [28]. Approximately, the underestimation of thermal expansion by RANN and overestimation by MTP

are consistent with their discrepancies in bulk modulus.

6.6 Conclusion

Anharmonic effects in the vibrational spectra of hexagonal zinc were investigated by inelastic neutron scattering and *ab initio* computational methods. A diffuse intensity near the K point in the Brillouin zone was found. This diffuse feature can be explained by the sideband model proposed in [4], which describes a strong phonon-phonon coupling mechanism involving transverse optical, transverse acoustic, and longitudinal acoustic modes. The sidebands are observed even at cryogenic temperatures, owing to anharmonic coupling to modes with zero-point dynamics.

Phonon anharmonicity influences the phonon self-energies, causing both positive and negative shifts as temperature varies. Even at extremely low temperatures, the zero-point quantum occupancies of high-energy vibrational modes affect the energies of low-energy modes through anharmonic coupling. This nuclear quantum effect, coupled with anharmonicity, explains the negative thermal expansion observed in the a - b plane and allows quantitative accuracy with computational methods. Both anharmonicity and nuclear quantum effects are important for thermophysical properties of zinc, and may be important for other materials with hexagonal crystal structures.

6.7 Supplemental Material

Single Crystal Data Analysis

Figure 6.10 shows the single crystal of Zn, and how it was mounted in a vanadium holder. Data were acquired in “event mode,” where raw data were time-stamped detections of individual neutrons in pixels of the large-area (π sr) detector array of the ARCS spectrometer at the SNS. Tools in the Mantid software package were used to reduce the single crystal data into the four-dimensional scattering function $S(\vec{Q}, \epsilon)$ [29]. Preliminary analyses assessed the data statistics, sample alignment, nonlinearities of the detector array for Bragg diffractions, and possible abnormalities in the different Brillouin zones. I found no problems, so I folded data throughout \vec{Q} into an irreducible wedge in the first Brillouin zone using symmetry operators. Before folding each zone, I subtracted background from the thin-wall vanadium sample container and an averaged incoherent multiphonon scattering. Finally, I checked the temperature dependence of the data at 15 meV at the K high-symmetry point to ensure that there are no processing artifacts introduced and the raw intensity of the sample is a smooth function of temperature (Fig. 6.9).

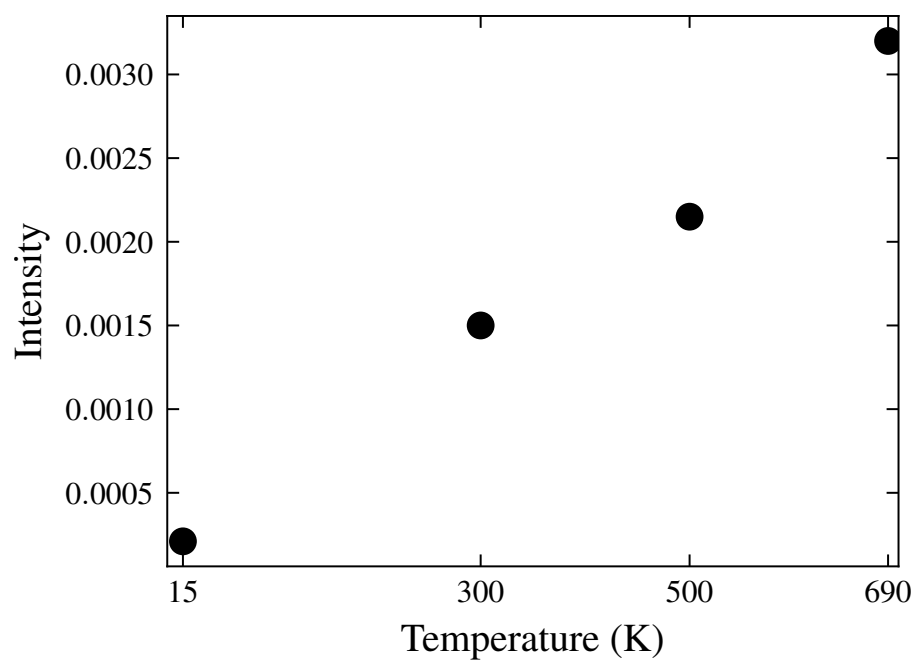


Figure 6.9: Intensity cut at K high symmetry point at $E = 15$ meV as a function of temperature.

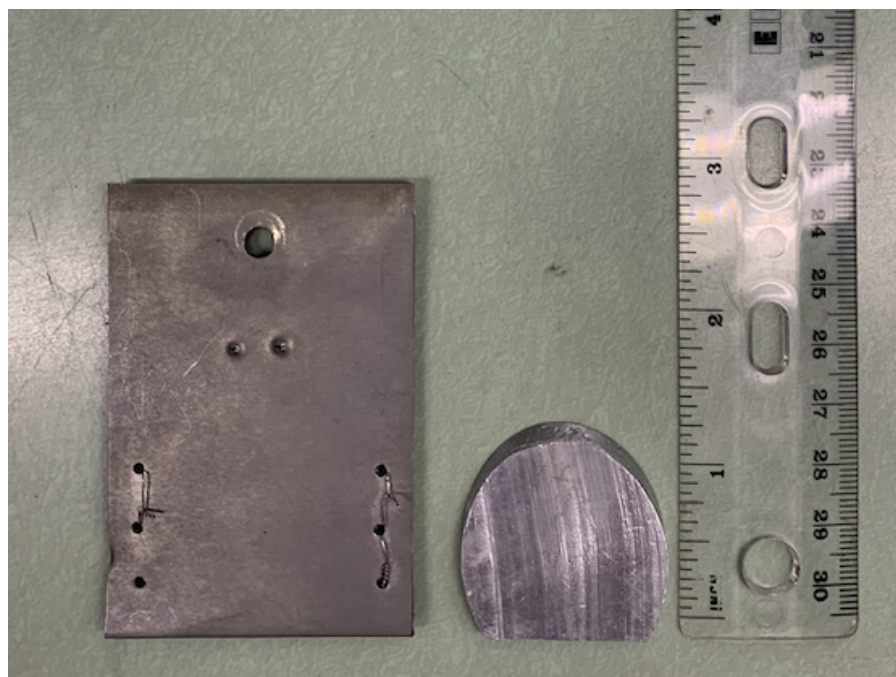


Figure 6.10: Zn single-crystal with vanadium sample holder.

For better visualization of the high energy modes, the spectral intensities were thermally weighted with the energy-dependent factor:

$$\varepsilon \left[1 - \exp\left(\frac{-\varepsilon}{k_B T}\right) \right] \times S(\vec{Q}, \varepsilon) = S_{\text{weighted}}(\vec{Q}, \varepsilon) \quad (6.16)$$

where $\varepsilon = \hbar\omega$. More details on the general process of data acquisition and analyses can be found in [4, 30].

X-ray diffraction data for thermal expansion

Variable-temperature cryogenic powder X-ray diffraction (XRD) measurements were performed using a PANalytical X'Pert Pro MPD diffractometer equipped with an Oxford PheniX closed-cycle cryostat (Oxford Cryosystems). Cu $K\alpha$ radiation ($\lambda = 1.5418 \text{ \AA}$) was used in conjunction with an X'Celerator position-sensitive detector. For the cryogenic measurements, the sample was initially cooled to 30 K at a rate of -6 K/min . After equilibrating at 30 K for 1 minute, data were collected over a 2θ range of 20° to 100° , with a step size of 0.016° and an exposure time of 40 seconds per step. The sample was subsequently heated at a rate of 6 K/min to the next desired temperature, and data collection resumed after 1 minute of equilibration at each step. The X-ray generator was operated at 45 kV and 40 mA. Measured diffraction patterns are shown in Fig. 6.11. The GSAS-II software package [31] was used to extract lattice parameters from diffraction patterns in a series of Rietveld refinements where the current histogram refinement results were used as a starting point for refinement at the next temperature in the series. The procedure included fitting of the starting 30 K histogram where after background fitting (I used 6th order Chebyshev polynomial), lattice parameter was refined with respect to sample displacement (value after refinement equal to 122.6424 ± 1.56), domain size (0.1745 ± 0.0019), and uniaxial mustrains (1151.4 ± 21.6 , 6423.0 ± 113.5) in the corresponding order (the thermal factor U_{iso} was kept fixed with value of 0.01). The instrument parameters were obtained from silicon standard and are presented in Fig. 6.16. The refinement parameters for each histogram include background, scale factor and sample displacement, and elastic strain, leading to a total of 10 free parameters (other parameters were fixed to the values obtained at 15 K). The refinement results are given in the Fig. 6.17. The obtained lattice parameters as a function of temperature are shown in Fig. 6.12.

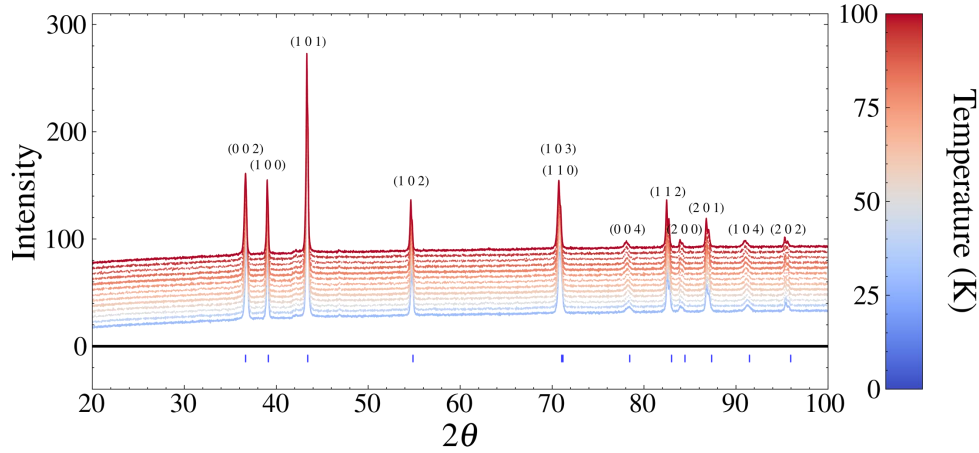


Figure 6.11: Zinc X-ray diffraction patterns measured from 30 to 100 K. Peaks are indexed. Positions of diffractions are shown with blue markers.

Static part of the compliance tensor for temperature dependent effective potential

I start with the TDEP expression for the static part of the free energy.

$$U_0^{TDEP} = \left\langle U_{DFT}(T, V) - \frac{1}{2} \sum_{i,j} \sum_{\alpha,\beta} \Phi_{i,j}^{\alpha,\beta}(T, V) u_i^\alpha u_j^\beta - \frac{1}{6} \sum_{i,j,k} \sum_{\alpha,\beta,\gamma} \Phi_{i,j,k}^{\alpha,\beta,\gamma}(T, V) u_i^\alpha u_j^\beta u_k^\gamma \right\rangle \quad (6.17)$$

$$= \left\langle U_{DFT} - V_2 - V_3 \right\rangle, \quad (6.18)$$

where V_2 and V_3 are terms attributed to second and third-order force constants.

The corresponding part of the stress tensor:

$$\begin{aligned} \sigma_{\alpha\beta}^0 &= \frac{1}{V} \frac{\partial U_0^{TDEP}}{\partial \varepsilon_{\alpha\beta}} = \left\langle \frac{1}{V} \frac{\partial U_{DFT}}{\partial \varepsilon_{\alpha\beta}} - \frac{1}{2} \frac{\partial V_2}{\partial \varepsilon_{\alpha\beta}} - \frac{1}{6} \frac{\partial V_3}{\partial \varepsilon_{\alpha\beta}} \right\rangle \\ &= \left\langle \sigma_{\alpha\beta}^{DFT} - \frac{1}{2} \frac{\partial V_2}{\partial \varepsilon_{\alpha\beta}} - \frac{1}{6} \frac{\partial V_3}{\partial \varepsilon_{\alpha\beta}} \right\rangle, \end{aligned} \quad (6.19)$$

where $\sigma_{\alpha\beta}^{DFT}$ is the stress tensor obtained from density function theory for the configuration of the ensemble.

Here, I derive the expression for V_2 . For the V_3 , I give a final result since it follows the steps of the V_2 case. In the following, I use Einstein's notation for tensor contraction.

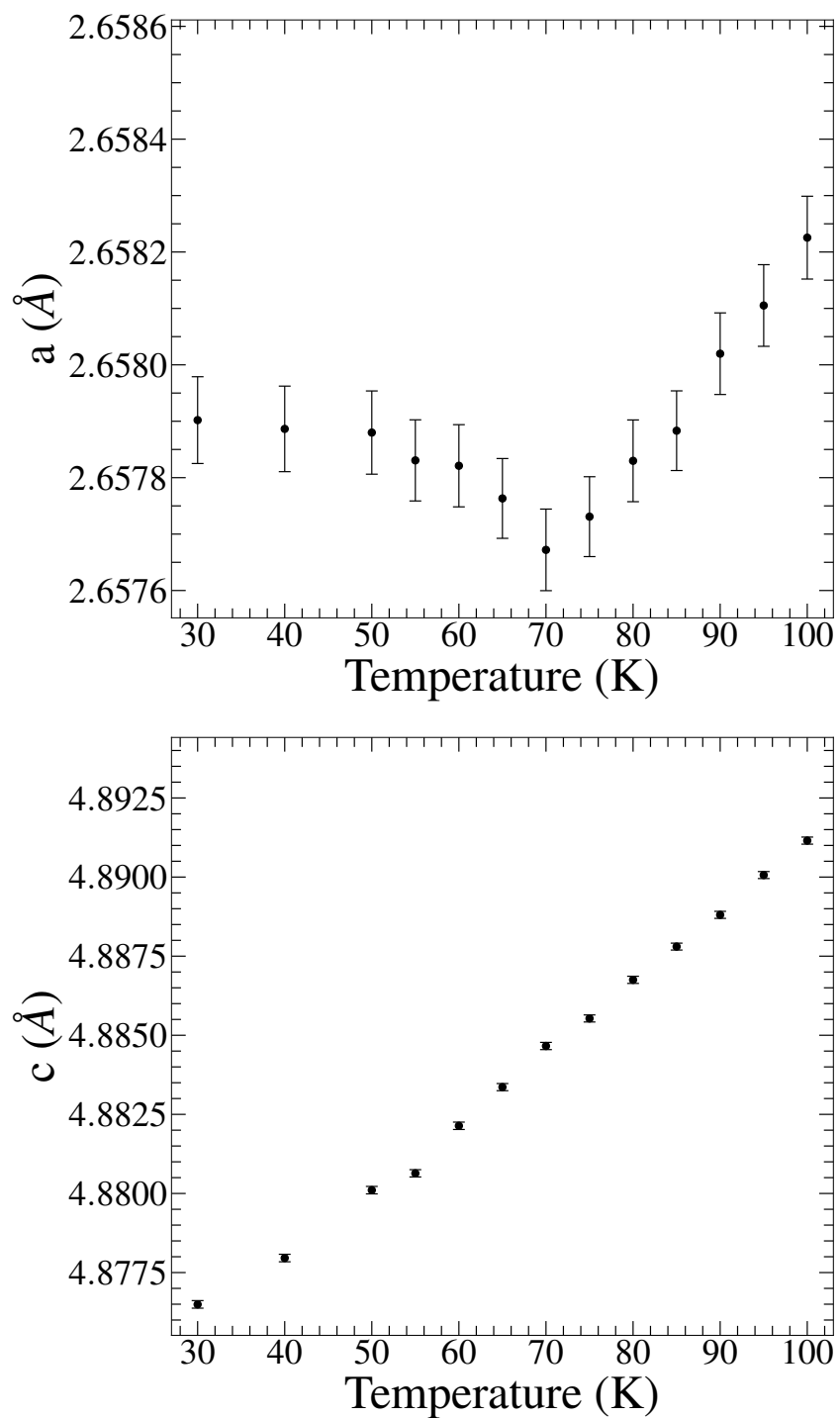


Figure 6.12: Temperature dependence of the lattice parameters of Zinc extracted from X-ray diffraction data. Confidence intervals are shown with errorbars.

$$\begin{aligned} \frac{\partial V_2}{\partial \varepsilon_{\alpha\beta}} &= \partial_{\varepsilon_{\alpha\beta}} \left(\Phi_{ij}^{\gamma\delta} u_i^\gamma u_j^\delta \right) = \Phi_{ij}^{\gamma\delta} (u_i^\alpha \delta_\gamma^\beta u_j^\delta + u_i^\gamma u_j^\beta \delta_\delta^\alpha) \\ &+ u_i^\gamma u_j^\delta \partial_{\varepsilon_{\alpha\beta}} \Phi_{ij}^{\gamma\delta} = \Phi_{ij}^{\beta\delta} u_i^\alpha u_j^\delta + \Phi_{ij}^{\gamma\alpha} u_i^\gamma u_j^\beta + u_i^\gamma u_j^\delta \partial_{\varepsilon_{\alpha\beta}} \Phi_{ij}^{\gamma\delta}. \end{aligned} \quad (6.20)$$

Here, I used the fact that $\partial u^\gamma / \varepsilon_{\alpha\beta} = u^\alpha \delta_\gamma^\beta$.

Relating the last expression to the harmonic part of the force in the temperature dependent effective potential $f_i^{(2)\alpha} = -\Phi_{ij}^{\alpha\beta} u_j^\beta$ [32, 33]

$$\frac{\partial V_2}{\partial \varepsilon_{\alpha\beta}} = - \sum_i (u_i^\alpha f_i^{(2)\beta} + u_i^\beta f_i^{(2)\alpha}) + u_i^\gamma u_j^\delta \partial_{\varepsilon_{\alpha\beta}} \Phi_{ij}^{\gamma\delta}. \quad (6.21)$$

The $\partial_{\varepsilon_{\alpha\beta}} \Phi_{ij}^{\gamma\delta}$ can be found from Taylor expansions of second order force constants with respect to displacements $\vec{r}'_i = \vec{r}_i + \vec{u}_i$

$$\Phi_{ij}^{\gamma\delta}(\vec{r}') = \Phi_{ij}^{\gamma\delta}(\vec{r}) + \Phi_{ijk}^{\gamma\delta\alpha} u_k^\alpha + O(u^2). \quad (6.22)$$

In the case of the strain $u_i^\alpha = \varepsilon_{\alpha\beta} r_i^\beta$

$$\Phi_{ij}^{\gamma\delta}(\varepsilon_{\alpha\beta}) = \Phi_{ij}^{\gamma\delta}(\varepsilon_{\alpha\beta} = 0) + \Phi_{ijk}^{\gamma\delta\alpha} \varepsilon_{\alpha\beta} r_k^\beta + O(\varepsilon_{\alpha\beta}^2). \quad (6.23)$$

$$\partial_{\varepsilon_{\alpha\beta}} \Phi_{ij}^{\gamma\delta} = \Phi_{ijk}^{\gamma\delta\alpha} r_k^\beta. \quad (6.24)$$

Substituting the result into rightmost term Eq. 6.21

$$\begin{aligned} u_i^\gamma u_j^\delta \partial_{\varepsilon_{\alpha\beta}} \Phi_{ij}^{\gamma\delta} &= u_i^\gamma u_j^\delta \Phi_{ijk}^{\gamma\delta\alpha} r_k^\beta = r_k^\beta \Phi_{kij}^{\alpha\gamma\delta} u_i^\gamma u_j^\delta \\ &= -2r_k^\beta f_k^{(3)\alpha} = -2r_k^\alpha f_k^{(3)\beta}, \end{aligned} \quad (6.25)$$

where $f_k^{(3)\beta}$ is the contribution from third-order forceconstants to forces in TDEP formalism [33].

The final expression for the V_2 term is

$$\begin{aligned} \frac{1}{V} \frac{1}{2} \partial_{\varepsilon_{\alpha\beta}} V_2 &= -\frac{1}{V} \left(\frac{1}{2} u_i^\alpha f_i^{(2)\beta} + \frac{1}{2} u_i^\beta f_i^{(2)\alpha} \right) - r_k^\alpha f_k^{(3)\beta} \\ &= -\frac{1}{V} \left(u_i^\alpha f_i^{(2)\beta} + r_k^\alpha f_k^{(3)\beta} \right). \end{aligned} \quad (6.26)$$

$u_i^\alpha f_i^{(2)\beta} = \frac{1}{2} u_i^\beta f_i^{(2)\alpha}$ due to periodic crystal symmetry.

A similar expression for the V_3

$$\frac{1}{V} \frac{1}{6} \partial_{\varepsilon_{\alpha\beta}} V_3 = -\frac{1}{V} \left(u_i^\alpha f_i^{(3)\beta} + r_k^\alpha f_k^{(4)\beta} \right). \quad (6.27)$$

With the static part of the stress tensor

$$\sigma_{\alpha\beta}^0 = \left\langle \sigma_{\alpha\beta}^{DFT} - \frac{1}{V} \left(u_i^\alpha f_i^{(2)\beta} + r_k^\alpha f_k^{(3)\beta} \right) - \frac{1}{V} \left(u_i^\alpha f_i^{(3)\beta} + r_k^\alpha f_k^{(4)\beta} \right) \right\rangle. \quad (6.28)$$

I note that pressure fluctuations are exclusively captured by the third-order force constants, as the second-order contribution yields a kinetic, ideal-gas-like term. However, I found that the second-order force constants are important to describe fluctuations of the off-diagonal stress tensor components. All expressions presented here are implemented in the TDEP code [34].

Construction of Machine Learning Interatomic Potentials (MLIP)

I used moment tensor potentials (MTP) [15] to model the interatomic interactions. Moment tensors are flexible basis functions helpful in learning the lattice dynamics of a system, including anharmonic effects [35]. The construction of machine learning interatomic potentials (MLIP) followed the procedure of Ref. [36]. I generated the MLIP from configurations actively sampled from molecular dynamics simulations at temperature from 15 K to 690 K. Different candidate lengths of the a and c axes were chosen on the grid with $\pm 10\%$ of their equilibrium values at the corresponding temperature. The training set contained 117 configurations post-processed with VASP providing reference energies, forces, and stresses [19–22]. The average difference between the fitted potential and the potential from the ab initio model was 2 meV/atom. Using Eq. 3.17, I calculated a relative difference of 7 % in forces, and 10 % in stresses.

Analyses of diffuse intensity generation through third order anharmonicity and beyond

To perform sTDEP computations of temperature dependent phonon lineshapes presented in Fig. 6.13 I followed the procedure described in Supplemental of [37]. The linewidths from sTDEP are able to reproduce the experimental features in the phonon spectra of Zn, including the formation of diffuse intensity at 15 K. The TDEP reproduces additional intensity formation at Γ and A points, and the frequency shifts of diffuse intensity with temperature.

Path Integral Molecular Dynamics

Path Integral Molecular Dynamics (PIMD) simulations capture the correct physics of zero-point energy. The efficient LAMMPS realization of PIMD in the NPT

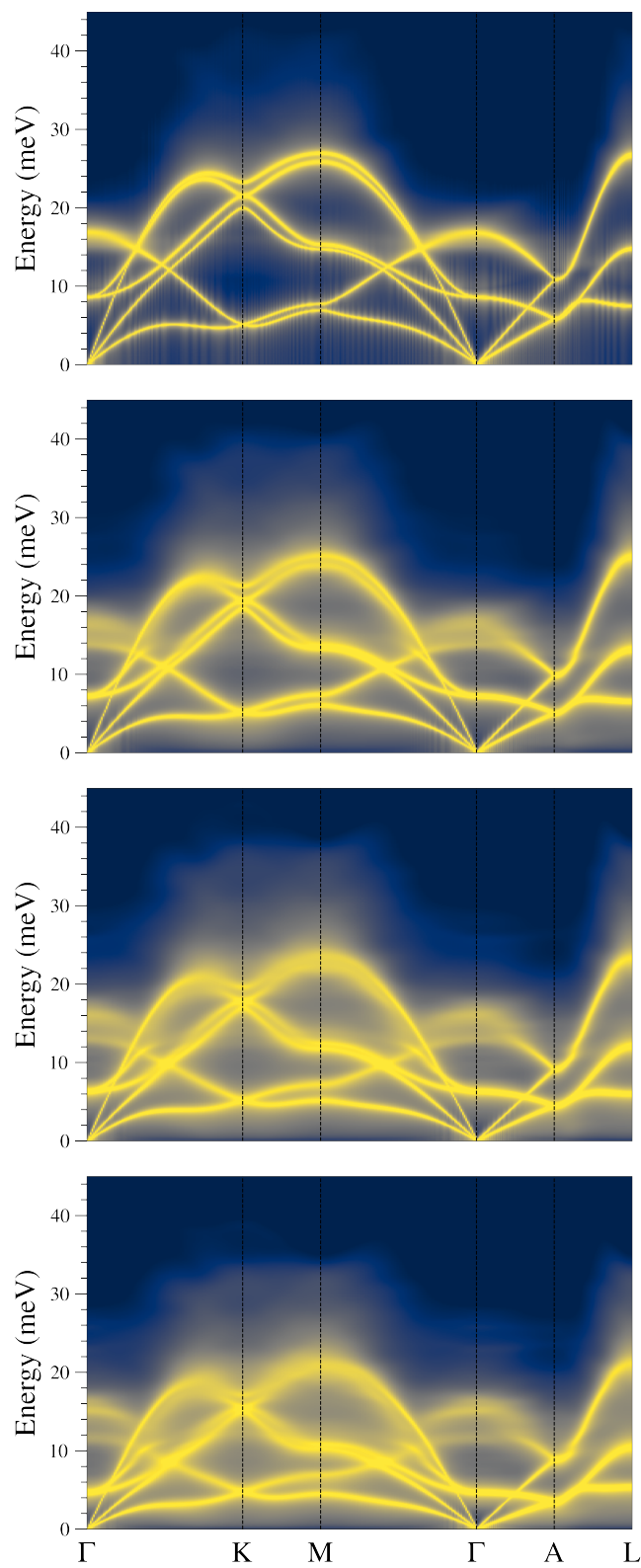


Figure 6.13: Calculated sTDEP phonon dispersions along high-symmetry directions for temperatures from top to bottom: 15 K, 300 K, 500 K, and 690 K.

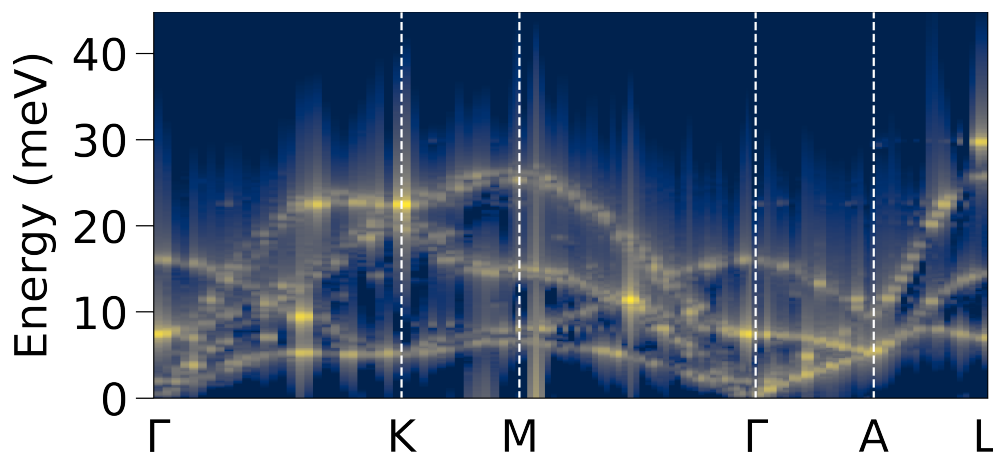


Figure 6.14: Phonon dispersions along high-symmetry directions calculated by projected velocity-velocity autocorrelation function method at 15 K using BCMD.

ensemble [38] was used to perform a simulation with multiple beads to estimate the nuclear quantum effects that alter the thermal expansion of Zn at low temperatures. The supercell size for cell parameter equilibration was chosen in correspondence with the TDEP calculations ($10 \times 10 \times 5$ with 1000 atoms). A number of beads equal to 64 was obtained on the basis of the convergence of the equilibrium lattice parameters used in the simulation as discussed below.

In [39, 40] the authors proposed a new path integral method to calculate dynamical properties such as a two-point autocorrelation function in the low temperature limit called Brownian Chain Molecular Dynamics (BCMD). I used BCMD as implemented in the PIMD software package [41] to perform a long-range large-scale molecular dynamics simulation with multiple beads at 15 K. For BCMD calculations, the supercell size was $40 \times 40 \times 20$ with 64,000 atoms due to computational complexity. The projected velocity-velocity autocorrelation functions came from 4 statistically independent 10 ps BCMD trajectories. For large-scale BCMD simulations, I used the number of beads equal to 32 with accuracy comparable to the number of beads used in thermal expansion simulations. The vibrational spectra at 15 K obtained with the projected velocity autocorrelation functions obtained from the BCMD simulations are shown in Fig. 6.14. The inclusion of nuclear quantum effects allows the generation of diffuse intensity at the *K* point and around the *A* point at 15 K.

Some results from the convergence testing for the number of beads in BCMD simulations at 10 K are shown in Fig. 6.15. Simulations were performed in the NPT ensemble for the set of beads [8, 16, 32, 64]. From Fig. 6.15(c),(d) the optimal

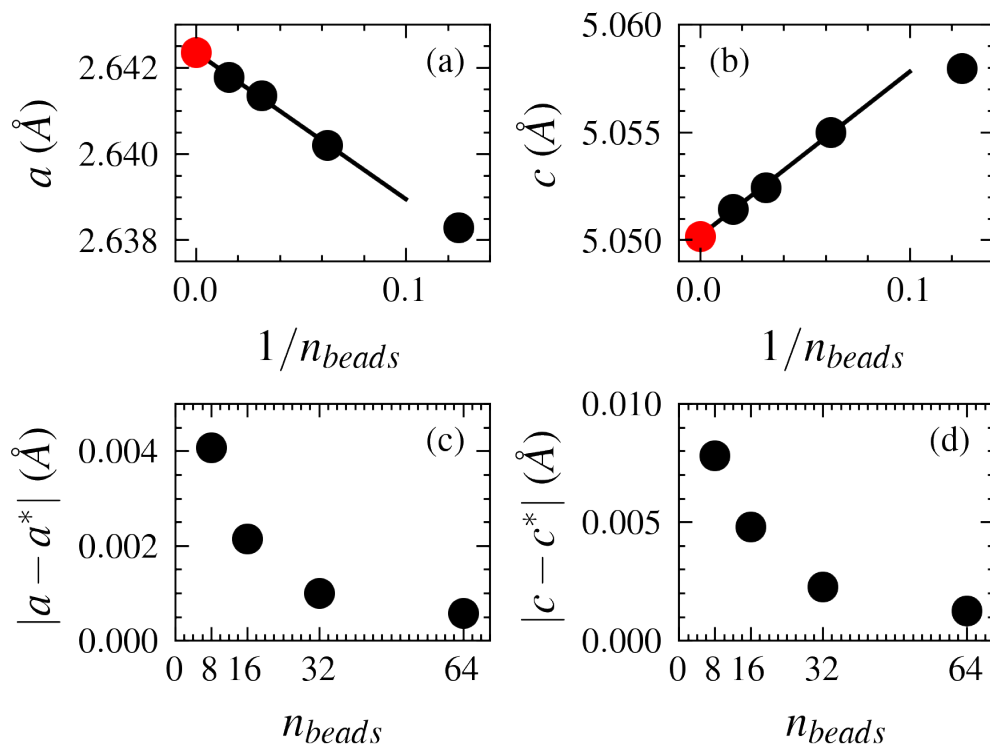


Figure 6.15: Convergence of lattice parameters in the PIMD simulation at 10 K. (a),(b) show limits as the number of beads approach infinity: black dots - NPT simulation results of lattice parameters; solid curve - linear fit of the function $f(1/n_{bead})$; red dot - limit of lattice parameter at number of beads equal approaching infinity. (c),(d) error in lattice parameter estimation with respect to a number of beads (a^* , c^* denote the limit with number of beads approaching infinity).

number of beads was selected to be 64 for lattice parameter determination, and 32 for the large-scale BCMD simulations.

Instrument settings

Histogram Type: PXC Bank: 1
 Azimuth: 0.00 Ka1/Ka2: 1.540510/1.544330Å Source type: **CuKa** 

Name (default)	Value	Refine?
I(L2)/I(L1) (0.4234):	<input type="text" value="0.4234"/>	<input type="checkbox"/>
Zero (-0.0083):	<input type="text" value="-0.0083"/>	<input type="checkbox"/>
Polariz. (0.5840):	<input type="text" value="0.584"/>	<input type="checkbox"/>
U (4.022):	<input type="text" value="4.022"/>	<input type="checkbox"/>
V (-0.988):	<input type="text" value="-0.988"/>	<input type="checkbox"/>
W (3.463):	<input type="text" value="3.463"/>	<input type="checkbox"/>
X (-8.542):	<input type="text" value="-8.542"/>	<input type="checkbox"/>
Y (4.907):	<input type="text" value="4.907"/>	<input type="checkbox"/>
Z (8.976):	<input type="text" value="8.976"/>	<input type="checkbox"/>
SH/L (0.00662):	<input type="text" value="0.00662"/>	<input type="checkbox"/>

References:
 Thompson, P., Cox, D.E. Hastings, J.B. (1987). J. Appl. Cryst. 20,79-83.
 Finger, L. W., Cox, D. E. Jephcoat, A. P. (1994). J. Appl. Cryst. 27, 892-900.

Figure 6.16: Instrument parameters for GSAS-II Rietveld refinement.

Sequential results:

	No.	Use	$\Delta\chi^2$ (%)	a	c	bkgd0	bkgd1	bkgd2	bkgd3	bkgd4	bkgd5	Scale factor	Sample Displ.
25_27_100_Phenix_Zn_30.00K.xy	0	<input checked="" type="checkbox"/>	-0.02771	2.65790	4.87649	3524.123627	754.622672	-336.901314	182.457374	-51.800847	-100.368425	577.722717	122.642437
24_27_100_Phenix_Zn_40.00K.xy	2	<input checked="" type="checkbox"/>	-0.00566	2.65789	4.87798	3533.426068	753.881524	-344.963835	175.044700	-55.679938	-93.656037	577.647980	121.917678
23_27_100_Phenix_Zn_50.00K.xy	1	<input checked="" type="checkbox"/>	0.05193	2.65788	4.88010	3513.053054	763.916638	-347.798579	68.899660	-33.083719	-6.399866	592.688632	125.839943
22_27_100_Phenix_Zn_55.00K.xy	8	<input checked="" type="checkbox"/>	0.05444	2.65783	4.88064	3513.534855	769.942800	-371.638367	50.083721	-3.134236	14.230696	593.957562	128.754086
21_27_100_Phenix_Zn_60.00K.xy	9	<input checked="" type="checkbox"/>	0.06221	2.65782	4.88214	3510.814341	762.769986	-352.981038	85.491559	-17.989970	-14.714094	587.680532	127.107782
20_27_100_Phenix_Zn_65.00K.xy	3	<input checked="" type="checkbox"/>	0.08392	2.65776	4.88338	3508.931598	753.042421	-337.330077	133.972763	-45.212520	-57.457407	586.525495	129.640469
19_27_100_Phenix_Zn_70.00K.xy	14	<input checked="" type="checkbox"/>	0.00032	2.65767	4.88466	3512.721707	747.937793	-343.860220	152.728474	-35.896740	-71.582883	582.870538	132.029741
18_27_100_Phenix_Zn_75.00K.xy	6	<input checked="" type="checkbox"/>	0.00039	2.65773	4.88553	3514.743114	756.050494	-360.106640	106.861486	-16.023304	-32.141842	585.705876	132.624558
17_27_100_Phenix_Zn_80.00K.xy	12	<input checked="" type="checkbox"/>	0.00055	2.65783	4.88678	3519.299822	760.959656	-357.875734	85.836830	-22.603009	-17.352996	583.124695	130.325742
16_27_100_Phenix_Zn_85.00K.xy	5	<input checked="" type="checkbox"/>	0.00425	2.65788	4.88780	3516.894711	737.381708	-352.640134	154.129330	-28.125256	-70.205012	590.796085	131.031585
15_27_100_Phenix_Zn_90.00K.xy	7	<input checked="" type="checkbox"/>	-0.00145	2.65802	4.88881	3520.603394	756.078577	-366.215675	81.735220	-18.087197	-9.093649	588.570867	128.953895
14_27_100_Phenix_Zn_95.00K.xy	13	<input checked="" type="checkbox"/>	0.00416	2.65811	4.89008	3520.991587	728.498845	-352.322059	184.722904	-35.005489	-90.097185	585.331847	128.933925
13_27_100_Phenix_Zn_100.00K.xy	4	<input checked="" type="checkbox"/>	0.00480	2.65823	4.89115	3523.159901	753.587176	-366.247156	92.631437	-19.993177	-18.976325	586.427606	128.550221
12_27_100_Phenix_Zn_105.00K.xy	10	<input checked="" type="checkbox"/>	0.00603	2.65837	4.89240	3524.523334	744.475077	-373.806619	105.212457	-5.092234	-20.663583	585.171824	126.996760
11_27_100_Phenix_Zn_110.00K.xy	11	<input checked="" type="checkbox"/>	0.00959	2.65849	4.89344	3527.519870	742.096379	-378.905393	113.948950	-1.384727	-22.967657	584.134795	126.031033

Figure 6.17: Results of Rietveld refinement.

References

- [1] A. A. Maradudin and A. E. Fein. Scattering of neutrons by an anharmonic crystal. *Phys. Rev.*, 128:2589–2608, 1962. doi: 10.1103/PhysRev.128.2589. URL <https://link.aps.org/doi/10.1103/PhysRev.128.2589>.
- [2] D. S. Kim, O. Hellman, J. Herriman, H. L. Smith, J. Y. Y. Lin, N. Shulumba, J. L. Niedziela, C. W. Li, D. L. Abernathy, and B. Fultz. Nuclear quantum effect with pure anharmonicity and the anomalous thermal expansion of silicon. *Proc. Natl. Acad. Sci. USA*, 115(9):1992–1997, 2018. ISSN 0027-8424. doi: 10.1073/pnas.1707745115. URL <https://www.pnas.org/content/115/9/1992>.
- [3] C. N. Saunders, D. S. Kim, O. Hellman, H. L. Smith, N. J. Weadock, S. T. Omelchenko, G. E. Granroth, C. M. Bernal-Choban, S. H. Lohaus, D. L. Abernathy, and B. Fultz. Thermal expansion and phonon anharmonicity of cuprite studied by inelastic neutron scattering and *ab initio* calculations. *Phys. Rev. B*, 105:174308, May 2022. doi: 10.1103/PhysRevB.105.174308. URL <https://link.aps.org/doi/10.1103/PhysRevB.105.174308>.
- [4] Yang Shen, C. N. Saunders, C. M. Bernal, D. L. Abernathy, T. J. Williams, M. E. Manley, and B. Fultz. Prediction and observation of intermodulation sidebands from anharmonic phonons in NaBr. *Phys. Rev. B*, 103(13):134302, 2021.
- [5] R. D. McCammon and G. K. White. Thermal expansion at low temperatures of hexagonal metals: Mg, Zn and Cd. *Philos. Mag.*, 11(114):1125–1134, 1965.
- [6] D. A. Channing and S. Weintroub. Thermal expansion of single crystals of zinc at low temperatures. *Can. J. Phys.*, 43(7):1328–1333, 1965.
- [7] T. Vreeland, Jr. Tilt boundary motion in zinc produced by static and dynamic shear stress. *Acta Metallurgica*, 9(2):112–116, 1961.
- [8] D. L. Abernathy, M. B. Stone, M. J. Loguillo, M. S. Lucas, O. Delaire, X. Tang, J. Y. Y. Lin, and B. Fultz. Design and operation of the wide angular-range chopper spectrometer ARCS at the Spallation Neutron Source. *Rev. Sci. Instrum.*, 83(1):015114, 2012. doi: 10.1063/1.3680104. URL <https://doi.org/10.1063/1.3680104>.
- [9] T.E. Mason, D. Abernathy, I. Anderson, J. Ankner, T. Egami, G. Ehlers, A. Ekkebus, G. Granroth, M. Hagen, K. Herwig, J. Hodges, C. Hoffmann, C. Horak, L. Horton, F. Klose, J. Larese, A. Mesecar, D. Myles, J. Neufeind, M. Ohl, C. Tulk, X-L. Wang, and J. Zhao. The Spallation Neutron Source in Oak Ridge: A powerful tool for materials research. *Physica B Condens. Matter*, 385-386:955–960, 2006. ISSN 0921-4526. doi: 10.1016/j.physb.2006.05.281. URL <https://www.sciencedirect.com/science/article/pii/S092145260601177X>.

- [10] D. Abernathy, G. Granroth, and R. Goyette. ARCS white beam vanadium normalization data for SNS cycle 2022B. URL [10.14461/oncat.data/2515590](https://doi.org/10.14461/oncat.data/2515590).
- [11] V. F. Sears, E. C. Svensson, and B. M. Powell. Phonon density of states in vanadium. *Can. J. Phys.*, 73(11-12):726–734, 1995.
- [12] V. Ladygin, C. Saunders, C. Bernal-Choban, D. Abernathy, M. Manley, and B. Fultz. Phonon second harmonic generation in nabr studied by inelastic neutron scattering and computer simulation. *Phys. Rev. Mater.*, 9:015002, Jan 2025. doi: [10.1103/PhysRevMaterials.9.015002](https://doi.org/10.1103/PhysRevMaterials.9.015002).
- [13] D. C. Wallace. *Thermodynamics of Crystals*. J. Wiley, New York, 1998.
- [14] J. F. Nye. *Physical Properties of Solids*. Oxford University Press, 1957.
- [15] A. V. Shapeev. Moment tensor potentials: A class of systematically improvable interatomic potentials. *Multiscale Modeling & Simulation*, 14(3): 1153–1173, 2016. doi: [10.1137/15M1054183](https://doi.org/10.1137/15M1054183). URL <https://doi.org/10.1137/15M1054183>.
- [16] A. P. Thompson, H. M. Aktulga, R. Berger, D. S. Bolintineanu, W. M. Brown, P. S. Crozier, P. J. in't Veld, A. Kohlmeyer, S. G. Moore, T. D. Nguyen, R. Shan, M. J. Stevens, J. Tranchida, C. Trott, and S. J. Plimpton. LAMMPS - a flexible simulation tool for particle-based materials modeling at the atomic, meso, and continuum scales. *Comp. Phys. Comm.*, 271:108171, 2022. doi: [10.1016/j.cpc.2021.108171](https://doi.org/10.1016/j.cpc.2021.108171).
- [17] C. N. Saunders. *Thermal Behavior of Cuprous Oxide: a Comprehensive Study of Three-Body Phonon Effects and Beyond*. PhD thesis, California Institute of Technology, 2022. URL <https://resolver.caltech.edu/CaltechTHESIS:05262022-015714738>.
- [18] J. Lahnsteiner and M. Bokdam. Anharmonic lattice dynamics in large thermodynamic ensembles with machine-learning force fields: CsPbBr₃, a phonon liquid with Cs rattlers. *Phys. Rev. B*, 105:024302, Jan 2022. doi: [10.1103/PhysRevB.105.024302](https://doi.org/10.1103/PhysRevB.105.024302). URL <https://link.aps.org/doi/10.1103/PhysRevB.105.024302>.
- [19] G. Kresse and J. Hafner. Ab initio molecular dynamics for liquid metals. *Phys. Rev. B*, 47:558–561, 1993. doi: [10.1103/PhysRevB.47.558](https://doi.org/10.1103/PhysRevB.47.558). URL <https://link.aps.org/doi/10.1103/PhysRevB.47.558>.
- [20] G. Kresse and J. Hafner. Ab initio molecular-dynamics simulation of the liquid-metal–amorphous–semiconductor transition in germanium. *Phys. Rev. B*, 49:14251–14269, 1994. doi: [10.1103/PhysRevB.49.14251](https://doi.org/10.1103/PhysRevB.49.14251). URL <https://link.aps.org/doi/10.1103/PhysRevB.49.14251>.

- [21] G. Kresse and J. Furthmüller. Efficiency of *ab initio* total energy calculations for metals and semiconductors using a plane-wave basis set. *Comput. Mater. Sci.*, 6(1):15 – 50, 1996. ISSN 0927-0256. doi: 10.1016/0927-0256(96)00008-0. URL <http://www.sciencedirect.com/science/article/pii/0927025696000080>.
- [22] G. Kresse and J. Furthmüller. Efficient iterative schemes for *ab initio* total-energy calculations using a plane-wave basis set. *Phys. Rev. B*, 54:11169–11186, 1996. doi: 10.1103/PhysRevB.54.11169. URL <https://link.aps.org/doi/10.1103/PhysRevB.54.11169>.
- [23] G. Kresse and D. Joubert. From ultrasoft pseudopotentials to the projector augmented-wave method. *Phys. Rev. B*, 59:1758–1775, Jan 1999. doi: 10.1103/PhysRevB.59.1758. URL <https://link.aps.org/doi/10.1103/PhysRevB.59.1758>.
- [24] J. P. Perdew, K. Burke, and M. Ernzerhof. Generalized gradient approximation made simple. *Phys. Rev. Lett.*, 77:3865–3868, Oct 1996. doi: 10.1103/PhysRevLett.77.3865. URL <https://link.aps.org/doi/10.1103/PhysRevLett.77.3865>.
- [25] M. S. Nitol, D. E. Dickel, and C. D. Barrett. Artificial neural network potential for pure zinc. *Comput. Mater. Sci.*, 188:110207, 2021.
- [26] H. Mei, L. Cheng, L. Chen, F. Wang, J. Li, and L. Kong. Development of machine learning interatomic potential for zinc. *Comput. Mater. Sci.*, 233:112723, 2024.
- [27] J. Nuss, U. Wedig, A. Kirfel, and M. Jansen. The structural anomaly of zinc: Evolution of lattice constants and parameters of thermal motion in the temperature range of 40 to 500 k. *Z. Anorg. Allg. Chem.*, 636(2):309–313, 2010. doi: <https://doi.org/10.1002/zaac.200900460>. URL <https://onlinelibrary.wiley.com/doi/abs/10.1002/zaac.200900460>.
- [28] T. Bučko, S. Lebègue, J. Hafner, and J. G. Angyan. Tkatchenko-scheffler van der waals correction method with and without self-consistent screening applied to solids. *Phys. Rev. B*, 87(6):064110, 2013.
- [29] O. Arnold, J. C. Bilheux, J. M. Borreguero, A. Buts, S.I. Campbell, L. Chapon, M. Doucet, N. Draper, R. Ferraz Leal, M. A. Gigg, V. E. Lynch, A. Markvardsen, D. J. Mikkelson, R. L. Mikkelson, R. Miller, K. Palmen, P. Parker, G. Passos, T. G. Perring, P. F. Peterson, S. Ren, M. A. Reuter, A. T. Savici, J. W. Taylor, R. J. Taylor, R. Tolchenov, W. Zhou, and J. Zikovsky. Mantid—data analysis and visualization package for neutron scattering and μ sr experiments. *Nucl. Instrum. Meth. A*, 764:156–166, 2014. ISSN 0168-9002. doi: <https://doi.org/10.1016/j.nima.2014.07.029>. URL <https://www.sciencedirect.com/science/article/pii/S0168900214008729>.

- [30] Y. Shen, C. N. Saunders, C. M. Bernal, D. L. Abernathy, M. E. Manley, and B. Fultz. Anharmonic origin of the giant thermal expansion of nabr. *Phys. Rev. Lett.*, 125(8):085504, 2020.
- [31] B. H. Toby and R. B. Von Dreele. Gsas-ii: The genesis of a modern open-source all purpose crystallography software package. *Appl. Cryst.*, 46(2):544–549, 2013.
- [32] O. Hellman, I. A. Abrikosov, and S. I. Simak. Lattice dynamics of anharmonic solids from first principles. *Phys. Rev. B*, 84:180301, 2011. doi: 10.1103/PhysRevB.84.180301. URL <https://link.aps.org/doi/10.1103/PhysRevB.84.180301>.
- [33] F. Knoop, T. A. R. Purcell, M. Scheffler, and C. Carbogno. Anharmonicity measure for materials. *Phys. Rev. Mater.*, 4:083809, Aug 2020. doi: 10.1103/PhysRevMaterials.4.083809. URL <https://link.aps.org/doi/10.1103/PhysRevMaterials.4.083809>.
- [34] F. Knoop, N. Shulumba, A. Castellano, J. P. Alvarinhas Batista, R. Farris, M. J. Verstraete, M. Heine, D. Broido, D. S. Kim, J. Klarbring, et al. Tdep: Temperature dependent effective potentials. *J. Open Source Software*, 9(94), 2024.
- [35] V. V. Ladygin, P. Yu. Korotaev, A. V. Yanilkin, and A. V. Shapeev. Lattice dynamics simulation using machine learning interatomic potentials. *Comput. Mater. Sc.*, 172:109333, 2020. ISSN 0927-0256. doi: <https://doi.org/10.1016/j.commatsci.2019.109333>. URL <https://www.sciencedirect.com/science/article/pii/S0927025619306329>.
- [36] I. S. Novikov, K. Gubaev, E. V. Podryabinkin, and A. V. Shapeev. The MLIP package: Moment tensor potentials with mpi and active learning. *Mach. Learn.: Sci. Technol.*, 2(2):025002, 2020. doi: 10.1088/2632-2153/abc9fe.
- [37] N. Benshalom, G. Reuveni, R. Korobko, O. Yaffe, and O. Hellman. Dielectric response of rock-salt crystals at finite temperatures from first principles. *Phys. Rev. Mater.*, 6(3):033607, 2022.
- [38] Y. Liu, V. S. Bryantsev, M. S. Diallo, and W. A. Goddard III. Pamam dendrimers undergo ph responsive conformational changes without swelling. *J. Am. Chem. Soc.*, 131(8):2798–2799, 2009. doi: 10.1021/ja8100227. URL <https://doi.org/10.1021/ja8100227>. PMID: 19199433.
- [39] M. Shiga. Path integral brownian chain molecular dynamics: A simple approximation of quantum vibrational dynamics. *J. of Comp. Chem.*, 43(27):1864–1879, 2022. doi: <https://doi.org/10.1002/jcc.26989>. URL <https://onlinelibrary.wiley.com/doi/abs/10.1002/jcc.26989>.

- [40] M. Shiga, B. Thomsen, and H. Kimizuka. Inelastic neutron scattering of hydrogen in palladium studied by semiclassical dynamics. *Phys. Rev. B*, 109: 054303, Feb 2024. doi: 10.1103/PhysRevB.109.054303. URL <https://link.aps.org/doi/10.1103/PhysRevB.109.054303>.
- [41] M. Shiga, M. Tachikawa, and S. Miura. A unified scheme for ab initio molecular orbital theory and path integral molecular dynamics. *J. Chem. Phys.*, 115(20): 9149–9159, 2001.

FINAL REMARKS AND FUTURE DIRECTIONS

7.1 New Methods Development

In the thesis, I focused on the anharmonic effects related to lattice degrees of freedom. However, in the example of NaBr, it is seen that the interaction of lattice and dipole degrees of freedom is essential. Recent advances in Raman spectra calculation [1] and interatomic potential construction [1, 2] allow modeling electrostatic effects in molecular dynamics simulation. In the case of polar materials, result can be compared to the phonon behavior computed from the electric susceptibility response function to show the connection between phonon intermodulation and optical response experiments.

Another example of nontrivial dynamics is the interplay of lattice and spin degrees of freedom. For example, in [3], an accurate treatment of this interaction allows describing zero thermal expansion in an invar alloy¹. Thus, an accurate modeling of the effects of spin-lattice interaction possibly leads to a new direction in the exploration of anharmonic effects.

In particular, the simulations can show the contribution of anharmonic effects in magnetic materials, accurately predicting macroscopic properties such as thermal expansion and estimating the strength of spin-lattice coupling. Current approaches to study magnetic materials either neglect vibrational effects and anharmonicity or focus on the selective representation of spin states [3]. An accurate description of the spin-lattice interaction is possible in large-scale molecular dynamics simulations using machine learning interatomic potential [4]. The anharmonic part of vibrational free energy is captured with autocorrelation function analyses. In this case, the magnetic degrees of freedom are modeled with a collinear approach where spins are allowed to change in absolute value and sign. I propose a study of vibrational lattice dynamics of Fe₆₈Pd₃₂, known for its low thermal expansion under pressure in the ferromagnetic-paramagnetic transition region [5, 6]. Similar to invar [3], the direct comparison can be obtained from the pressure dependence of vibrational spectra and magnetization. I propose to study the anharmonic part of the thermal

¹Invar is a Fe₆₅Ni₃₅ alloy with low thermal expansion in a large interval around room temperature.

expansion using molecular dynamics simulation with a collinear model for spins for the case of Fe₆₈Pd₃₂. In the computational approach, we started with fitting the potential on DFT data (comparison between the reference model and the MLIP results for magnetization is given in Fig. 7.1). The MTP captures the behavior of the ferromagnetic phase compared to the DFT model, but misses the transition to the nonmagnetic state, which we attribute to the limitations of MD simulations for sampling the potential energy surface of magnetic systems. The issue can be resolved in the future work by including more paramagnetic states in the training set of the MLIP, extending spin basis for more accurate magnetic moment fitting, and using Monte-Carlo algorithms to allow magnetic moment flip in MD simulations. The limitations of the collinear spin model result in inaccurate phase transition prediction by DFT (around 30 GPa compared to 10 GPa observed in experiment). This issue is inherited by MLIP. The solution lies in using spin-polarized calculation as a reference model and MLIPs with noncollinear spin features with time-reversal symmetry [7].

The next step is to compare the vibrational density of states from the autocorrelation function calculations between moment tensor potential (MTP) and DFT simulations (Fig. 7.2). The simulations show excellent agreement, considering that the autocorrelation function calculations require a large supercell. The discrepancy at low temperatures is attributed to the finite size effects (Fig. 7.3). The general softening of the vibrational spectra is reproduced by large-scale MD simulation with a collinear spin model, Fig. 7.3. The approach described above can be extended to provide a fundamental understanding of the mechanical properties of other magnetic materials with an invar effect, such as Fe-Co, Ni-Mn, and hcp Gd. The simulation approach can complement inelastic neutron scattering experiments to estimate partial contributions of elements to the phonon density of states².

7.2 Sidebands and Nonlinear Optics

Recent advances in laser optics methods, such as the two-dimensional Terahertz-Terahertz (2D-TTR) Raman technique [8, 9], open a field of time-resolved in crystals with nonlinear optical susceptibility function. In the 2D-TTR technique, two phonons are excited by two terahertz pulses, and Raman later probes the coupling of the oscillations. The controlled time delays between terahertz pulses and probing

²Phonon density of states obtained in the INS experiments for alloys are neutron weighted. It means that partial contribution of elements to the density of states is altered by the σ/m factor, where σ and m are the neutron scattering cross-section and mass of an element.

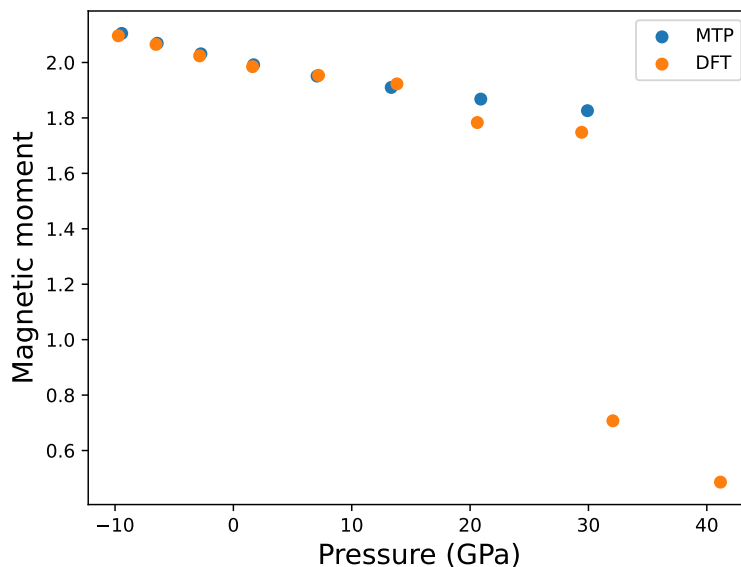


Figure 7.1: Magnetization comparison between DFT data (orange) and collinear spin MLIP (blue) for Fe₆₈Pd₃₂ in the pressure interval from -10 to 40 GPa.

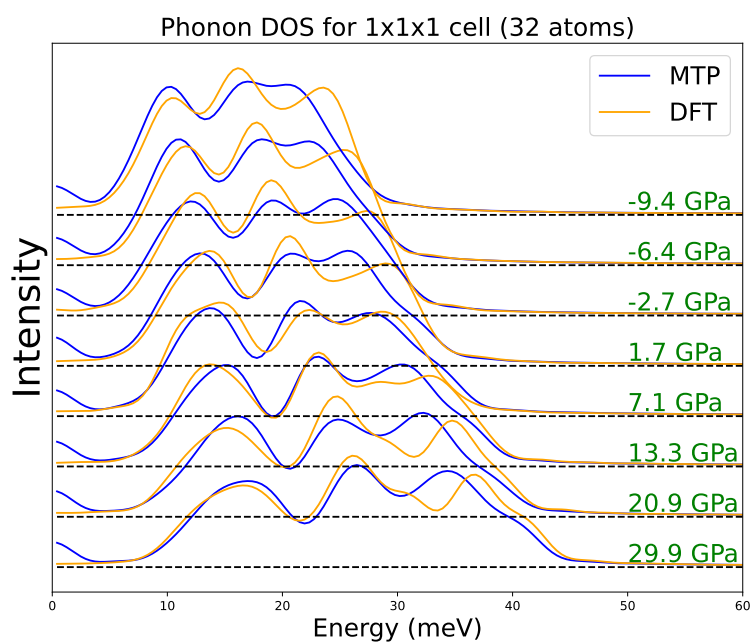


Figure 7.2: Phonon density of states between DFT data (orange) and collinear spin MLIP (blue) for Fe₆₈Pd₃₂ using a 32-atom supercell in the pressure interval from -10 to 40 GPa (top to bottom).

Raman can be Fourier transformed into a 2D map of the coupling frequencies. Also, by tuning the delay between the probing impulse and the THz pump, one can examine the lifetime of the quasiparticle arising from the coupling of two phonon modes. Method from can be used The exact mechanism behind the oscillations coupling can be found using Feynman diagram analyses similar to [10]. The design of the

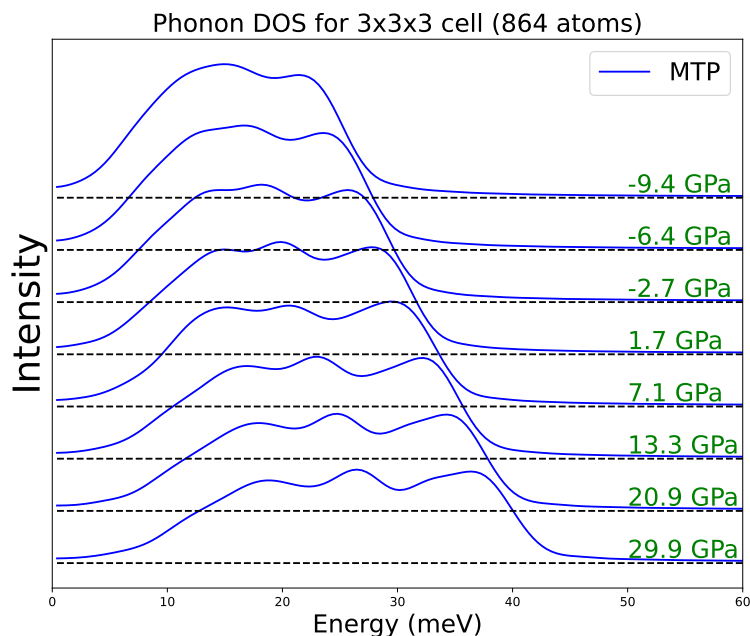


Figure 7.3: Phonon density of states using collinear spin MLIP (blue) for Fe₆₈Pd₃₂ with 864 atom supercell in the pressure interval from -10 to 40 GPa (top to bottom).

experimental setup is shown in Fig. 7.4.

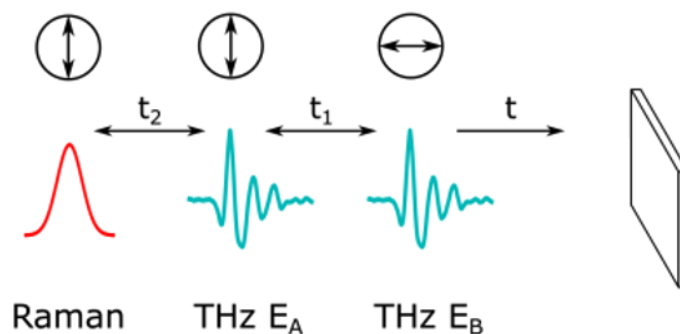


Figure 7.4: Schematic of the 2D-TTR experiment, pulse sequence, and time definitions. The polarization of each pulse is indicated in the circles.

The described technique complements the scattering experiment, providing time information on the intermodulation phenomena and allowing one to identify the phonon modes taking part in intermodulation experimentally. Additionally, since the theoretical technique works with optical susceptibility function, it establishes a stronger connection between the field of nonlinear optics and how it translates to the anharmonic phonon phenomena. A good candidate for the study would be ZnS. The TDEP calculation of vibrational spectra of ZnS along high symmetry directions

(left) and density of states (right) at 300 K are shown in Fig. 7.5. ZnS forms sidebands below and above optical modes and is a well-known optical material. Other candidates suitable for the study are GeTe and ZnTe.

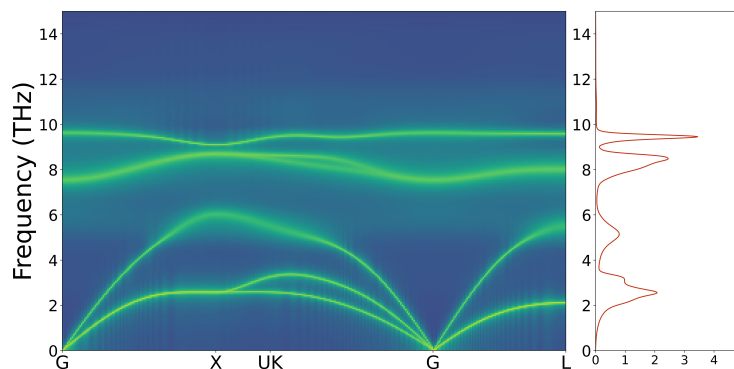


Figure 7.5: Vibrational spectra of ZnS along high symmetry directions (left) and density of states (right) at 300 K computed with TDEP method.

7.3 Diffuse Inelastic Intensity

DII originates in highly anharmonic solids and gives an almost flat contribution to the phonon spectra. However, the time for an anharmonic atom encounter cannot be zero, so the time correlation is not a delta function. The $I(\omega)$ cannot extend to infinite energy. It must roll off at large ω , and future experiments aim to find the shape of $I(\omega)$ at large ω . The found spectral shape of the DII can be back-transformed to give a correlation time, which provides access to the information on the duration of brief anharmonic interactions between atoms. The intensity of the DII allows to estimate the magnitude of the average phase advance ϕ per cycle. Figure 7.6 shows simulations of the DII of cuprite. The DII changes gradually with energy and is incoherent. These simulations tend to underestimate the DII compared to the experiment at energies less than 100 meV, so more intensity is expected in the experiment. In addition to Cu₂O, good candidates for DII are ZnO and ZnTe, which have tetrahedral coordination of the atoms. It is interesting to explore materials with other crystal structures for the presence of DII in the vibrational spectrum. The question is, "Is the cage motion necessary for generating DII?" The proposed level of exploration of the anharmonic part of the phonon potential energy and such detailed information has not been available from experimental measurements to date.

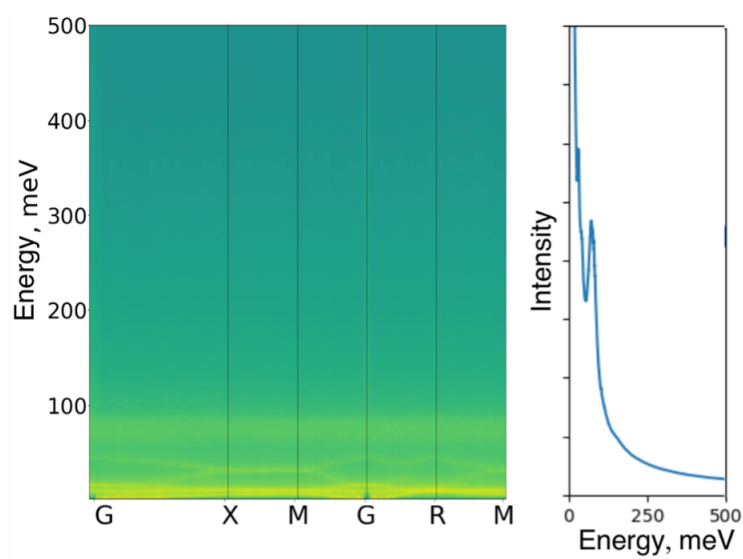


Figure 7.6: Vibrational spectra from autocorrelation function analyses of cuprite at 700 K. Simulations are performed using MLIP with Cu-O bond splined to ZBL potential at low separations. Dispersions are seen at energies below 100 meV. The right panel is phonon DOS.

References

- [1] N. Benshalom, G. Reuveni, R. Korobko, O. Yaffe, and O. Hellman. Dielectric response of rock-salt crystals at finite temperatures from first principles. *Phys. Rev. Mater.*, 6(3):033607, 2022.
- [2] S. Falletta, A. Cepellotti, A. Johansson, C. W. Tan, M. L. Descoteaux, A. Musaelian, C. J. Owen, and B. Kozinsky. Unified differentiable learning of electric response. *Nat. Comm.*, 16(1):4031, 2025.
- [3] S. H. Lohaus, M. Heine, P. Guzman, C. M. Bernal-Choban, C. N. Saunders, G. Shen, O. Hellman, D. Broido, and B. Fultz. A thermodynamic explanation of the invar effect. *Nat. Phys.*, 19(11):1642–1648, 2023.
- [4] I. Novikov, B. Grabowski, F. Körmann, and A. Shapeev. Magnetic moment tensor potentials for collinear spin-polarized materials reproduce different magnetic states of bcc fe. *npj Comput. Mater.*, 8(1):13, 2022.
- [5] M. Matsui, T. Shimizu, H. Yamada, and K. Adachi. Magnetic properties and thermal expansion of fe-pd invar alloys. *J. Magnet. Magnet. Mater.*, 15: 1201–1202, 1980.
- [6] M. Matsushita, T. Nishimura, S. Endo, M. Ishizuka, K. Kindo, and F. Ono. Anomalous magnetic moments in Fe–Pt and Fe–Pd invar alloys under high-pressure. *J. Phys.: Cond. Matt.*, 14(44):10753, 2002.
- [7] H. Yu, Y. Zhong, L. Hong, C. Xu, W. Ren, X. Gong, and H. Xiang. Spin-dependent graph neural network potential for magnetic materials. *Phys. Rev. B*, 109(14):144426, 2024.
- [8] C. L. Johnson, B. E. Knighton, and J. A. Johnson. Distinguishing nonlinear terahertz excitation pathways with two-dimensional spectroscopy. *Phys. Rev. Lett.*, 122:073901, Feb 2019. doi: 10.1103/PhysRevLett.122.073901. URL <https://link.aps.org/doi/10.1103/PhysRevLett.122.073901>.
- [9] H-W. Lin, G. Mead, and G. A. Blake. Mapping linbo₃ phonon-polariton nonlinearities with 2d thz-thz-raman spectroscopy. *Phys. Rev. Lett.*, 129: 207401, Nov 2022. doi: 10.1103/PhysRevLett.129.207401. URL <https://link.aps.org/doi/10.1103/PhysRevLett.129.207401>.
- [10] D. Sidler and P. Hamm. A feynman diagram description of the 2d-raman-thz response of amorphous ice. *J. Chem. Phys.*, 153(4), 2020.